Faculty of Aerospace Engineering

Aerodynamic Stall Modeling for the Cessna Citation II

L.J. van Horssen

August 3, 2016

Delft University of Technology

Challenge the future

Aerodynamic Stall Modeling for the Cessna Citation II

MASTER OF SCIENCE THESIS

For obtaining the degree of Master of Science in Aerospace Engineering
at Delft University of Technology

L.J. van Horssen

August 3, 2016

Faculty of Aerospace Engineering · Delft University of Technology

Delft University of Technology

DELFT UNIVERSITY OF TECHNOLOGY
DEPARTMENT OF
CONTROL AND SIMULATION

The undersigned hereby certify that they have read and recommend to the Faculty of Aerospace Engineering for acceptance a thesis entitled **"Aerodynamic Stall Modeling for the Cessna Citation II"** by **L.J. van Horssen** in partial fulfillment of the requirements for the degree of **Master of Science**.

Dated: August 3, 2016

Readers:

Dr.ir. D.M. Pool

Dr.ir. C.C. de Visser

Prof.dr.ir. M. Mulder

Dr.ir. M.M. van Paassen

Dr.ir. M. Voskuijl

Summary

The largest cause of fatalities in general aviation and an important contributor to accidents in airliners is loss of control in flight (NTSB, 2013). A major contributor to this loss of control are aerodynamic stalls. An aerodynamic stall is a highly dynamic and non-stationary condition where the flow over the wings of the aircraft detaches in unpredictable ways. This can lead to dangerous upset conditions if left uncorrected.

To solve this, the Federal Aviation Administration (FAA) stated that all pilots flying for air-carriers in the United States are obliged to receive training in stall recovery in 2019 (FAA, 2013). Current stall training is often done in smaller (single engine) aircraft, however, the dynamics of such an aircraft differ from large airliners. Due to the risk and cost involved in stall training with these larger aircraft, it is most likely that pilots will receive upset recovery training in Flight Simulation Training Devices (FTSD).

Current development of stall models is mostly based on flight test, wind tunnel and Computational Fluid Dynamics (CFD) data. Flight tests are both expensive and definitely not without danger. Furthermore by using only flight test data it is nearly impossible to model fully developed stalls, such as a (flat) spin. Therefore state-of-the-art flight models are often combined with wind tunnel and/ or CFD analysis to predict the aerodynamics in fully developed stalls.

The major disadvantage of current stall model developments is the huge cost that is involved. Although large aircraft manufactures have the means to use these expensive methods to create stall models, this situation does not apply for smaller General Aviation (GA) aircraft manufacturers. Furthermore it is difficult to obtain fully developed stall data for all commercial aircraft (Schroeder, Bürki-Cohen, Shikany, Gingras, & Desrochers, 2014).

For this reason, the division on Control & Simulation (C&S) at Delft University of Technology (DUT) has set up a 'task force' to develop a new methodology for creating stall models at much lower cost. The first step in this project will consist of the development of a stall model for the Cessna Citation II laboratory aircraft, based on existing flight test data collected over more than a decade of flight tests. This newly identified stall model will be combined with a new high-fidelity dynamics model of the aircraft. This will result in a fully integrated model that can be used to simulate stall onset and initial stall development in SIMONA Research Simulator (SRS) at DUT.

This report is structured as follows. In part I the final paper is given, containing all the results that were found during this research. This includes the aerodynamic parameters for the stall region and a stall buffet model. In part II the preliminary thesis is given, which shows typical stall characteristics. On top of that an explanation of state estimation is given, together with a comparison between different kind of Kalman filters and smoothers, on simulated data. Furthermore a section is written about several optimization algorithms. Lastly in the appendices a few important notes are regarding working with the flight data.

Acronyms

AHRS	Attitude Heading Reference System
AoA	Angle of Attack
AoSS	Angle of Side Slip
C&S	Control & Simulation
CFD	Computational Fluid Dynamics
DADC	Digital Air Data Computer
DASMAT	Delft University Aircraft Simulation Model and Analysis tool
DOP	Dilution of Precision
DUT	Delft University of Technology
ECEF	Earth Centered Earth Fixed
EKF	Extended Kalman Filter
FAA	Federal Aviation Administration
FPR	Flight Path Reconstruction
FTIS	Flight Test Instrumentation System
FTSD	Flight Simulation Training Devices
GA	General Aviation
GPS	Global Positioning System
ICATEE	International Committee for Aviation Training in Extended Envelopes
IEKF	Iterated Extended Kalman Filter
IERTSS	Iterated Extended Rauch Tung Striebel Smoother
IMU	Inertial Measurement Unit
ISA	International Standard Atmosphere
NACA	National Advisory Committee for Aeronautics
NASA	National Aeronautics and Space Administration
NLR	Nederlands Lucht- en Ruimtevaartcentrum
RTS	Rauch Tung Striebel
SME	Subject Matter Expert

SOC	Statement of Compliance
SRS	SIMONA Research Simulator
UKF	Unscented Kalman Filter
UKS	Unscented Kalman Smoother
URTSS	Unscented Rauch Tung Striebel Smoother

List of Symbols

Greek Symbols

α	Angle of attack
α	Scaling parameter for the UKF
$\dot{\alpha}$	Angle of attack rate
α^*	Flow separation delay term of the stall dynamics
β	Angle of side slip
β	Scaling parameter for the UKF
$\boldsymbol{\mathcal{X}}$	Sigma point
δ_e	Elevator deflection (+ upward)
Γ	Discretization of the input matrix
Γ	Wing dihedral angle
Λ	Aspect ratio
λ	Bias term
λ	Scaling parameter for the UKF
μ	Dynamic viscosity of a fluid
Φ	Discretization of the state transition matrix
ϕ	Roll angle
ψ	Yaw angle
ρ	Density
σ	Standard deviation
τ_1	Transient effect of the stall dynamics

τ_2	Hysteresis effect of the stall dynamics
θ	Pitch angle

Roman Symbols

a_1	Stall abruptness term of the stall dynamics
A_x	Acceleration in longitudinal direction (+ forward)
A_y	Acceleration in lateral direction (+ right)
A_z	Acceleration in normal direction (+ down)
C_{α_0}	Unknown wind component
$C_{\alpha_{up}}$	Fuselage upwash coefficient
C_{β_0}	Unknown wind component
$\bar{c}$	Mean aerodynamic chord
$C_{\beta_{si}}$	Fuselage sidewash coefficient
C_D	Drag coefficient
C_L	Lift coefficient
C_m	Moment coefficient
D	Smoother gain
Δy	Effective lever arm
e	Oswalt factor
f	System dynamics
F_u	Input Jacobian
F_x	State transition Jacobian
g	Gravitational acceleration (= 9.80665 m/s^2)
h	Altitude
h	Observation dynamics
H_x	Measurement Jacobian
K	Kalman gain
L	Characteristic linear dimension
L	Dimension of the state vector
M	Mach number
m	Mass
n	Load Factor
p	Roll rate
Q	Process noise covariance matrix

q	Pitch rate
R	Observation noise covariance matrix
r	Yaw rate
Re	Reynolds number
S	Wing Surface
u	Longitudinal body velocity
u	Input
v	Lateral body velocity
v	Velocity of the object relative to the fluid
V_{stall}	Stall Speed
V_{TAS}	True Airspeed
W	Weighing vector
w	Normal body velocity
W_{x_E}	Wind velocity in x-direction in ECEF frame
W_{y_E}	Wind velocity in y-direction in ECEF frame
W_{z_E}	Wind velocity in z-direction in ECEF frame
X	Flow separation point
x	State
x_E	x-position in ECEF frame
x_{v_α}	Distance from angle of attack measurement to center of gravity
x_{v_β}	Distance from angle of side slip measurement to center of gravity
y_E	y-position in ECEF frame
z_E	z-position in ECEF frame
z_{v_β}	Distance from angle of side slip measurement to center of gravity

Subscripts

$_0$	Initial or steady
$_{max}$	maximum
$_{k,k+1}$	Predicted (a priori) estimate
$_{k+1,k+1}$	Updated (a posteriori) estimate
$_m$	Measured

Contents

III Appendices

Part I

Paper

Aerodynamic Stall Modeling for the Cessna Citation II based on Flight Test Data

L.J. van Horssen* and D.M. Pool† and C.C. de Visser ‡ and M. Mulder§

Delft University of Technology, Delft, Zuid-Holland, 2629 HS, the Netherlands

In 2019 all air-carrier pilots are obliged to go through flight simulator-based stall recovery training. Therefore simulators will have to be equipped with accurate flight models at high angles of attack. This paper shows which stall characteristics can be modeled using flight data from symmetrical induced, quasi-steady stalls. Furthermore a well-known stall model structure is used, based on Kirchoff's flow separation theory. It is shown that the hysteresis effect can be estimated using quasi-steady stall maneuvers. Aerodynamic terms related to the pitch rate, however, are not identifiable using such maneuvers. Transient effects on the other hand, which are normally only expected with highly dynamic maneuvers, could be estimated using the accelerations caused by the stall buffet. Lastly a stall buffet model is proposed, based on power spectral density analysis of the acceleration measurements.

Nomenclature

a_1	Parameter that influences the stall abruptness
a_x, a_y, a_z	Linear accelerations in the center of gravity, m/s^2
$a_{x_{ac}}, a_{y_{ac}}, a_{z_{ac}}$	Measured acceleration by the AHRS, m
b	Wing span, m
$\bar{c}$	Mean aerodynamic chord, m
C_{α_0}	Unknown wind component in angle of attack, rad
$C_{\alpha_{up}}$	Fuselage upwash component effect on angle of attack
g	Acceleration due to gravity, m/s^2
h	Altitude, m
$\dot{h}$	Climb rate, m/s
I_{xx}, I_{yy}, I_{zz}	Moments of inertia around body axes, kgm^2
I_{xz}	Cross moment of inertia between x- and z-axes, kgm^2
m	Aircraft mass, kg
p, q, r	Body-axes rotational rates, rad/s
$\dot{p}, \dot{q}, \dot{r}$	Body-axes rotational accelerations, rad/s^2
S	Wing surface, m^2
T	Engine thrust, N
u, v, w	Longitudinal-, lateral- and vertical body velocities, m/s
V_{TAS}	True airspeed, m/s
w_r	Random walk
$W_{x_E}, W_{y_E}, W_{z_E}$	Wind velocities in the ECEF frame, m/s
X	Unsteady flow separation point
X_0	Steady flow separation point
x, y, z	Position in the Earth centered Earth fixed frame, m

---

[*] MSc student, Faculty of Aerospace Engineering, Control and Simulation Division

[†] Assistant Professor, Faculty of Aerospace Engineering, Control and Simulation Division, 2629 HS Delft, The Netherlands.

[‡] Assistant Professor, Faculty of Aerospace Engineering, Control and Simulation Division, 2629 HS Delft, The Netherlands.

[§] Professor, Faculty of Aerospace Engineering, Control and Simulation Division, 2629 HS Delft, The Netherlands.

$\dot{x}, \dot{y}$	Velocity in the Earth centered Earth fixed frame, m
x_{ac}, y_{ac}, z_{ac}	Location where the acceleration is measured, m
x_{cg}, y_{cg}, z_{cg}	Center of gravity location, m
x_{v_α}	Distance between the center of gravity and the alpha-vane, m
Δy	Effective lever arm, m

Symbols

α	Angle of attack, rad
α^*	Angle of attack for $X_0 = 0.5$, rad
α_v	Angle of attack measured by the alpha-vane, rad
α^*	Expected angle of attack in the area of the alpha-vane, rad
β	Angle of side slip, rad
$\delta_e, \delta_a, \delta_r$	Elevator, aileron and rudder deflections, rad
δ_f	Flap deflection, rad
Γ	Dihedral angle, rad
λ	Bias term in the linear accelerations and rotational rates
ϕ, θ, ψ	Euler angles (roll, pitch, yaw), rad
ρ	Density, kgm^{-3}
τ_1	Time constant for the hysteresis effect of the stall dynamics, s
τ_2	Time constant for the transient effect of the stall dynamics, s
τ_v	Time delay constant of the alpha-vane, s

I. Introduction

Aerodynamic stall is a highly dynamic, non-stationary condition where the flow over the wings of the aircraft separates in unpredictable ways, leading to dangerous upset conditions if left uncorrected. Stalls currently are the primary cause of fatal accidents in general aviation, and are an important contributor to fatal accidents in civil aviation.[1] As a result of new aviation legislation, in 2019 all air-carrier pilots are obliged to go through flight simulator-based stall recovery training.[2] To date, simulators were not required to have an accurate representation of flight in the stall regime.[3] This implies that the aircraft dynamics models driving flight simulators must be updated to include accurate stall and post-stall dynamics.

Accurate simulations of high angle of attack maneuvers have been developed for fighter jets.[4–6] These models were based on wind tunnel data, which included both static and dynamic tests using a rotary balance.[7] Due to the new aviation legislation current research not only focuses on fighter jets, but also on general aviation and large transport jets. A European effort into stall modeling has been performed by the SUPRA project. During this project a stall model for a generic transport aircraft, low-wing configuration and engines positioned under the wings, has been created. The SUPRA model is mainly based on wind tunnel and computational fluid dynamics (CFD) data.[8] Another contribution was made by NASA, who has researched the development of upset conditions for large transport aircraft. This model was created using wind tunnel data and validated with flight data. One issue regarding wind tunnel modeling, however, are aerodynamic scale effects such as the Reynolds number.[3]

Other efforts have been made in stall modeling, using semi-empirical and analytical data. This included computational methods such as the Vortex Lattice Method (VLM). These methods, however, are primarily used for aircraft design.[9] A similar research has been done in modeling the stall characteristics due to different parts of the aircraft.[10] Current practice however is that stall models are created using wind tunnel, CFD and possibly flight data. It has been shown that a wind tunnel based stall model is able to represent stalling dynamics,[11, 12] however, aerodynamic scale effects could lead to errors in the flight model.

Currently, when basing a stall model on flight data, specifically designed input maneuvers have been applied for parameter identification.[13, 14] A comparison between a quasi-steady stall and a dynamic stall has been made, showing that the quasi-steady stall model was less robust.[15] It is currently not clear, however, which stall characteristics can be modeled using such quasi-steady stalls. As presented by Gingras et. al.,[11] the ICATEE proposed several stall characteristics to be modeled, for representative stall model simulation, including:

- Stall buffet,
- Stall hysteresis,
- Changes in pitch stability,
- Degradation in control response (pitch, roll, yaw),
- Uncommanded roll response or roll-off, requiring significant control deflection to counter,
- Apparent randomness or non-repeatability,
- Degradation in static/dynamic lateral-directional stability

In this paper it is shown which of these characteristics can be modeled using flight data of quasi-steady, symmetrical induced, stall maneuvers, without a side slip measurement. The stall model will be split into a low-frequency and a high-frequency model. The low-frequency model contains the aerodynamic stability and control derivatives, which calculates the baseline for the forces and moments. The high-frequency model adds high-frequency accelerations on top of the accelerations as predicted by the low-frequency model. Essentially, the high-frequency model will be used for re-creating the stall buffet. Both models will be created, based on flight data of a Cessna Citation II, for which data was collected of a large number of quasi-steady stalls.

The layout of this paper is as follows. First a description of the aircraft will be given, containing information on its mass, inertia and instrumentation system. Together with this description an overview of all the flight test points will be given in Section II. Secondly the flight path reconstruction (FPR) will be explained in Section III. This includes pre-processing of the data, the kinematic equations and the post-processing. In Section IV the aerodynamic and buffet model structures are given. Next to that the method of parameter identification is explained and a discussion is given on how to blend the stall model with the baseline model. The outcome of the work will be given in Section V. Finally in Section VI and Section VII, a discussion and the conclusions on the results are given, respectively.

II. Research Vehicle and Flight Data

The aircraft being modeled is a Cessna Citation II, model 550. This aircraft is property of Delft University of Technology (DUT) and the Netherlands Aerospace Center (NLR). The aircraft is a twinjet business jet, with two Pratt & Whitney JT15D-4 turbofan engines, with a maximum thrust of 11.1 kN each. Its maximum operating speed is 198.6 m/s, with a maximum operating altitude of 13 km.[16]

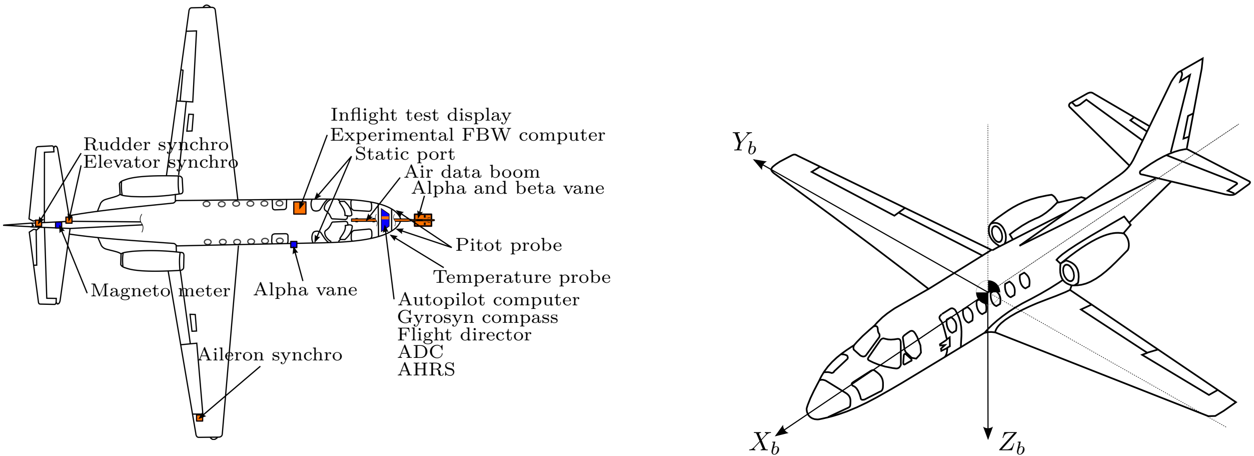

(a) Overview of the aircraft instrumentation system

(b) Aircraft body axes $\mathbb{F}_b$ definition

Figure 1. Aircraft instrumentation system and reference frame

A. Dimensions and mass properties

The Cessna Citation II is 14.4 meters long and has an outer fuselage diameter of 1.63 meters. The sweep-back of the main wings at 25% chord is 1.4 degrees, and it has a 4.0 deg dihedral. The aircraft basic empty weight (BEW) and inertia properties are given in Table 1. Furthermore the distance between the angle of attack vane and the aircraft nose is approximately 4 meters. The attitude and heading reference system (AHRS) is located beneath the floor of the nose baggage compartment, which is the compartment in front of the forward pressure bulkhead. The distance between the AHRS system and the nose is approximately 1.9 meters.

B. Instrumentation

The flight test instrumentation system (FTIS) on the Cessna Citation II contains among others:

- an AHRS, which contains information on the Euler angles (ϕ, θ, ψ), the body-axes rotational rates (p, q, r) and the linear accelerations (a_x, a_y, a_z). The linear accelerations: a_y and a_z were compensated for the gravity component, meaning that in stationary flight these measurements were zero. The linear acceleration in x-direction however did not contain this compensation and thus it measured the specific force. These measurement had a sampling frequency of 50 Hz.

- a digital air data computer (DADC) which measures among others, the true airspeed (V_{TAS}). All measurements by the DADC had a sampling frequency of 16.67 Hz.

- a differential global positioning system (DGPS), which contained information regarding the position and change in position $(\dot{x}, \dot{y}, \dot{h})$. The position was originally measured in longitude, latitude and altitude, but for this research was transformed into flat Earth coordinates (x, y, z), using a standard transformation matrix. The DGPS measurements had a sampling frequency of 1 Hz.

- an air data boom and an angle of attack vane. The air data boom was, however, not available during the data collection for this research project. Therefore only the angle of attack vane was used to measure the angle of attack (α), this vane had a sampling frequency of 1000 Hz.

- a set of synchro's on the elevator, aileron, rudder and flaps $(\delta_e, \delta_a, \delta_r, \delta_f)$ to measure the control surface deflections. These were measured with a sampling frequency of 100 Hz.

Table 1. Dimensions and mass properties of the aircraft

Dimensions	
b	15.9 m
$\bar{c}$	2.06 m
S	30.0 m^2

Mass properties	
m	4,157 kg
I_{xx}	12,392 kgm^2
I_{yy}	31,501 kgm^2
I_{zz}	41,908 kgm^2
I_{xz}	2252.2 kgm^2

All values correspond to the basic empty weight.

A summary of the accuracy and update rates of the different sensors is given in Table 2.

C. Flight Data

In the third year bachelor course *Aerospace Flight Dynamics & Simulation* at Delft University of Technology, students take part in a flight test. During these flight tests, students have to obtain data which has to be processed later on. Students also experience the eigenmodes of the Cessna Citation II, weightlessness and a stall. These stalls are symmetrical induced and quasi-steady, by slowly approaching the stall speed with approximately 1 kts/s deceleration. In total 69 quasi-steady stalls were used for the development of the stall model, meaning that the pitch rate is approximately zero during the approach to stall. On top of that four stalls were flown using a pull-up maneuver, in which the aircraft pitched up with a load factor of approximately 1.3 g. In each of these dynamically induced stalls were flown in a different configuration: flaps and gear up, flaps at 15° and landing gear up, flaps at 15° and landing gear down and flaps at 40° and landing gear down. In each of these non-cruise configuration two stalls were performed: One quasi-steady stall and

Table 2. **Standard update rates and noise standard deviations of the sensors**

Measurement	Update frequency [Hz]	std	unit	Source
x	1	$2.08 \cdot 10^{-1}$	m	GPS
y	1	$2.75 \cdot 10^{-1}$	m	GPS
h	1	$2.29 \cdot 10^{-1}$	m	GPS
$\dot{x}$	1	n/a	m/s	GPS
$\dot{y}$	1	n/a	m/s	GPS
$\dot{h}$	1	$1.08 \cdot 10^{-1}$	m/s	GPS
ϕ	50	$1.62 \cdot 10^{-3}$	rad	AHRS
θ	50	$3.40 \cdot 10^{-4}$	rad	AHRS
ψ	50	$1.13 \cdot 10^{-3}$	rad	AHRS
V_{TAS}	16.67	$8.97 \cdot 10^{-2}$	m/s	DADC
α	1000	$2.10 \cdot 10^{-4}$	rad	alpha-vane
p	50	$9.40 \cdot 10^{-4}$	rad/s	AHRS
q	50	$3.10 \cdot 10^{-4}$	rad/s	AHRS
r	50	$5.90 \cdot 10^{-4}$	rad/s	AHRS
a_x	50	$1.59 \cdot 10^{-2}$	m/s^2	AHRS
a_y	50	$4.74 \cdot 10^{-2}$	m/s^2	AHRS
a_z	50	$8.48 \cdot 10^{-2}$	m/s^2	AHRS
δ_e	100	$1.39 \cdot 10^{-3}$	rad	synchro
δ_a	100	$5.50 \cdot 10^{-4}$	rad	synchro
δ_r	100	$3.90 \cdot 10^{-4}$	rad	synchro

a stall with a pull-up maneuver. An overview of the test maneuvers within the flight envelope is shown in Figure 2. During the stall model development approximately 75% was used for model identification, the other 25% was used for validation. The validation sets are numbered from 1 to 17 in Figure 2.

III. Flight Path Reconstruction

The first step in aerodynamic modeling, based on flight data is to perform flight path reconstruction (FPR). This is done to correct certain variables, such as the linear accelerations and the angle of attack for instrumentation errors. FPR is essentially state estimation of the aircraft, for which a Kalman filter can be used. The chosen filter for this research is the Unscented Kalman filter (UKF).[17, 18]

A. Pre-processing

As described in Section II, the acquisition rates differ between sensors. One method of coping with this is by using a multi-rate Kalman filter[19] (MRKF). For this research, however, FPR can be done offline and thus instead of using a MRKF, the data were re-sampled to a sampling time of 10 ms (100 Hz).

After re-sampling it was necessary to correct the linear acceleration for an offset w.r.t. the center of gravity. The linear accelerations are measured by the AHRS system, which is approximately 1.9 meters from the nose. The center of gravity, however, lies between 18.0% and 30.0% of the mean aerodynamic chord (MAC).[16] To compensate for this offset the following set of equations can be used:[20]

$$\begin{aligned}
a_{x_{cg}} &= a_{x_{ac}} + (x_{cg} - x_{ac})\left(q^2 + r^2\right) - (y_{cg} - y_{ac})(pq - \dot{r}) - (z_{cg} - z_{ac})(pr - \dot{q}) \\
a_{y_{cg}} &= a_{y_{ac}} + (y_{cg} - y_{ac})\left(r^2 + p^2\right) - (z_{cg} - z_{ac})(qr - \dot{p}) - (x_{cg} - x_{ac})(qp - \dot{r}) \\
a_{z_{cg}} &= a_{z_{ac}} + (z_{cg} - z_{ac})\left(p^2 + q^2\right) - (x_{cg} - x_{ac})(rp - \dot{q}) - (y_{cg} - y_{ac})(rq - \dot{p})
\end{aligned} \qquad (1)$$

There are two issues in applying Eq.(1) before the FPR. First of all, any biases in the rotational rates have not been filtered out yet. These biases can be estimated using FPR, by adding an extra term (λ) to the

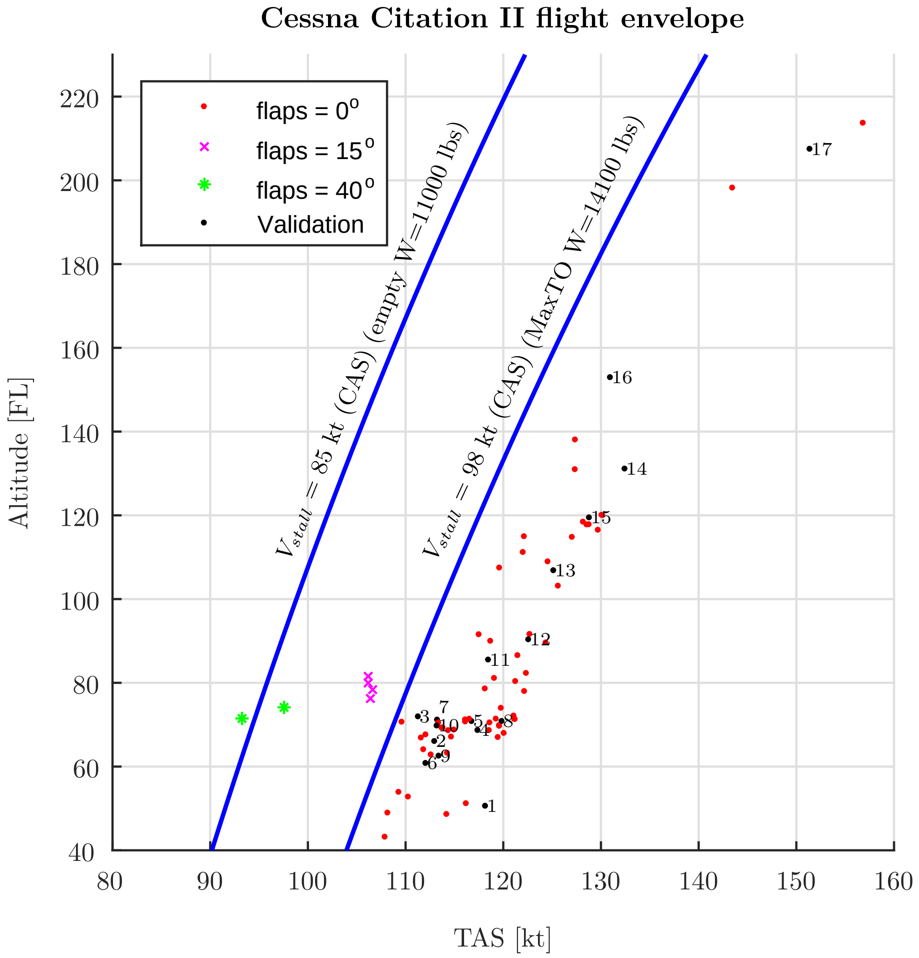

Figure 2. An overview of where the data points were captured within the flight envelope

measured acceleration and rotational rates. Assuming that during the maneuver the bias does not change, the time derivative of the bias term ($\dot{\lambda}$) is equal to zero. As shown in Figure 3, however, these biases in rotational rates are rather small. Therefore the error introduced by neglecting the bias in the rotational rates will be rather small. In fact the error caused by not correcting the acceleration measurement for the offset w.r.t. the center of gravity, is larger than assuming that the biases are zero.

Another problem is to obtain the rotational accelerations ($\dot{p}$,$\dot{q}$,$\dot{r}$), since these are not measured directly. To obtain these rotational accelerations the rotational rates have to be numerically differentiated. Numerically differentiating the rotational rates, however, can lead to noise amplification. To prevent this the rotational rates are first filtered, using a zero-phase low-pass filter.[21] Then after filtering the rates could be differentiated (still neglecting the bias) to obtain the rotational accelerations.

Furthermore, the center of gravity position needs to be known, this is not a trivial task since the center of gravity changes throughout the flight. To obtain the distance of the center of gravity w.r.t. the nose, a mass model has been used of the Cessna Citation II. The BEW was obtained by placing the wheels of the aircraft on three separate weight scales. Furthermore the weight of each passenger was measured, as well as the fuel state at the start of the flight. This allowed for a rather accurate estimation of the center of gravity of the aircraft.

Not only do the linear accelerations have to be corrected for the offset in the center of gravity, they also have to be pre-filtered using a low-pass filter. This is due to the buffet effect, which is not captured by the dynamic equations. An example of the raw vertical linear acceleration vs. the filtered acceleration is given in Figure 4. The cut-off frequency was chosen to be 0.8 Hz. The reason for this value is due to the angle of attack measurement, which is measured by a physically damped vane. The damping of this vane corresponds to a cut-off frequency of 0.8 Hz, as will be shown in Subsection III.B.1.

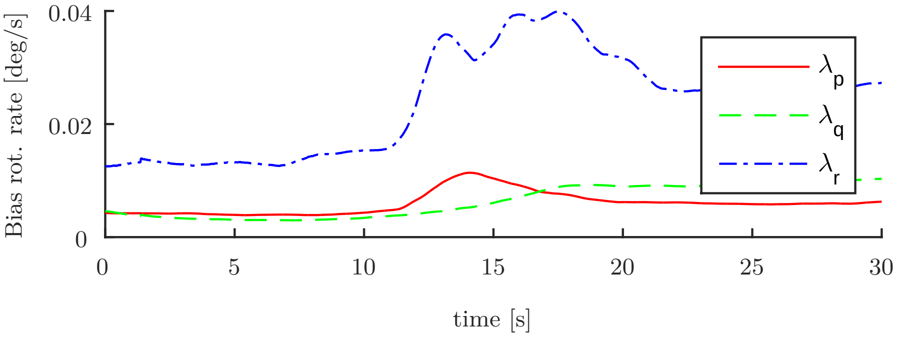

Figure 3. Average bias in the rotational rate measurements

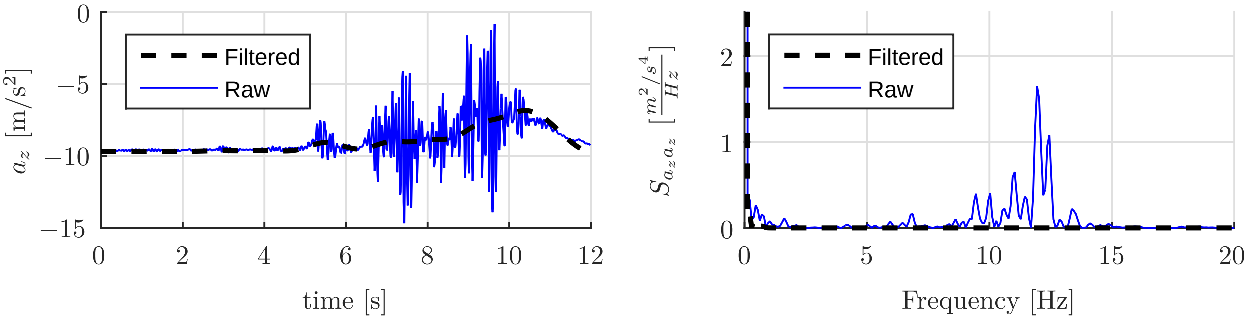

(a) Time history plot (b) Power Spectral Density

Figure 4. An example of the pre-filtered acceleration input vs. the raw acceleration

Due to the unavailability of the air data boom, for the recorded stalls, a measurement of the side slip angle was not available. Without a measurement of the side slip angle the lateral velocity component (v) does not converge well. Therefore it is better to use a pseudo-beta in longitudinal maneuvers.[22] This pseudo-beta is a zero mean white noise signal, for this research the noise intensity was set to 0.01°, which was found by trial and error. With the introduction of a pseudo-beta the estimated values of the side slip angle and the bias term in the lateral acceleration will be meaningless, nonetheless this pseudo-beta improves the performance of the state estimation for longitudinal maneuvers.

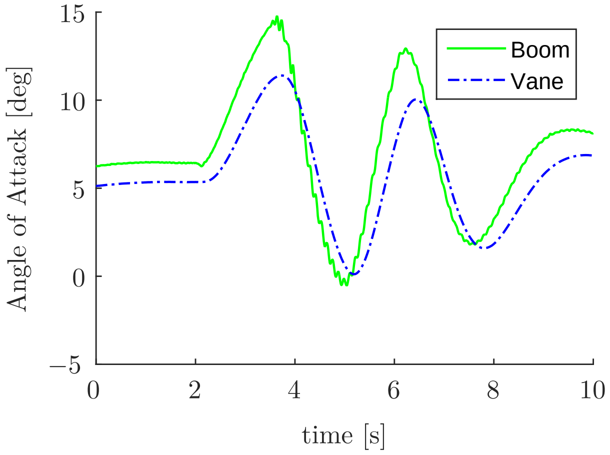

Figure 5. The angle of attack as measured by the boom and by the vane

B. Kinematic equations

1. *Alpha vane dynamics*

The aircraft was not equipped with an air-data boom and thus an alpha vane on the fuselage was used to measured the angle of attack. This angle of attack is normally not used for model identification because of its inherent mechanical lag ($\tau \approx 0.2$ s). A comparison between a measurement of the air data boom and the alpha-vane is shown in Figure 5. This dataset, in which both the air-data boom and the alpha-vane were available, is from older flight tests performed by Delft University of Technology. These flight tests were originally performed for comparing multimodal pilot pitch control behavior[23] and global nonlinear model identification with multivariate splines.[24] From Figure 5 several observations can be made:

1. Body induced velocities are definitely present in the alpha-vane, since the angle of attack measured by

the vane is approximately 1.1 degrees lower than angle of attack measured by the boom. Although it must be noted that the boom in this case is the raw signal, and is not corrected for any body induced velocities.

2. The angle of attack as measured by the vane is well damped, resulting in a smooth signal. The boom measurements contain higher frequency components.

3. The damping of the vane also causes a lag in its measurement. When comparing the vane with the boom, the vane has a lag of approximately 0.2 seconds. This causes the signal to be low-pass filtered with a cut-off frequency of approximately 5 rad/s (≈ 0.8 Hz).

To capture the effect of the body induced velocities, the angle of attack model model is extended by: a correction for the pitch rate of the aircraft, a fuselage upwash component on the angle of attack ($C_{\alpha_{up}}$) and an unknown wind component in the angle of attack (C_{α_0}). The resulting equation is:[20]

$$\alpha_v^* = \left(1 + C_{\alpha_{up}}\right) \arctan \frac{w}{u} - \frac{x_{v_\alpha}\left(q - \lambda_q\right)}{\sqrt{u^2 + v^2 + w^2}} + C_{\alpha_0} \tag{2}$$

Another issue with the angle of attack measured by the vane is the lag of approximately 0.2 seconds. This can be compensated for by modeling the angle of attack vane as a first order filter.[22] This filter is given by:

$$\frac{\alpha_v\left(s\right)}{\alpha_v^*\left(s\right)} = \frac{1}{\tau_v s + 1} \quad \Rightarrow \quad s\alpha_v\left(s\right) = \frac{1}{\tau_v}\left(\alpha_v^*\left(s\right) - \alpha_v\left(s\right)\right) \tag{3}$$

Here α_v is the measured angle of attack by the vane and α_v^* is the true angle of attack in the area of the α-vane, as given in Eq.(2). Combining Eqs. (2) and (3) results in:

$$\dot{\alpha}_v = \frac{1}{\tau_v}\left(\alpha_v^* - \alpha_v\right) = \frac{1}{\tau_v}\left[\left(1 + C_{\alpha_{up}}\right)\arctan\frac{w}{u} - \frac{x_{v_\alpha}\left(q - \lambda_q\right)}{\sqrt{u^2 + v^2 + w^2}} + C_{\alpha_0} - \alpha_v\right] \tag{4}$$

Where the value of the time constant (τ_v) is set to 0.2 seconds. In practice this time constant could be a function of the flight condition, during this research, however, the time constant was assumed to be constant.

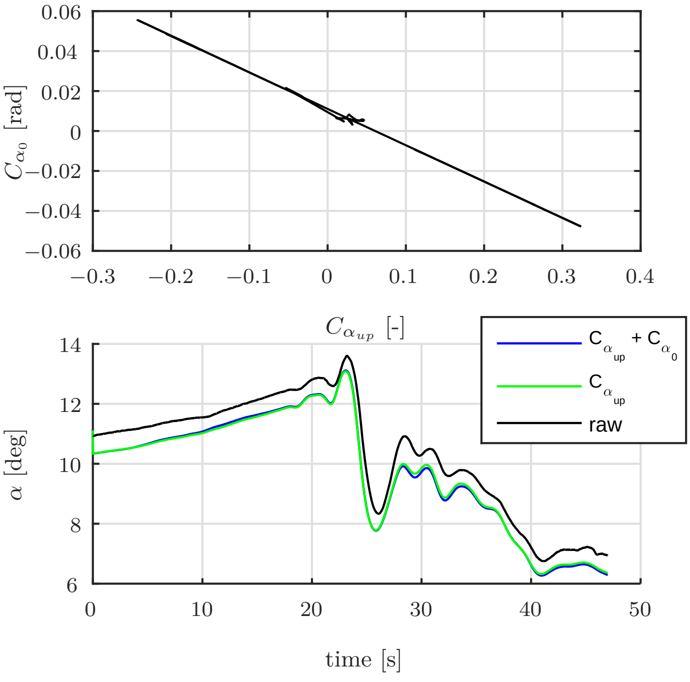

Figure 6. Top: Correlation between $C_{\alpha_{up}}$ and C_{α_0}. Bottom: Difference on the estimated angle of attack

2. Navigation Equations

The full set of navigation equations, i.e., the kinematic equations of the state are given by Eq. (5).

An important factor in state estimation, however, is that the state should be observable. Observability of the system can be calculated theoretically,[25] but this does not necessarily mean that the Kalman filter will converge. Theoretically the system as given by Eq. (5), is fully observable with the observation equations as given in Eq. (6). It was observed that the vertical wind component (W_{z_E}) would not converge. Furthermore the variables $C_{\alpha_{up}}$ and C_{α_0} are considerably correlated, as shown in Figure 6. This correlation can also be seen in Figure 7, where until the stall, both $C_{\alpha_{up}}$ and C_{α_0} could not converge. Therefore the unknown wind component (C_{α_0}) was removed from the state equations. The effect on the reconstructed angle of attack is shown in Figure 6, as can be seen there is no clear difference between using both $C_{\alpha_{up}}$ and C_{α_0} or only using $C_{\alpha_{up}}$.

The other variable, the vertical wind component (W_{z_E}) had to be omitted as well. Most flight tests, however, were done in relatively calm weather, in which the vertical wind components are in the order of 0.1 to 0.2 m/s.[26] Therefore this introduces a small but unpreventable error in the FPR.

Furthermore it is assumed that bias in the linear accelerations and rotational rates is constant throughout the maneuver. The wind components in the horizontal plane and the up wash coefficient, however, might not be constant throughout the stall maneuver. Therefore these time derivatives are modeled as a random walk, to give the Kalman filter more freedom in changing these values.

Lastly the gravity components in the equations for $\dot{v}$ and $\dot{w}$ are omitted, due to the correction of these measurements for the gravity components, as explained in Section III A.

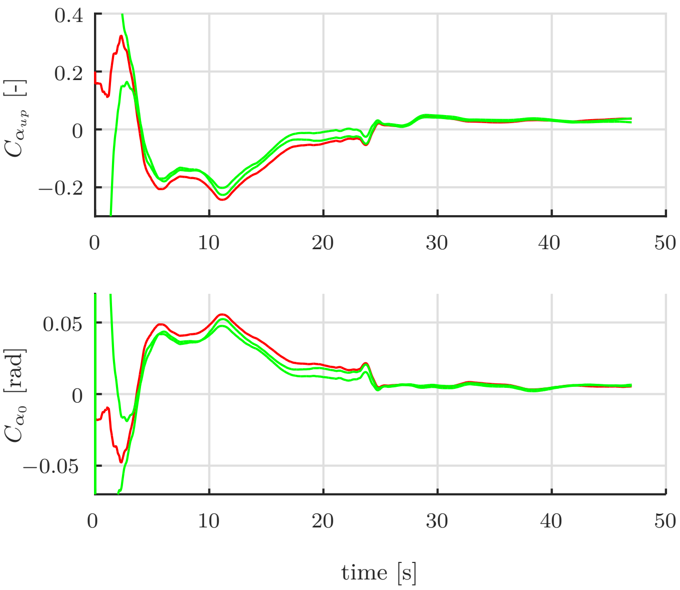

Figure 7. Upwash coefficient $C_{\alpha_{up}}$ and unknown wind component C_{α_0} for three different initial conditions.

$$
\begin{array}{rcl}
\dot{x} & = & [u\cos\theta + (v\sin\phi + w\cos\phi)\sin\theta]\cos\psi - (v\cos\phi - w\sin\phi)\sin\psi + W_{x_E} \\
\dot{y} & = & [u\cos\theta + (v\sin\phi + w\cos\phi)\sin\theta]\sin\psi + (v\cos\phi - w\sin\phi)\cos\psi + W_{y_E} \\
\dot{z} & = & -u\sin\theta + (v\sin\phi + w\cos\phi)\cos\theta + \cancel{W_{z_E}} \\
\dot{u} & = & (a_x - \lambda_x) - g\sin\theta - (q-\lambda_q)\,w + (r-\lambda_r)\,v \\
\dot{v} & = & (a_y - \lambda_y) + \cancel{g\cos\theta\sin\phi} - (r-\lambda_r)\,u + (p-\lambda_p)\,w \\
\dot{w} & = & (a_z - \lambda_z) + \cancel{g\cos\theta\cos\phi} - (p-\lambda_p)\,v + (q-\lambda_q)\,u \\
\dot{p} & = & (p-\lambda_p) + (q-\lambda_q)\sin\phi\tan\theta + (r-\lambda_r)\cos\phi\tan\theta \\
\dot{q} & = & (q-\lambda_q)\cos\phi - (r-\lambda_r)\sin\phi \\
\dot{r} & = & (q-\lambda_q)\,\frac{\sin\phi}{\cos\theta} + (r-\lambda_r)\,\frac{\cos\phi}{\cos\theta} \\
\dot{W}_{x_e} & = & 0.01 w_r \\
\dot{W}_{y_e} & = & 0.01 w_r \\
\cancel{\dot{W}_{z_e}} & = & \cancel{0.01 w_r} \\
\dot{C}_{\alpha_{up}} & = & \frac{0.1\pi}{180} w_r \\
\cancel{\dot{C}_{\alpha_0}} & = & \cancel{\frac{0.1\pi}{180} w_r} \\
\dot{\lambda}_x & = & 0 \\
\dot{\lambda}_y & = & 0 \\
\dot{\lambda}_z & = & 0 \\
\dot{\lambda}_p & = & 0 \\
\dot{\lambda}_q & = & 0 \\
\dot{\lambda}_r & = & 0 \\
\dot{\alpha}_v & = & \frac{1}{\tau_v}\left(\left(1 + C_{\alpha_{up}}\right)\arctan\frac{w}{u} - \frac{x_{v_\alpha}(q-\lambda_q)}{\sqrt{u^2+v^2+w^2}} + \cancel{C_{\alpha_0}} - \alpha_v\right)
\end{array}
\qquad (5)
$$

3. *Observation Equations*

The observation equations are given in Eq. (6). The DGPS was used to obtain the position and velocity in the Earth Centered Earth Fixed (ECEF) frame. The DADC was used for the true airspeed. The AHRS was used for the Euler angles and the alpha-vane was used to obtain the angle of attack. The value of the side slip angle was unavailable and therefore a pseudo-beta is used, as was explained in Section III A.

$$
\begin{aligned}
x_{gps} &= x \\
y_{gps} &= y \\
h_{gps} &= -z \\
\dot{x}_{gps} &= u\sin\theta - (v\sin\phi + w\cos\phi)\cos\theta \\
\dot{y}_{gps} &= [u\cos\theta + (v\sin\phi + w\cos\phi)\sin\theta]\cos\psi - (v\cos\phi - w\sin\phi)\sin\psi + W_{x_E} \\
\dot{h}_{gps} &= [u\cos\theta + (v\sin\phi + w\cos\phi)\sin\theta]\sin\psi + (v\cos\phi - w\sin\phi)\cos\psi + W_{y_E} \\
\phi_{AHRS} &= \phi \\
\theta_{AHRS} &= \theta \\
\psi_{AHRS} &= \psi \\
V_{TAS} &= \sqrt{u^2 + v^2 + w^2} \\
\alpha_{vane} &= \alpha_v \\
\beta_{pseudo} &= \arctan\left(\frac{v}{\sqrt{u^2+w^2}}\right)
\end{aligned}
\tag{6}
$$

C. Post-processing

After the state estimation, it is necessary to add the gravity acceleration components in y- and z-directions, to the measured accelerations by the AHRS. This can be done by a ECEF frame to body frame transformation, where gravity is defined negative downward. The transformation matrix from the ECEF to the body frame is given by:

$$
\mathbb{T}_{bE} = \begin{bmatrix} \cos(\theta)\cos(\psi) & \cos(\theta)\sin(\psi) & -\sin(\theta) \\ \sin(\phi)\sin(\theta)\cos(\psi) - \cos(\phi)\sin(\psi) & \sin(\phi)\sin(\theta)\sin(\psi) + \cos(\phi)\cos(\psi) & \sin(\phi)\cos(\theta) \\ \cos(\phi)\sin(\theta)\cos(\psi) + \sin(\phi)\sin(\psi) & \cos(\phi)\sin(\theta)\sin(\psi) - \sin(\phi)\cos(\psi) & \cos(\phi)\cos(\theta) \end{bmatrix} \tag{7}
$$

Lastly the thrust has to be calculated for the model identification. This thrust is calculated using a look-up table of the Pratt & Whitney JT15D-4 turbofan engine, with as inputs the fan speed ($N1$) and the Mach number.

IV. Aerodynamic Model Identification

The stall model is divided into two sub-models: A low-frequency aerodynamic model and a high-frequency buffet model. The aerodynamic model will calculate all the aerodynamic forces and moments on the aircraft. This model is based on well-known aerodynamic stability and control derivatives, such as $C_{m_{\delta_e}}$.[27] The lift, drag and pitch moment equations, however, are augmented using Kirchoff's theory of flow separation.[15,28] The lateral model will be created by modeling the forces for each wing separately. The buffet model creates a high-frequency signal on top of the baseline accelerations, to reproduce the vibrations due to the flow separation.

A. Aerodynamic Model

The low-frequency aerodynamic model will be based on Kirchhoff's theory of flow separation, which has been applied before to a large transport aircraft[28] and a turboprop aircraft.[15] The main idea of this method is to let the lift coefficient depend on the flow separation point on the wing. This can be modeled using Eq. (8), where X is the flow separation point. When the flow is fully attached the flow separation point (X) has a value of one, whereas a fully detached flow gives a value of zero.

$$
C_L(\alpha, X) = C_{L_\alpha}\left\{\frac{1+\sqrt{X}}{2}\right\}^2 \alpha \tag{8}
$$

The flow separation point is modeled as a differential equation:[28]

$$
\tau_1 \frac{dX}{dt} + X = \frac{1}{2}\left\{1 - \tanh\left(a_1\left(\alpha - \tau_2\dot{\alpha} - \alpha^*\right)\right)\right\} \tag{9}
$$

As can be seen in Eq. (9), the flow separation point is a function of the angle of attack and the angle of attack rate. In total there are four parameters that can be used for "tuning" this function. The parameters a_1 and α^* influence the steady conditions of the stall model, i.e., $\dot{\alpha} = 0$. The values of τ_1 and τ_2 relate to the dynamic effects of the stall, i.e., $\dot{\alpha} \neq 0$. An overview of the effects each parameter has, is given below:

- a_1: Influences the abruptness of the stall. A low value of a_1 indicates that the stall is not very abrupt, while a high value does the opposite.
- α^*: The angle of attack at which the flow separation point equals a half. An increase in α^* indicates a higher critical angle of attack.
- τ_1: Influences the transient effects of the flow separation point, it is essentially a time delay in the flow separation point. A high value indicates a large time delay.
- τ_2: Determines the hysteresis effect, a higher value indicates that flow separation occurs later with a positive angle of attack rate ($\dot{\alpha}$).

Visualizations of these different parameters on the $C_L - \alpha$ curve are given in Figures 8, 9, 10 and 11. In Figures 8 and 9 the flow separation point is described as X_0, as shown on the y-axis in the right figures. This indicates a steady flow separation point, i.e. $\dot{\alpha} = 0$. Most of the flown stalls are quasi-steady, and thus during approach to stall $\dot{\alpha} \approx 0$. This makes it rather difficult to estimate τ_1. In fact, estimating the value of τ_1 is not possible using only quasi-steady stall maneuvers, without correlation with other parameters.[28]

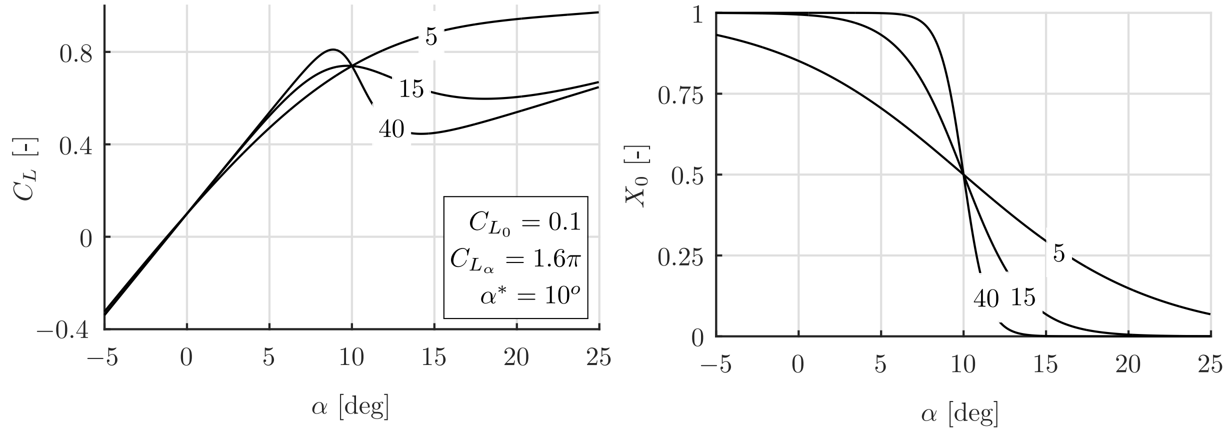

Figure 8. Effect of a_1 on the lift coefficient and flow separation point in steady conditions. (Adapted from Fischenberg[28] and Dias[15])

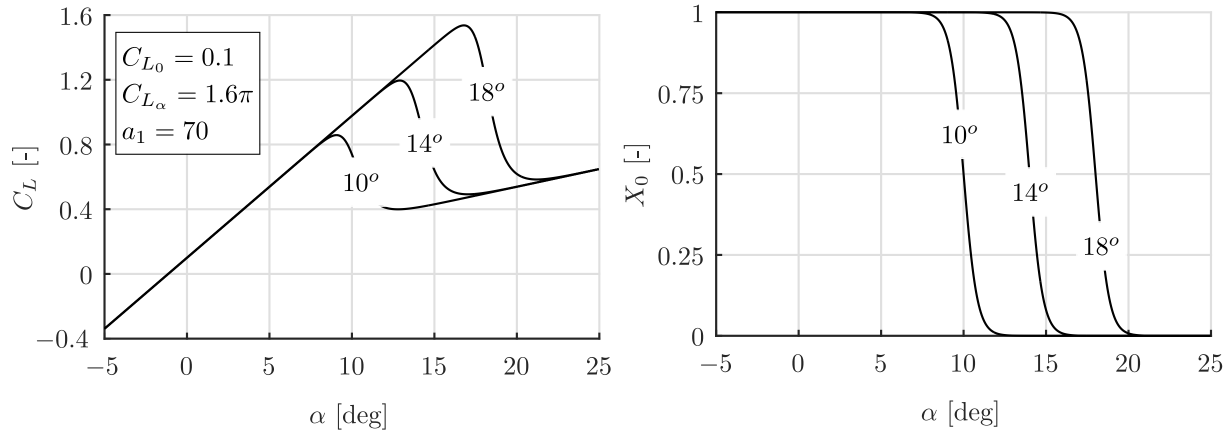

Figure 9. Effect of α^* on the lift coefficient and flow separation point in steady conditions. (Adapted from Fischenberg[28] and Dias[15])

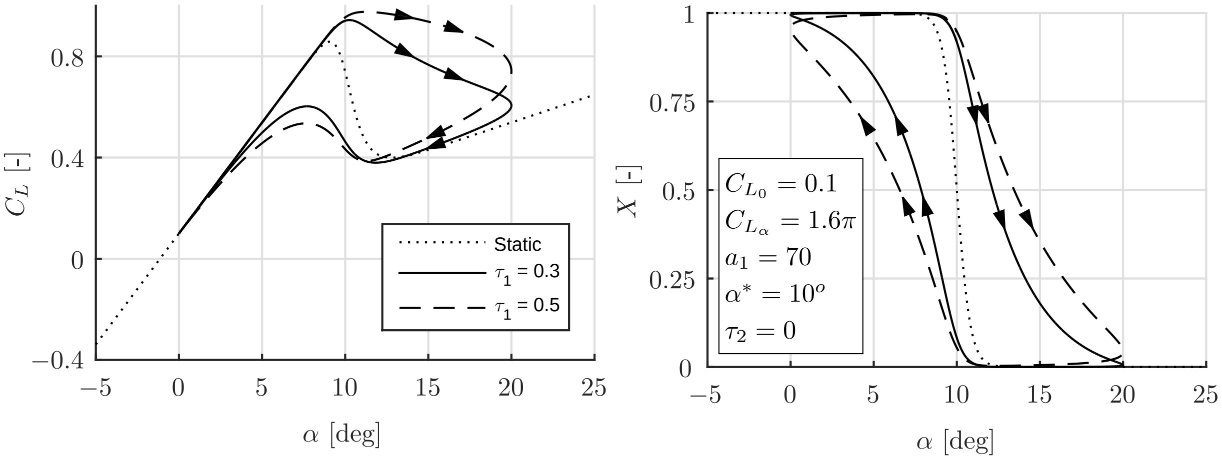

Figure 10. Effect of τ_1 on the lift coefficient and flow separation point in steady conditions. (Adapted from Fischenberg[28] and Dias[15])

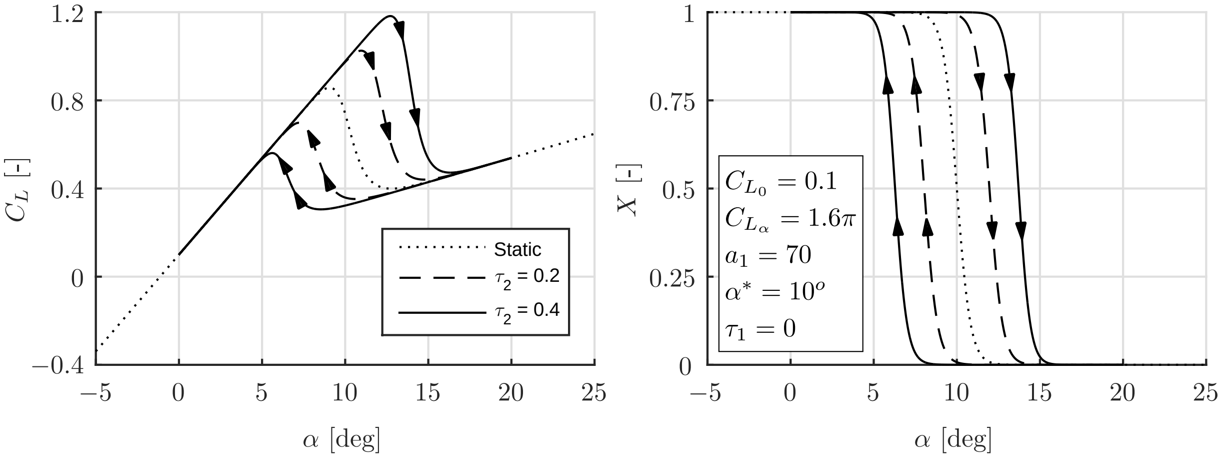

Figure 11. Effect of τ_2 on the lift coefficient and flow separation point in steady conditions. (Adapted from Fischenberg[28] and Dias[15])

1. Longitudinal

The low-frequency longitudinal forces and moment are modeled using Eqs.(10), (11) and (12). The damping terms, i.e., terms w.r.t. the pitch rate were omitted from the equations. As will be shown in Section V, the identification of C_{L_q} is feasible, the parameters C_{D_q} and C_{m_q}, however, are not identifiable.

$$C_L = C_{L_0} + C_{L_\alpha} \left\{ \frac{1+\sqrt{X}}{2} \right\}^2 \alpha \tag{10}$$

$$C_D = C_{D_0} + C_{D_\alpha}\alpha + C_{D_X}(1-X) \tag{11}$$

$$C_m = C_{m_0} + C_{m_\alpha}\alpha + C_{m_{\delta_e}}\delta_e + C_{m_X}(1-X) \tag{12}$$

2. Lateral

Due to the unavailability of the side slip measurement, an alternate model structure is used for modeling lateral effects during stall.[29] This is done by calculating the lift and drag for both wings separately. The difference in lift and drag causes a rolling and yawing moment, which can be modeled using Eqs. (13) and

(14), where Δy is the effective lever arm. The control effectiveness, i.e., $C_{l_{\delta_a}}$ and $C_{n_{\delta_r}}$, could be extracted from the original flight model, with a possible reduction to model the reduced control effectiveness.

$$C_l = \left(C_{Z_{\text{right}}} - C_{Z_{\text{left}}}\right) \Delta y \tag{13}$$

$$C_n = \left(C_{X_{\text{left}}} - C_{X_{\text{right}}}\right) \Delta y \tag{14}$$

To calculate the lift for both wings separately a distinction can be made between the angle of attack experienced by both wings. Effects such as the side slip angle, roll rate and yaw rate all have effect on the local angle of attack on the aircraft. The following distinctions are made for the simulation:

1. **Angle of side slip:** For an aircraft with a low wing configuration a positive side slip angle will decrease the angle of attack on the forward wing and increase the angle of attack on the backward wing.[30] This effect is caused by the wing-fuselage interaction, as shown in Figure 12. Although this interaction does have an effect on the local angle of attack it is difficult to model, especially without a side slip measurement.

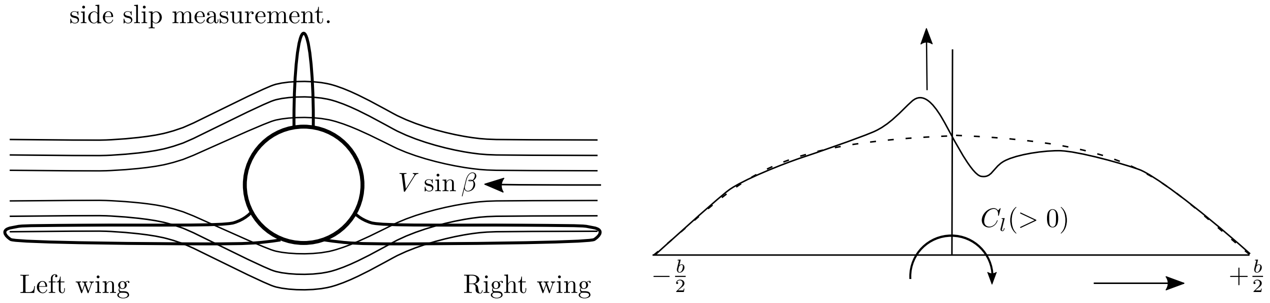

(a) Airflow over the aircraft

(b) Pressure distribution over the wings

Figure 12. Rolling moment caused by wing-fuselage interaction in side slipping flight. (Adapted from Mulder[30])

Another effect is caused by the wing dihedral.[30] Assuming that the aircraft has a side slip from the right, as shown in in Figure 13, it can be seen that the normal velocity on the wings can be calculated as follows:

$$V_{n_l} = w \cos\Lambda - v \sin\Lambda \quad \text{and} \quad V_{n_r} = w \cos\Lambda + v \sin\Lambda \tag{15}$$

The local angle of attack can then be calculated using Eq. (16), following from Figure 13:

$$\alpha_{w_l} = \arctan\left(\frac{V_{n_l}}{u}\right) \quad \text{and} \quad \alpha_{w_r} = \arctan\left(\frac{V_{n_r}}{u}\right) \tag{16}$$

So with a positive dihedral and a positive side slip, the right wing will experience a higher local angle of attack than the left wing.

2. **Roll rate:** When the aircraft is rolling, the down going-wing experiences a higher angle of attack than the up-going wing. Normally this would damp the rolling motion of the aircraft, but at attitudes near the critical angle of attack, the down-going wing could stall while the up-going wing does not. This phenomena is called auto rotation. The change in the angle of attack can be calculated using Eq. (17), where y is the position at the wing:[30]

$$\Delta\alpha_{w_l} = -\frac{pb}{2V}\frac{y - y_{c.g.}}{b/2} \quad \text{and} \quad \Delta\alpha_{w_r} = \frac{pb}{2V}\frac{y - y_{c.g.}}{b/2} \tag{17}$$

3. **Yaw rate:** A yawing moment also causes a difference in force generated by the two wings. This is caused by the rotation in which the outer board wing locally experiences a higher velocity than the inboard wing. The local velocity on the wing changes as follows:[30]

$$\frac{\Delta V_l}{V} = \frac{rb}{2V}\frac{y}{b/2} \quad \text{and} \quad \frac{\Delta V_r}{V} = -\frac{rb}{2V}\frac{y}{b/2} \tag{18}$$

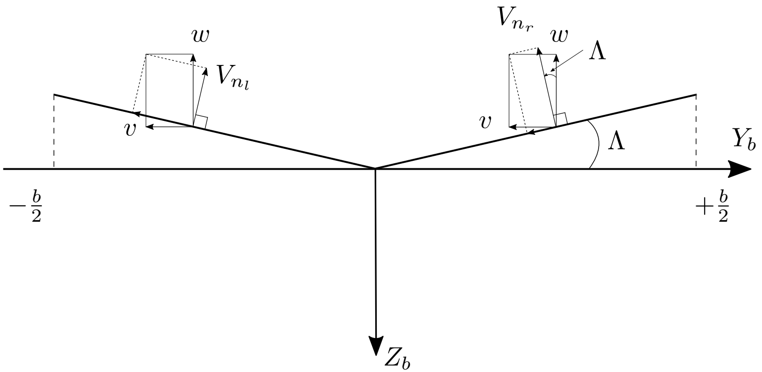

(a) Backview of the induced velocity at both wings

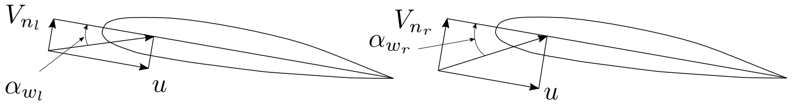

(b) Sideview of the induced velocity at both wings

Figure 13. Effect of side slip on an aircraft with wing dihedral. (Adapted from Mulder[30])

B. Buffet Model

The other model that was obtained from the flight data is the high-frequency buffet model. When the flow starts separating from the wing, a vibration can be felt throughout the aircraft. This vibration was measured by the AHRS, which was used for developing a buffet model. The time signal of the vibration was transformed to the frequency spectra, to obtain the power spectral density (PSD) for each stall. To obtain a more accurate results these power spectral densities were averaged to obtain one periodogram. Before doing so, however, it was first investigated whether altitude had a significant effect on the PSD. As shown in Figure 14, there is no clear effect of altitude on the stall buffet. Therefore one stall buffet for all altitudes will be modeled.

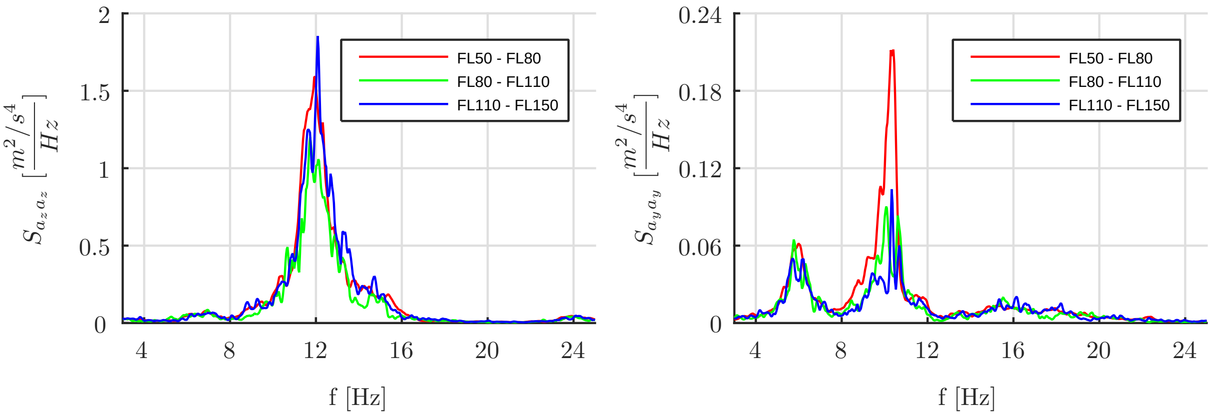

Figure 14. Effect of the altitude on the stall buffet.

As shown in Figure 14, the PSD of the vertical acceleration (a_z) is approximately ten times larger than the lateral acceleration (a_y). This indicates that the vertical acceleration is the most dominant. The reason for not showing the PSD for the acceleration in x-direction is that this signal is effectively zero. Furthermore it can also be seen already in Figure 14 that the vertical buffet has one dominant frequency, around 12 Hz. The lateral buffet has two dominant frequencies: one at 6 Hz and one at 10 Hz

The buffet model is assumed to be a white noise signal, which is passed through a shaping filter. This model structure is shown in Eq. (19). The stall buffet frequency response function ($H\left(j\omega\right)$) can be estimated from the PSD as shown in Figure 14, assuming that the white noise input signal has an intensity of one.

$$S_{yy} = S_{hh} \cdot S_{uu} = \left|H\left(j\omega\right)\right|^2 S_{uu} \qquad (19)$$

The stall buffet models are created using a second-order filter, as given in Eq. (20). The resonance frequency of a second order filter can be used to create a bandpass filter. For the vertical buffet model one bandpass filter is used, whereas for the lateral buffet model two bandpass filters were added together, as shown in Figure 15.

$$H\left(j\omega\right)=\frac{H_0 w_0^2}{\left(j\omega\right)^2+\frac{w_0}{Q_0}j\omega+w_0^2} \tag{20}$$

C. Parameter Estimation

Both the aerodynamic model and the buffet model are nonlinear functions, and thus estimating their parameters becomes a nonlinear optimization problem. The solver that was used, is based on a trust-region-reflective optimization algorithm.[31] One of the major problems associated with nonlinear optimization, is that a final value could be a local optimum. To increase the chance of finding the global optimum two techniques were applied simultaneously:

1. The estimated parameters were constrained when possible. For example it is known that: $C_{D_0} > 0$, otherwise the aircraft would be a perpetual motion machine. Another constraint is that $C_{L_\alpha} > 0$. Using such constraints the optimization problem becomes bounded and it is more likely that a global optimum will be found.
2. The optimization algorithm was run for multiple sets of initial conditions. A nonlinear optimization problem always needs a set of initial conditions, these conditions influence the possibility of finding the global optimum. When a large set of initial conditions is used, the solution with the lowest mean squared error can be chosen to be the best estimate. The set of initial conditions was chosen by first running a large set of randomly picked initial conditions through the cost function. Then a certain amount, e.g., 500, initial conditions were chosen from the larger set. This is done by obtaining the 500 initial conditions, which gave the lowest value for the cost function.

Since most stalls were quasi-steady they could not be used for estimating the transient effects (τ_1). Another method for estimating the value of τ_1 was found instead. To do so first all parameters, including the hysteresis constant (τ_2) were estimated using a nonlinear least squares approach.[32] During this estimation the value of τ_1 was kept fixed. The cost function that was used is given in Eq.(21), with X being defined as in Eq.(9). The constraints are as given in Table 3, as well as the initial conditions. The initial conditions were chosen as a base value plus a random number selected from the standard normal distribution, with a standard deviation of σ.

$$\begin{aligned} J &= \left(C_{L_0}+C_{L_\alpha}\left\{\frac{1+\sqrt{X}}{2}\right\}^2\alpha-C_L\right)^2 \\ &+ \left(C_{D_0}+C_{D_\alpha}\alpha+C_{D_X}\left(1-X\right)-C_D\right)^2 \\ &+ \left(C_{m_0}+C_{m_\alpha}\alpha+C_{m_{\delta_e}}\delta_e+C_{m_X}\left(1-X\right)-C_m\right)^2 \end{aligned} \tag{21}$$

Table 3. Constraints and initial conditions for the optimization algorithm

Parameter	C_{L_0}	C_{L_α}	a_1	α^* [rad]	τ_2 [s]	C_{D_0}	C_{D_α}	C_{D_X}	C_{m_0}	C_{m_α}	$C_{m_{\delta_e}}$	C_{m_X}
Lower-bound	-2	0	0	0	0	0	0	0	-2	-2	-2	-2
Upper-bound	2	2π	120	0.5	2	2	2	2	2	0	0	0
Initial condition	0.5	3.0	50	0.2	0.25	0.1	0.5	0.4	0.0	-0.5	-0.3	-0.2
σ	0.5	2.0	50	0.2	0.25	0.1	0.5	0.4	0.2	0.5	0.3	0.2

When these parameters, also shown in Figure 17, were estimated they were used in the stall buffet model.

The buffet is driven by a white noise signal, with a PSD equal to one. This signal is then shaped by a bandpass filter, corresponding to the stall buffet. To increase the amplitude of the stall buffet as a function of the flow separation point, the buffet signal will be multiplied with $(1-X)$, where X is determined using Eq.(9). This, however, decreases the amplitude of the original signal, which can be corrected for using a gain. This gain can later on also be used for tuning the amplitude, such that the accelerations are in within limits of a full motion simulator. Finally the stall buffet will have a certain threshold before the signal is activated, e.g., the buffet will only be felt in case $X < 0.89$. A schematic overview of this buffet signal generator is given in Figure 15.

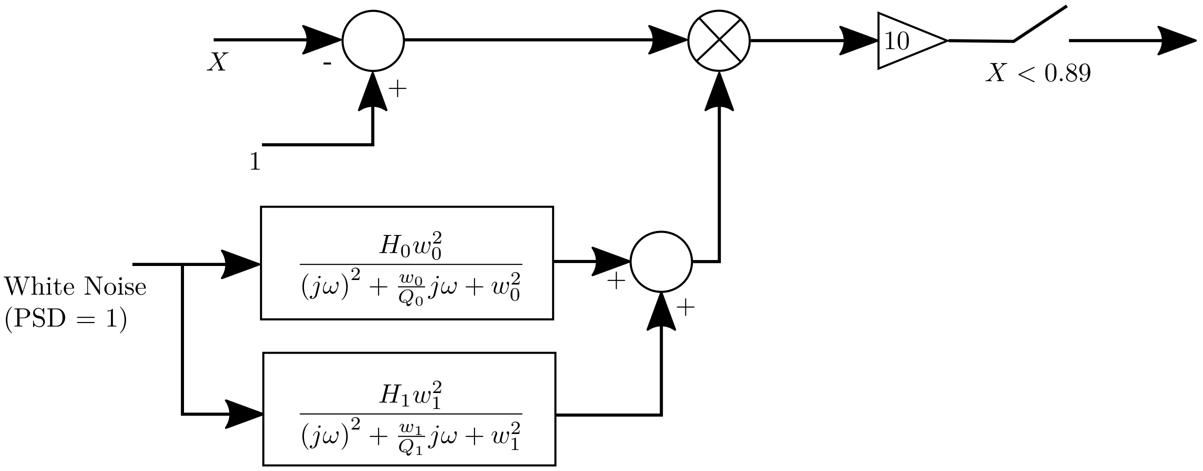

Figure 15. Effect of the flow separation point on the stall buffet, example given of the lateral stall buffet model

During the validation of the stall buffet it was found that, most of the time, the vibration of the model stopped earlier than from the flight data. This difference indicated that a transient effect was not taken into account in the stall model buffet. This transient effect is essentially the value of τ_1 and thus this allows for estimating τ_1 based on the buffet acceleration data.

To do so an algorithm was made to detect when the stall buffet was active. First the acceleration was filtered by a high pass filter. Then the absolute value of the high-pass filtered acceleration is taken, shown as the blue line in Figure 16a. This signal is then low-pass filtered to obtain a general trend of the stall buffet, as shown by the black line in Figure 16a. This trend was then compared to a certain threshold (red line in Figure 16a) , in this case 0.4 m/s^2. When the low-pass filtered absolute acceleration data (black line) got above the threshold (red line), the buffet was said to be active, otherwise the buffet was non-active. The same method was applied for the acceleration data obtained by an initial stall buffet model, as shown in Figure 16b. The activate and non-active sections from both the flight data and the stall model are compared, as shown in Figure 16c. The first trigger (i.e., from non-active to active) was used to obtain the onset flow separation point. This was done by calculating the stall model buffet for a set of thresholds. Then the threshold which matched the first triggers of both the model and the flight data the closest, was chosen as the best threshold.

The lag, i.e., τ_1, was estimated by calculating the cross correlation of the both the "active/ non-active" signal (as shown in Figure 16c). The estimated delay was given by the negative of the lag, for which the cross-correlation has the largest absolute value. In case more than one lag was found for the largest absolute value of the cross-correlation, the delay was chosen to be the smallest (in absolute value) of these lags, an example of this is given in Figure 16d, where the time delay was found to be 0.345 s. This was done for all model identification data sets, for a large set of random seeds for the white noise signal, which drives the stall buffet model.

Initially the stall parameters, however, were estimated with the assumption that τ_1 was zero. To obtain a better estimate the optimization algorithm, which obtains all parameters except for τ_1, was run again. This time however with the value of τ_1 as found from the stall buffet analysis. After doing so these parameters were used again to re-estimate τ_1. This process is iterated, until the change in τ_1 is sufficiently small. This iterative process is also shown in Figure 17.

As shown by Eqs. (10), (11) and (12), the dependent variables are the longitudinal force, vertical force and the pitch moment. These values cannot be measured directly and thus have to be calculated from the aircraft equations of motion:

$$C_X = \frac{m a_x}{\frac{1}{2}\rho V_{TAS}^2 S} - \frac{T}{\frac{1}{2}\rho V_{TAS}^2 S} \tag{22}$$

$$C_Z = \frac{m a_z}{\frac{1}{2}\rho V_{TAS}^2 S} \tag{23}$$

$$C_m = \frac{1}{\frac{1}{2}\rho V_{TAS}^2 S \bar{c}} \left(I_{yy}\dot{q} - \left(I_{zz} - I_{xx}\right) rp - I_{xz}\left(r^2 - p^2\right)\right) \tag{24}$$

From Eqs. 22 and 23, the lift- and drag force can be calculated, using the standard transformation from body to aerodynamic frame, assuming zero side slip:

$$C_L = -C_Z \cos\left(\alpha\right) + C_X \sin\left(\alpha\right) \tag{25}$$

$$C_D = -C_Z \sin\left(\alpha\right) - C_X \cos\left(\alpha\right) \tag{26}$$

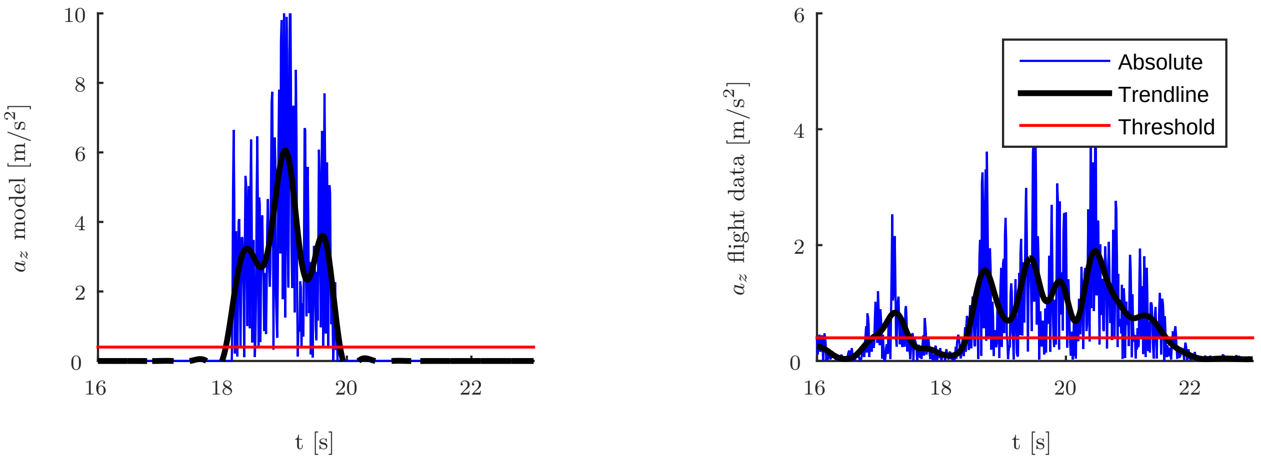

(a) Acceleration from flight data

(b) Acceleration from buffet model

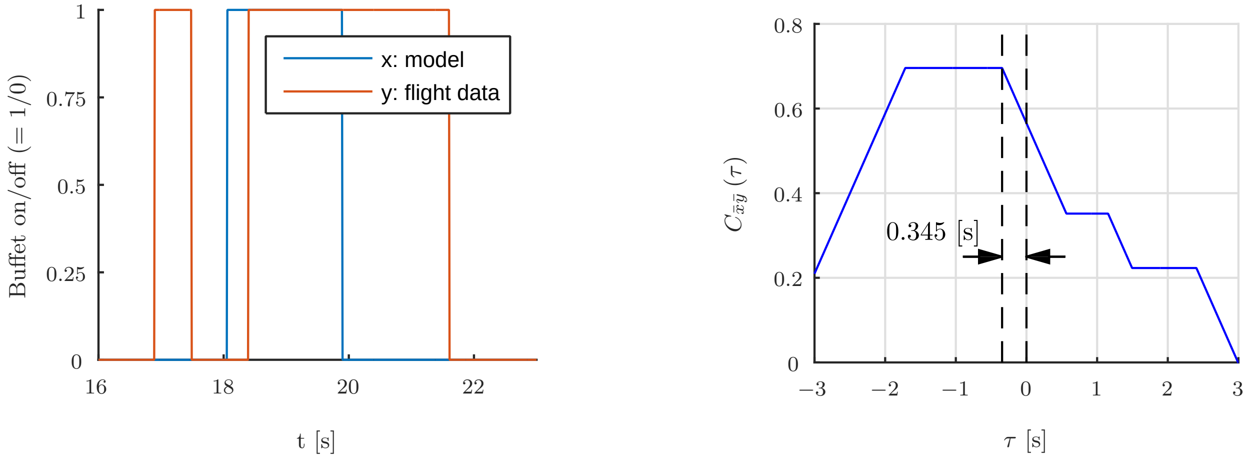

(c) Activation of both flight data and model

(d) Cross correlation between flight data and model

Figure 16. Graphical overview of the steps being taken to estimate τ_1

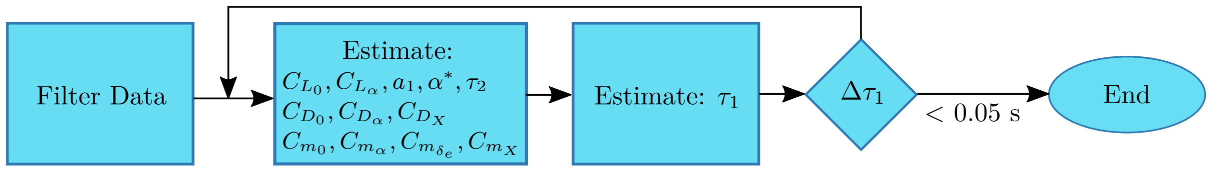

Figure 17. Method of how the parameters were estimated

Lastly the moment equation has to be corrected for the moment caused by the engine. The engine is located above the center of gravity, this distance (Δz) is on average approximately 0.5 meters. This moment caused by the engine causes an extra nose down moment and thus the moment induced by the engine has to be added to the moment as calculated by Eq. (24), which is done as follows:

$$C_{m_{\text{corr}}} = C_m + \frac{T\Delta z}{\frac{1}{2}\rho V_{TAS}^2 S\bar{c}} \tag{27}$$

D. Blending

The last part is to blend the stall model with the aerodynamic model for normal flight. This is done by gradually replacing the output (i.e. the aerodynamic forces and moments) of the baseline model, with the stall model. An example of such a blending function is given in Figure 18. It can be seen that at the lower angles of attack, the baseline model dominates the forces and moments. At a high angle of attack, the stall model starts to be more dominant.

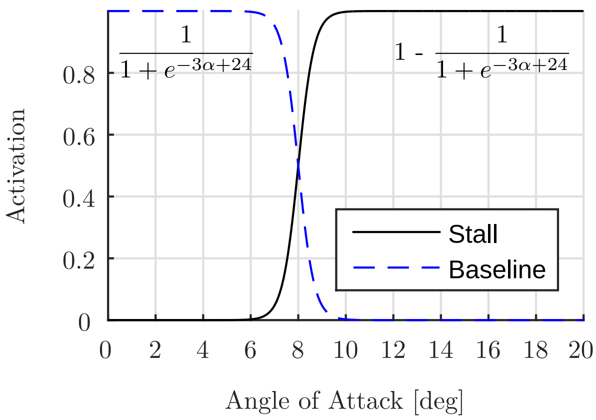

Figure 18. The activation for blending the two models together.

V. Results

A. Flight Path Reconstruction

An example of the state estimation results is given in Figures 19 and 20. The former shows the raw and reconstructed measurements. It can be noticed that the alpha-vane model seems to work correctly, since the signal is shifted approximately 0.2 seconds back in time. Another interesting note is that of the pseudo-beta. During the stall the aircraft has a small bank angle, which most likely causes a small side slip angle. As can be seen in Figure 19, the input data for the side slip angle is zero, whereas the reconstructed value is not.

In Figure 20 the estimate of the states, which are not directly measured, can be seen. A simple check for convergence is to run the Kalman filter for different initial conditions. When these signals still converge to one value it can be assumed that the state reconstruction is indeed converging. An example of this was shown in Figure 7. It is not shown, however, in Figure 20 since all lines coincided within a second. Furthermore it can be seen that the fuselage upwash component on the angle of attack measurement ($C_{\alpha_{up}}$) is not zero. This indicates that body induced velocities are definitely present at the alpha-vane.

The bias terms and the wind terms on the other hand seem to be varying a little. It must be noticed, however, that these terms most likely do not only contain the pure biases, but other effects as well. These effects could for example be: a small misalignment in the IMU, an error in correcting the linear accelerations for the center of gravity and a high value of dilution of precision (DOP) in the GPS system.

Another interesting effect is the bias term in the yaw rate (λ_r), which seems to be rather high and also changes during the stall maneuver. A logical explanation seems to be that there is not enough excitation in yaw direct, making it difficult to identify.

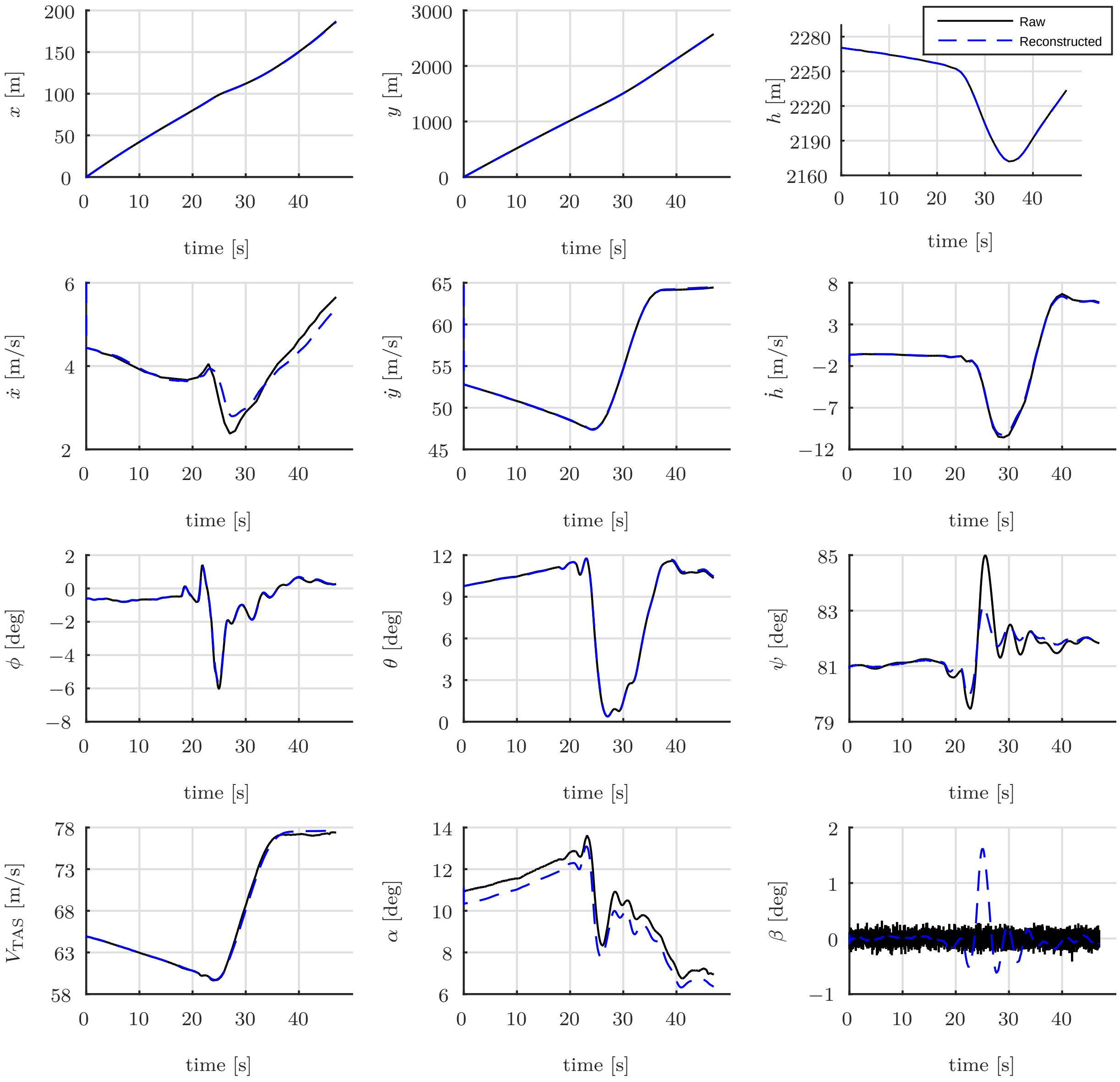

Figure 19. Example of FPR results for a stall occurring at t = 23 s.

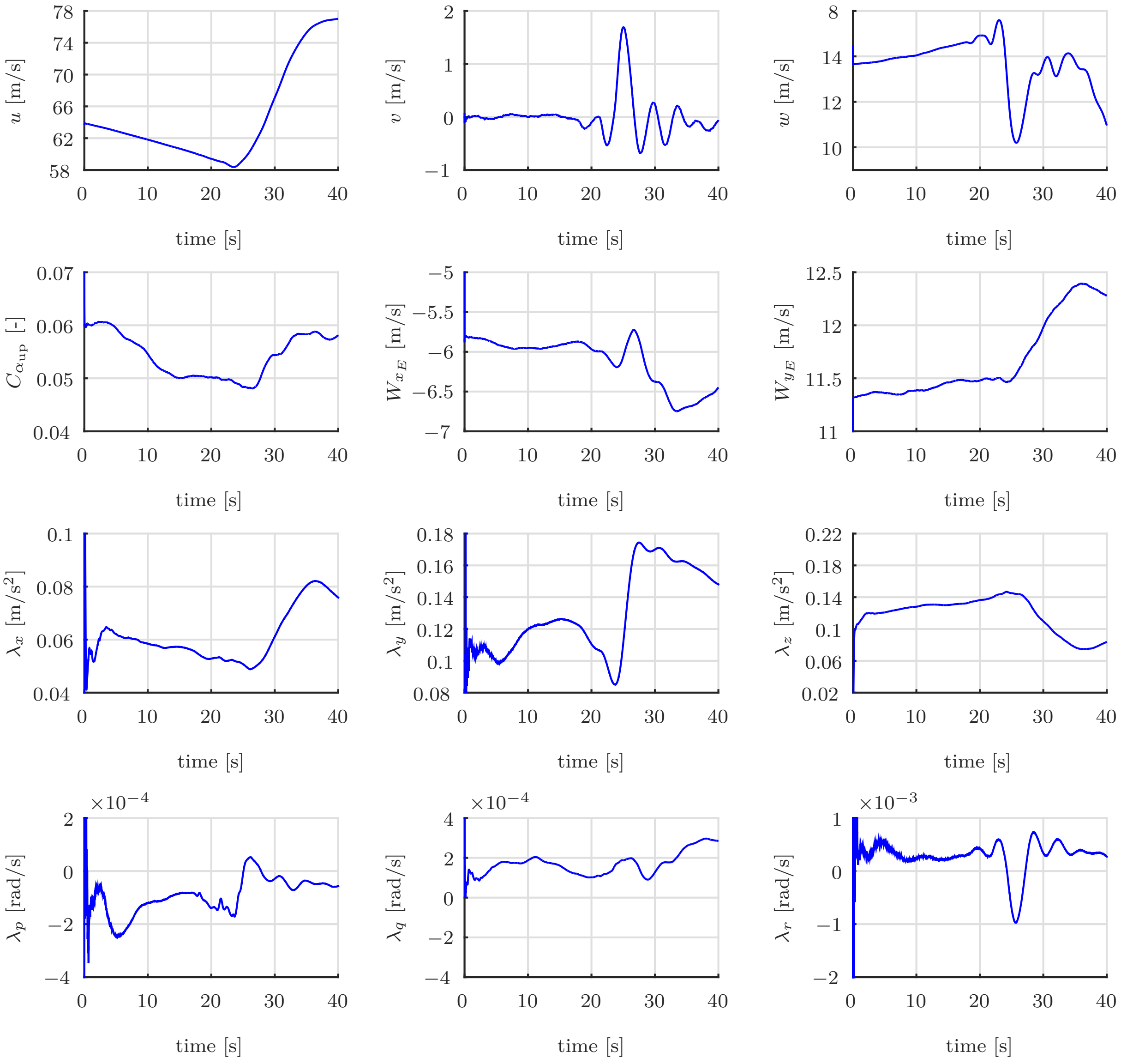

Figure 20. Example of the estimated state for a stall occurring at t = 23 s.

B. Aerodynamic Model

In Figures 21, 22 and 23 the estimated parameters can be found as a function of altitude. As can be noticed, with the quasi-steady stall approaches the parameters for the lift can be estimated rather well, as indicated by the Cramer-Rao lower bounds. The values for the drag (Figure 22) and moment coefficients (Figure 23), however, show a lot more variance. This indicates that the parameters for the drag- and moment coefficients are more uncertain.

Another method for validating the parameters is comparing them to the literature. In Table 4 the flow separation point parameters from other literature is given. The found values of a_1 and α^* as given in Figure 21 correspond to the found values in literature. The value of τ_2 on the other hand (with $\bar{c} = 2.09$ m and $V_{\text{stall}} = 59$ m/s), is approximately three times higher than the values found in literature.

Table 4. Flow separation point parameters from for other aircraft and airfoils

Parameter	Embraer AT-26 Xavante[33]	VFW-614[28]	C-160[28]	NACA 0015[34]
a_1	25	14.9	25.7	-
α^* [rad]	0.25	0.34	0.36	-
$\tau_1 \frac{\bar{c}}{V}$ [s]	-	15.6	14.5	0.52
$\tau_2 \frac{\bar{c}}{V}$ [s]	-	4.45	3.46	4.5

Other values that were found were the semi-empirical coefficients C_{D_X} and C_{m_X}. For the Embraer AT-26 Xavante, at Mach = 0.4, these are 0.2 and -0.08 respectively.[33] The value of C_{D_X} for the VFW-614 is 0.22 and for the C-160 approximately 0.40.[28] The values that were found, as shown in Figures 22 and 23 are approximately 0.2 and -0.12 for C_{D_X} and C_{m_X} respectively, corresponding well with the values found in literature.

Lastly for the Embraer AT-26 Xavante a control effectiveness ($C_{m_{\delta_e}}$) was found of approximately -0.4,[33] which corresponds to the value found in Figure 21.

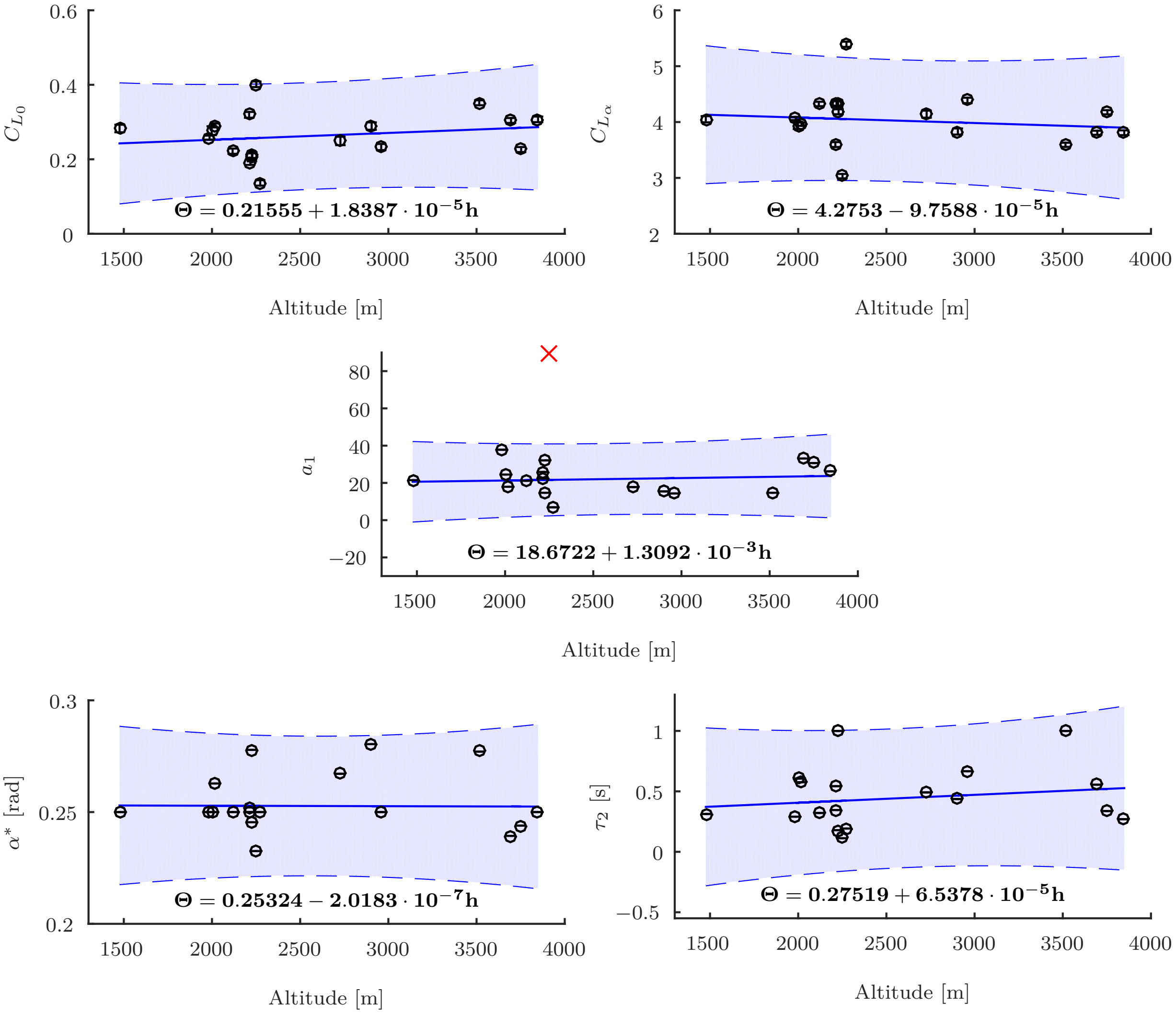

Figure 21. Lift coefficient parameters for the Cessna Citation II

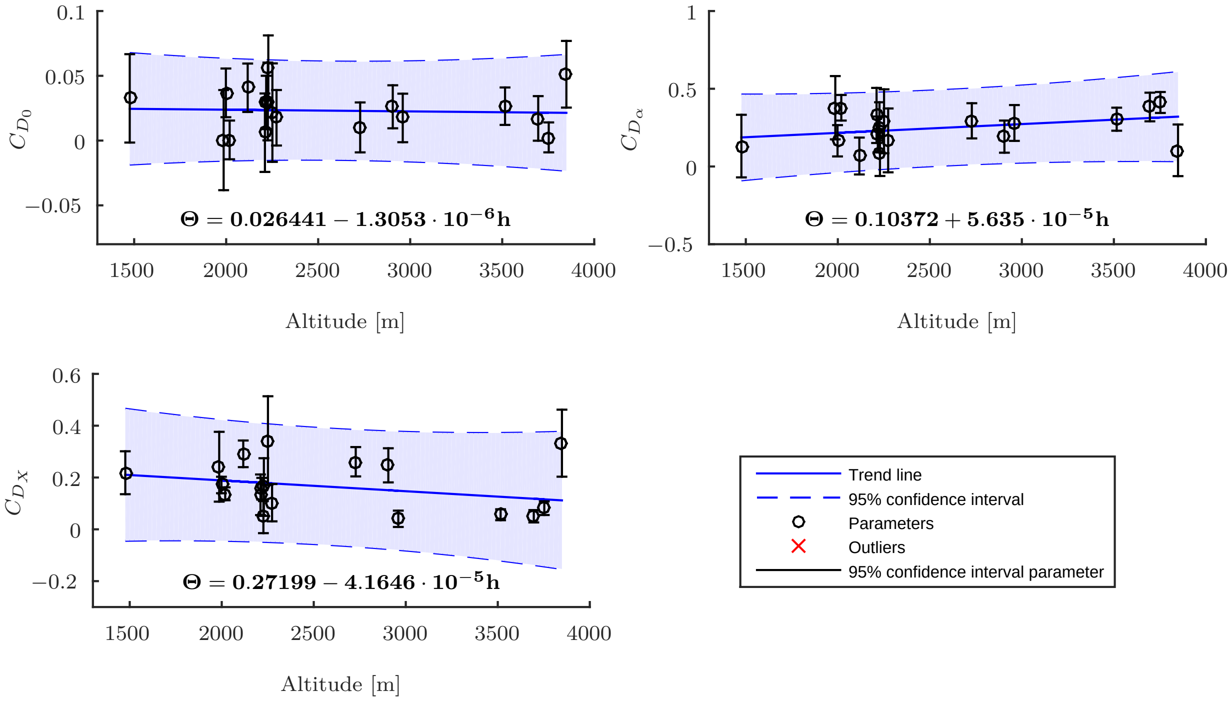

Figure 22. Drag coefficient parameters for the Cessna Citation II

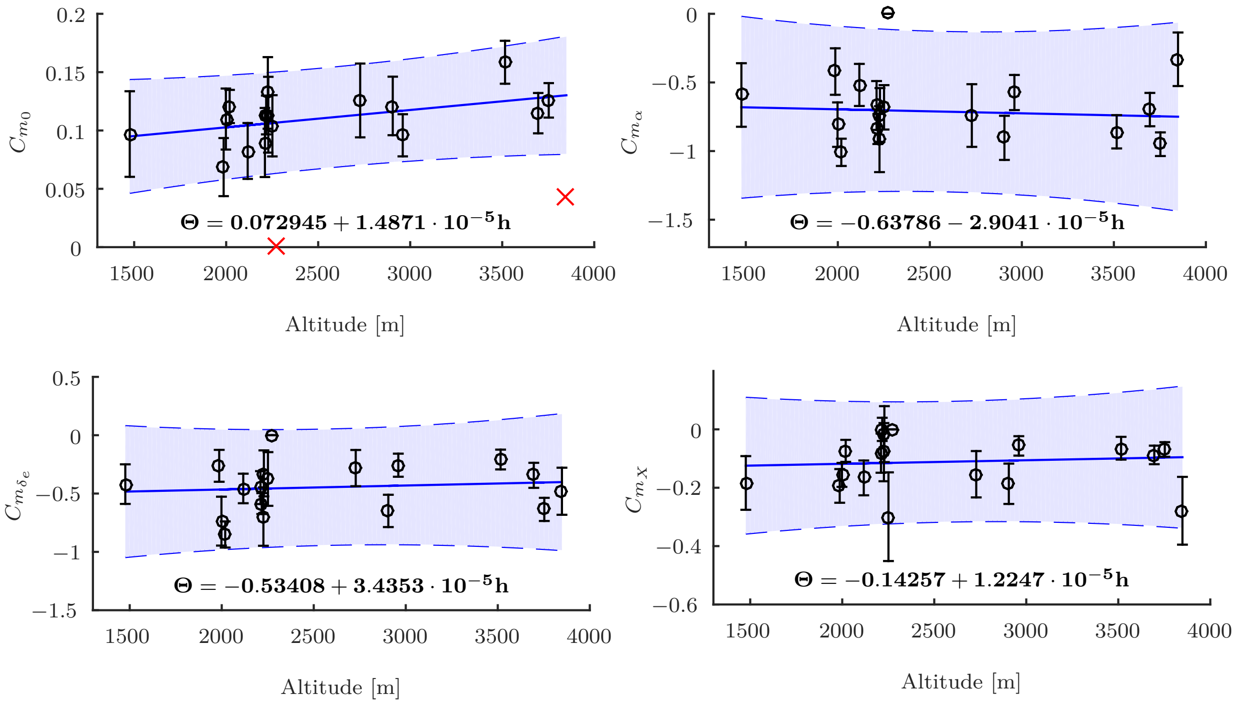

Figure 23. Moment coefficient parameters for the Cessna Citation II

Another interesting statistic is the cross correlation between parameters. A high absolute value (close to 1 or -1) indicates that the parameters are closely coupled. A high value, according to Klein et al.[27] has an absolute value greater than 0.9. Looking at Tables 5, 6 and 7 the only highly coupled parameters are the constant term ($C_{L_0}, C_{D_0}, C_{m_0}$) and the term w.r.t. the angle of attack. This high negative correlation between the intercept ($C_{L_0}, C_{D_0}, C_{m_0}$) and the slope ($C_{L_\alpha}, C_{D_\alpha}, C_{m_\alpha}$) is a result of the fact that all the data points are far away from $\alpha = 0$. When the slope increases somewhat the intercept has to decrease, otherwise the estimated output would be too large. To decrease this correlation more dynamic input maneuvers, such as an elevator doublet could be used. Another method could be to include a dynamic maneuver at a lower angle of attack. These two methods increase the angle of attack range, resulting in a lower correlation between the slope and the intercept. All the other values are below a value of 0.9, indicating that these parameters can be sufficiently dissociated.[27]

Table 5. Correlation matrix for the parameters corresponding to the lift coefficient

	C_{L_0}	C_{L_α}	a_1	α^*	τ_2
C_{L_0}	1.0000	-0.9916	-0.0214	0.0104	-0.0185
C_{L_α}	-	1.0000	-0.0187	-0.0134	0.0185
a_1	-	-	1.0000	-0.2361	-0.4101
α^*	-	-	-	1.0000	-0.3089
τ_2	-	-	-	-	1.0000

Table 6. Correlation matrix for the parameters corresponding to the drag coefficient

	C_{D_0}	C_{D_α}	C_{D_X}
C_{D_0}	1.0000	-0.9794	0.2953
C_{D_α}	-	1.0000	-0.4424
C_{D_X}	-	-	1.0000

Table 7. Correlation matrix for the parameters corresponding to the moment coefficient

	C_{m_0}	C_{m_α}	$C_{m_{\delta_e}}$	C_{m_X}
C_{m_0}	1.0000	-0.8576	0.0236	0.4242
C_{m_α}	-	1.0000	0.4513	-0.3580
$C_{m_{\delta_e}}$	-	-	1.0000	-0.2415
C_{m_X}	-	-	-	1.0000

The terms w.r.t. the pitch rate were omitted from the look up tables. The main reason for doing so is because the terms: C_{D_q} and C_{m_q} could not be estimated from quasi-steady stalls. As shown in Figure 24, these parameters have a large variance. The worst case is for the drag coefficient, in which half of the time the value is negative and the other half positive. Another interesting fact is that C_{m_q} is estimated to be positive, whereas a negative value is expected, as is the case for the Embraer AT-26 Xavante.[33] The only parameter w.r.t. the pitch rate which could be identified is C_{L_q}, the reason for not doing so is threefold. First it will make the aerodynamic model structure less clear by using a pitch rate term in one equation and not in the others. Secondly the coefficient of determination on the identification set hardly improves. Without the pitch rate term the average coefficient of determination on the identification set is **0.8712**, whereas with the pitch rate term this value is **0.8891**. Lastly in the flow separation point both a_1, and more directly τ_2 influence the behavior w.r.t. the angle of attack rate. The angle of attack rate and pitch rate, also with quasi-steady stalls, are still very much correlated. Since the angle of attack rate is used, indirectly a damping term such as C_{L_q} is used.

Good practice is that identified models should also be validated using data which was not used for model fitting. During this research approximately 75% of the data was used for parameter estimation and 25% for validation. The validation data in the Mach vs. Angle of Attack plane is shown in Figure 26, indicating where the flight model is validated. Three of the validation sets are shown in Figure 25, indicating a best fit, average fit and the worst case fit. As shown the general trends between the flight data and the model data correspond. The lift coefficient shows the best fit. The drag coefficient is somewhat overestimated, but except for the best case it shows a better fit than for the pitch moment coefficient. The pitching moment is difficult to predict with quasi-steady stall maneuvers. One possible method of increasing the moment

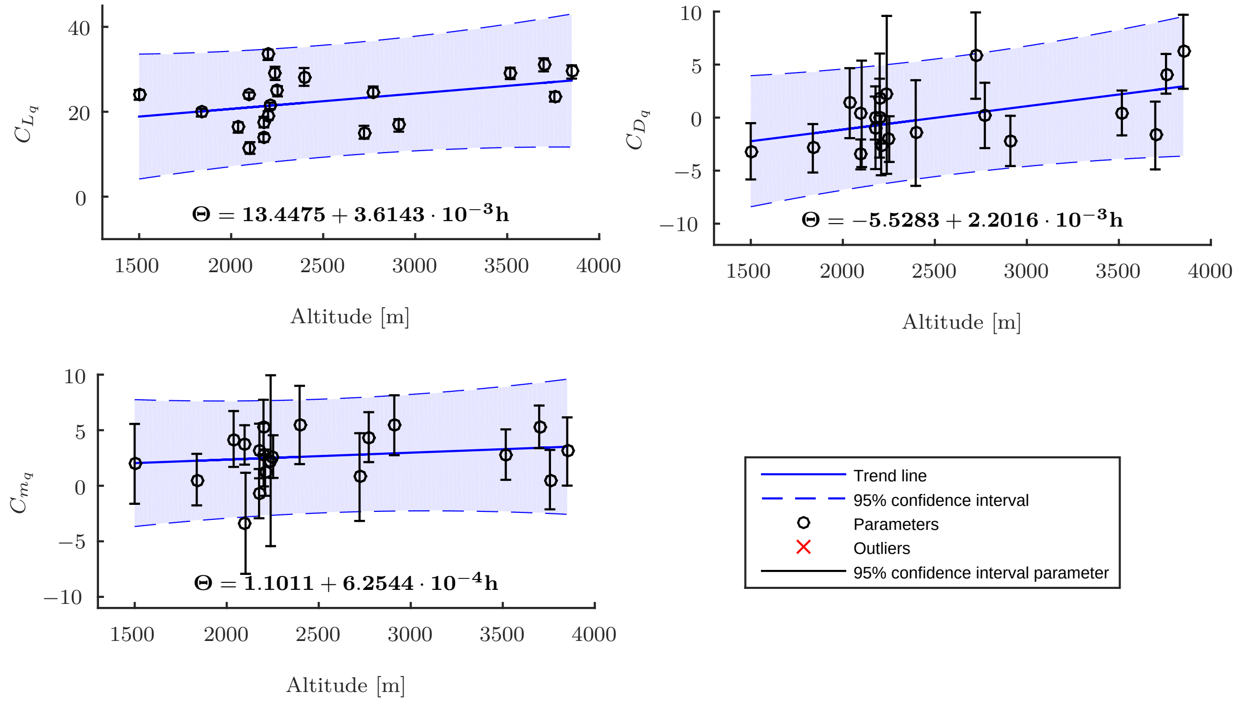

Figure 24. Aerodynamic terms w.r.t. the pitch rate

coefficient model is to use dynamic stall maneuvers, with e.g., elevator doublets during approach to stall. The dynamic stalls that were executed for this research, i.e. a symmetrical stall using a pull-up maneuver with a load factor of 1.3g, did not show better fitting on the identification data compared to the quasi-steady stalls.

C. Buffet Model

The stall buffet is obtained by Fourier analysis of the acceleration signals, to obtain the periodograms. These power spectral density estimates can be used to fit frequency response functions for the stall buffet model. The PSD of the raw data and the fitted models, for both the vertical and lateral acceleration, are shown in Figure 27. The stall buffet in vertical direction has one dominant frequency around 12 Hz, whereas the lateral acceleration has two peak frequencies: one at 10 Hz and one at 6 Hz. The coefficient of determination (R^2) for the vertical buffet model is **0.976** and for the lateral acceleration **0.771**. In Tables 8 and 9 the parameters for the vertical and lateral buffet models can be found. As can be noticed the Cramer-Rao lower bounds are rather low, which together with a high value of the coefficient of determination indicates that the model is a good fit.

Table 8. Parameters for the vertical acceleration

	unit	β	σ	$\frac{\sigma(\beta)}{\beta} \times 100$
H_0	[-]	0.05	3.57e-04	0.65
ω_0	[rad/s]	75.92	2.83e-02	0.04
Q_0	[-]	8.28	9.15e-04	0.01

Table 9. Parameters for the lateral acceleration

	unit	β	σ	$\frac{\sigma(\beta)}{\beta} \times 100$
H_0	[-]	0.02	1.15e-03	5.86
ω_0	[rad/s]	36.43	2.43e-01	0.67
Q_0	[-]	4.19	1.77e-02	0.42
H_1	[-]	0.01	1.39e-04	1.14
ω_1	[rad/s]	64.71	2.70e-02	0.04
Q_1	[-]	11.99	1.13e-03	0.01

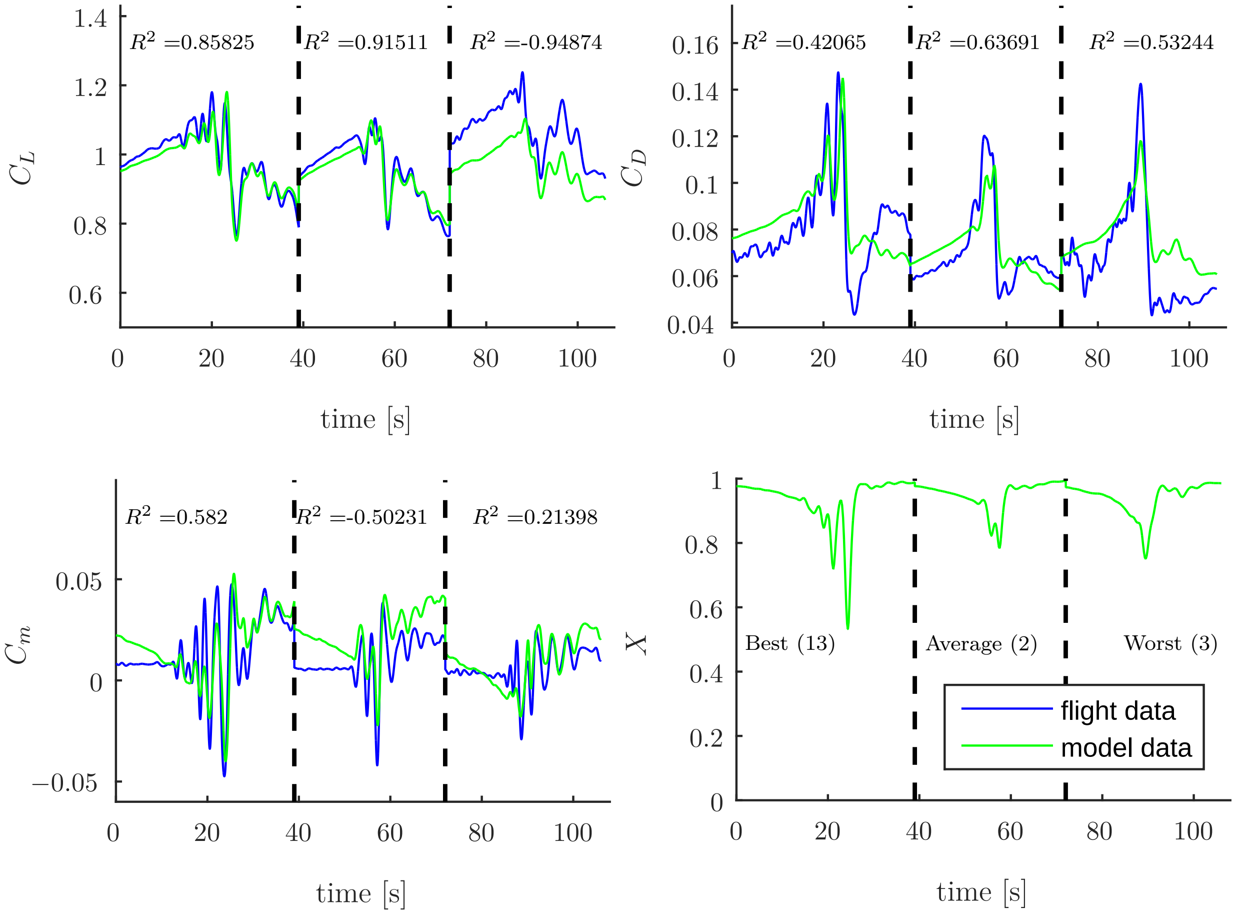

Figure 25. Validation set on the dimensionless forces and moment. The numbers on the bottom right (i.e. 13, 2 and 3), indicate the validation set as shown in Figure 2)

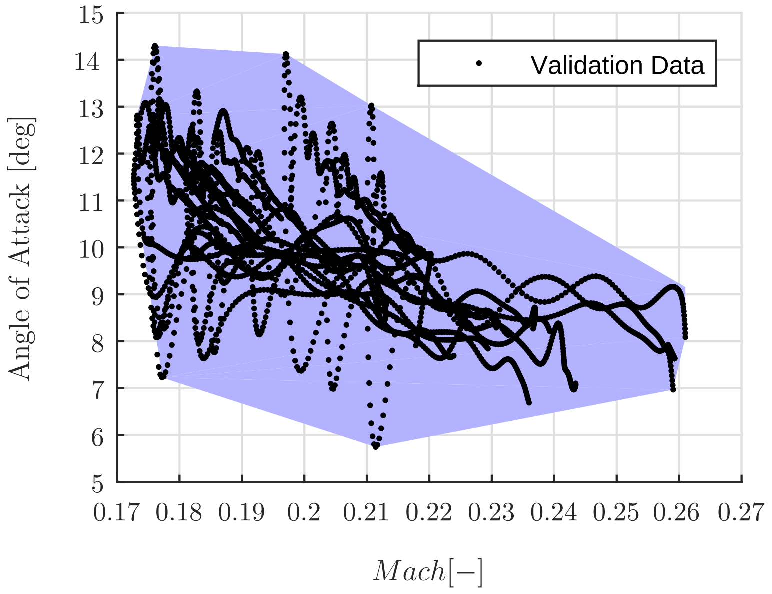

Figure 26. An overview of the validation data in the Mach vs. AoA plane

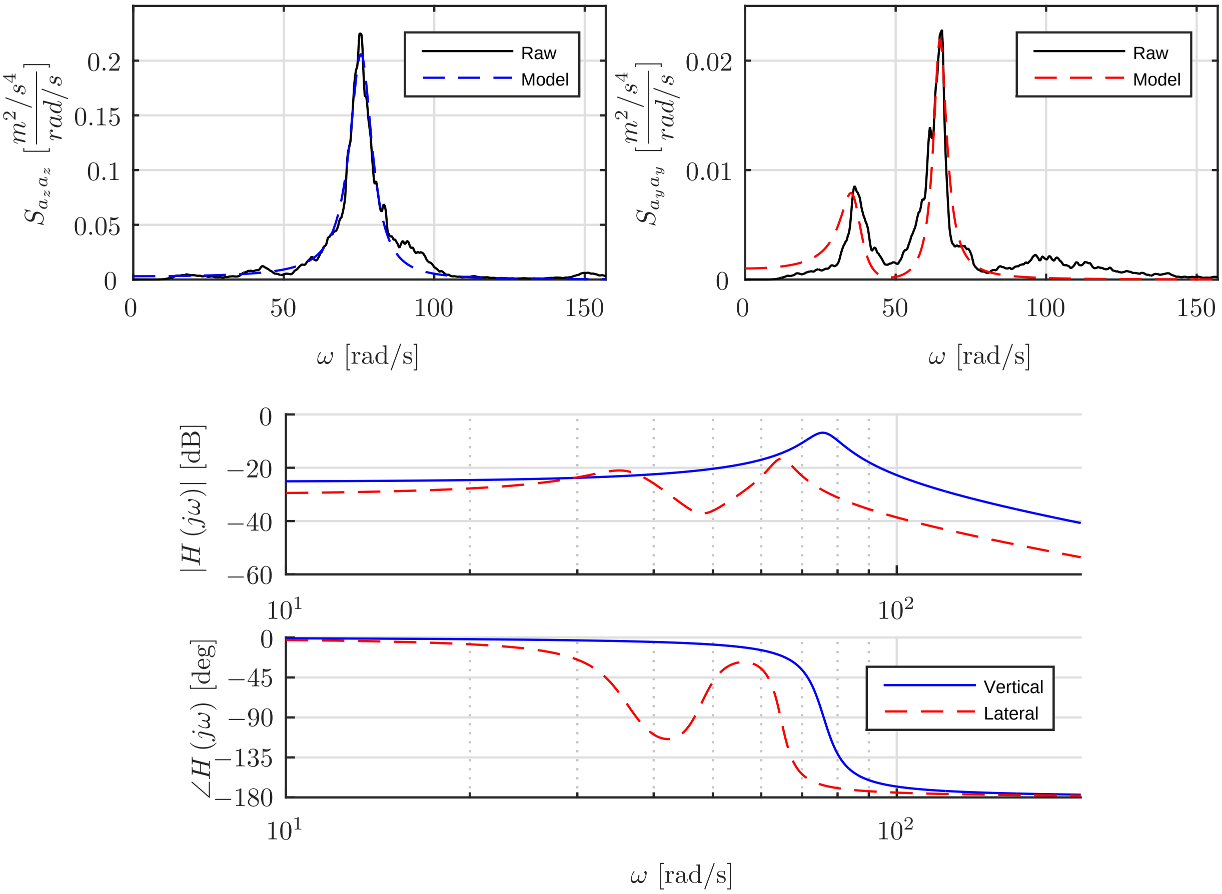

Figure 27. Stall buffet model

Next to the frequency data it is interesting to look at a time history plot for the stall buffet. In Figures 28 and 29, two validation sets for the stall buffet are shown. Both figures show that the stall buffet without transient effect stops prematurely w.r.t. flight data. When the transient effect is included a prolonged buffet can be seen, which matches the flight data better. Therefore it is suggested to use the flow separation point as threshold level, instead of the angle of attack, Because the latter variable does not have such a transient effect. Using the flow separation point thus allows for a more accurate representation of the stall buffet cue. It can however also be noticed that in Figure 29 the stall buffet model acts too late w.r.t. the measured stall buffet from flight data. Indicating that also this method of calculating the stall buffet is still not perfect.

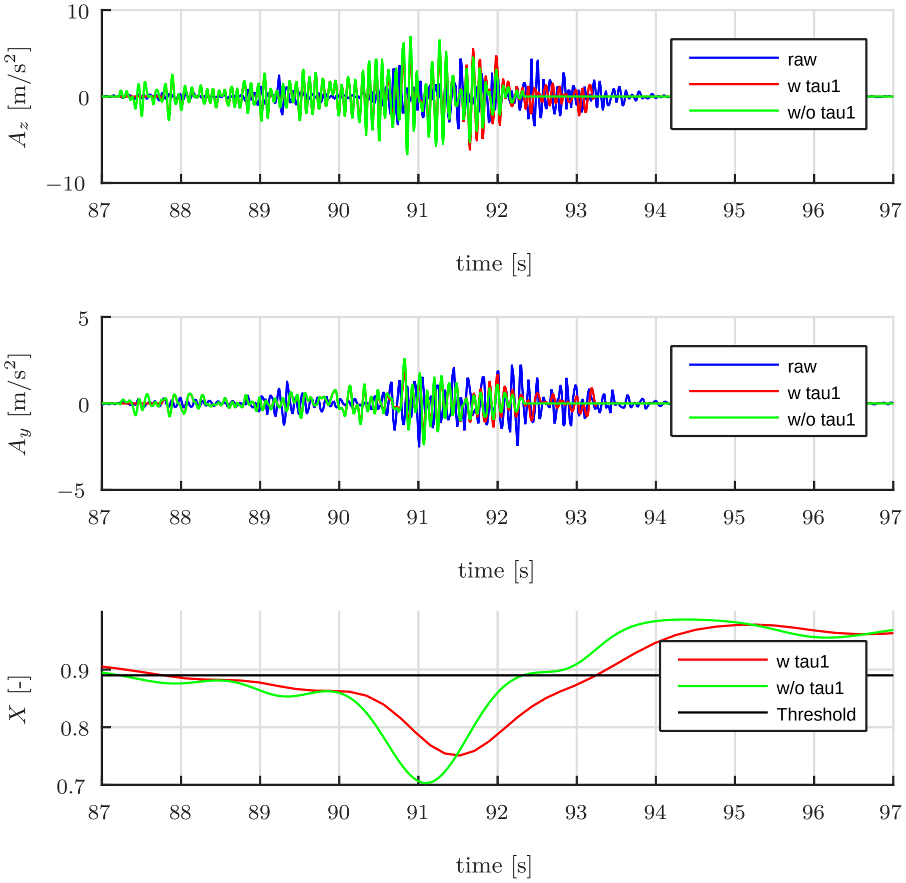

Figure 28. Stall buffet model validation for validation set 3 (as in Figure 2)

The value of τ_1 for this particular aircraft was estimated to be **0.6253**. Looking at Table 4 this value matches close to values found in literature. The threshold value for the onset flow separation point was estimated to be **0.89**. If the flow separation value gets below this particular level then the buffet cue will be turned on.

VI. Discussion

In this paper an overview is given of which characteristics can be modeled using quasi-steady stall maneuvers. Previous researches showed promising results, modeling stalls using an approximation of Kirchoff's flow separation theory.[15,28,29] Such researches, however, mostly use special types of identification maneuvers, such as doublets.

Research institutes and companies, however, might have quasi-steady stall data available, whereas for dynamic data extra flight tests have to be scheduled. This research identifies which stall characteristics can be modeled using quasi-steady maneuvers. This might reduce the cost of stall modeling, in case the most important stall characteristics can be replicated.

Due to the lacking measurement of a side slip measurement, a pseudo-beta was introduced. This increased the quality of the FPR, but only for longitudinal maneuvers. This lack of side slip, however, also means

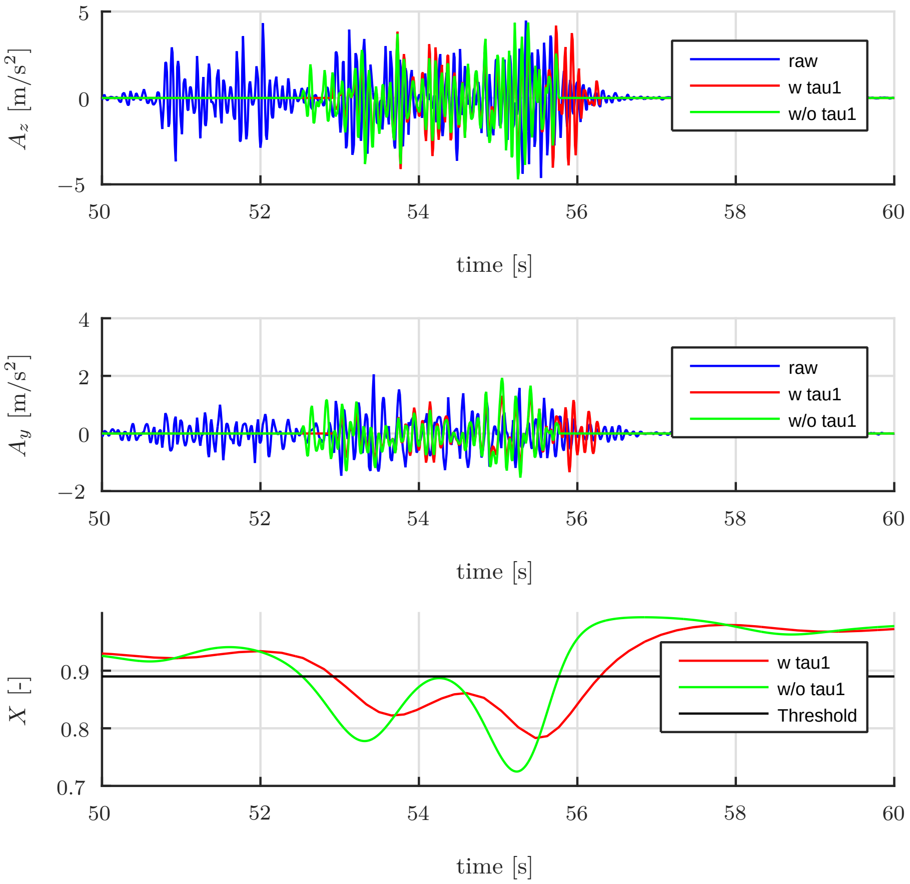

Figure 29. Stall buffet model validation for validation set 2 (as in Figure 2)

that only the longitudinal forces and moments could be predicted. Although a lateral component could be modeled by calculating the lift and drag of both wings separately, characteristics such as the reduced aileron and rudder control effectiveness could not be predicted. To predict the lateral forces and moments, a baseline model is used.[35] From this baseline model the roll damping C_{l_p} could be removed, since by calculating the forces for both wings separately this effect is already included. The effect of reduced aileron and rudder effectiveness could be modeled by reducing the forces and moment generated by the aileron and rudder respectively. The reduction of the elevator effectiveness, on the other hand, could be estimated. On average a value of -0.4 was found for $C_{m_{\delta_e}}$, whereas the baseline model has a value of approximately -1.3.[35]

During this research a large negative correlation between the intercept (C_{L_0}, C_{D_0}, C_{m_0}) and the slope (C_{L_α}, C_{D_α}, C_{m_α}) was found. This is caused by the fact that all values of the angle of attack are far from zero and only limited variation in alpha is experienced around the stall angle. This problem could be solved by: 1) Applying a dynamic maneuver at a lower angle of attack, where C_{L_α} is constant and 2) a dynamic maneuver around the critical angle of attack. The first maneuver will give some extra data closer to zero angle of attack, whereas the second maneuver gives more variation in angle of attack around the stall point. The dynamic stalls that were performed for this research did not show better fitting on the identification data, compared to the quasi-steady symmetrical induced stalls.

The proposed method of estimating the value of τ_1 from the stall buffet data is promising. It was found, however, that due to the randomness of the input signal of the stall buffet, the estimated value of τ_1 varied a little bit depending on the random seed. To make the estimation of τ_1 independent of this random seed multiple runs were done. The found values of all these runs were then averaged to obtain a single value for τ_1. It would be interesting to see how this proposed method compares to estimating τ_1 from highly dynamic stall maneuvers.

Another interesting research field would be to look at a global aerodynamic model, for example using multivariate splines.[24] To identify stability derivatives related to the rotational rates, however, dynamic stall maneuvers must be conducted that are designed specifically for aerodynamic model identification. Such dynamic stall maneuvers are also more likely to improve the fidelity of the moment coefficient. During this research four dynamic stalls were captured, each in a different configuration. This, however, was not enough to properly validate such dynamic stall maneuvers. Single maneuver evaluation is also unusable,[14] therefore during this research the stalls were concatenated in groups of three, which was found to be a good number for parameter estimation. Another interesting study would be to investigate the effect of flaps and landing gear on stall characteristics such as the stall buffet or hysteresis effect.

Lastly, apart from stall model identification, it would be interesting to fly the current identified model in a full motion simulator. This could be done to obtain a subject matter rating on the stall model, based on quasi-steady stalls. Especially since the moment coefficient could not be estimated accurately, therefore the pitch angle does not match closely to the measured pitch angle in flight. On top of that it could be investigated which stall characteristics are the most important for stall recovery training.

VII. Conclusion

In this work an aerodynamic stall model is created based on flight data. It was found that the UKF was suitable for flight path reconstruction techniques. Furthermore it was found that for longitudinal maneuvers it is better to use a pseudo-beta, i.e., a side slip angle modeled as a zero-mean white noise signal, than no side slip observation. It was also found that the vertical wind component (W_{z_E}) was not observable and that the fuselage upwash component on the angle of attack ($C_{\alpha_{up}}$) and unknown wind component in the angle of attack measurement (C_{α_0}) were highly correlated. Therefore without an excitation, such as a stall, no clear distinction could be made between these two variables. Hence C_{α_0} was left out of the state as well.

Furthermore it was found that the hysteresis effect is identifiable using quasi-steady stall maneuvers. The aerodynamic parameters related to the pitch rate, however, showed large variances, indicating that these parameters were not identifiable, except for C_{L_q}. In fact C_{D_q} was found to be both positive and negative and C_{m_q} was estimated to be positive, whereas one would expect a negative value.

The validation sets showed that the identification of the lift coefficient showed the best results, followed by the drag coefficient. The parameters regarding the moment coefficient were difficult to estimate in general, using quasi-steady stall maneuvers. The simulated pitch angle did not match closely to the pitch angle in flight, given the same initial conditions and inputs. The dynamic stalls that were performed for this research did not show better fitting on the identification data, compared to the quasi-steady symmetrical induced stalls.

Although the transient effect could not be identified directly with the other parameters, a method was found to estimate τ_1 from the stall buffet. Using these accelerations a stall buffet model could be created, based on frequency domain analysis. It was found that the altitude does not have a significant effect on the magnitude or frequency of this buffet. The largest buffet accelerations were found to be in z-direction, the second largest in y-direction. The buffet in x-direction on the other hand is negligible. The flow separation point was used as main driver for the stall buffet, both as threshold and as scaling factor. This resulted in a more accurate representation of the stall buffet than using the angle of attack.

In conclusion characteristics such as: the degradation in pitch response, changes in pitch stability, stall buffet and stall hysteresis are identifiable using quasi-steady stall maneuvers, without a side slip measurement. Other effects such as a degradation in lateral-directional stability or the degradation in roll- and yaw response were not identifiable. An uncommanded roll response or roll-off could be modeled by calculating the lift generated by both wings separately.

References

[1] NTSB, "Annual Review 2013 – Data and Statistics," `http://www.ntsb.gov/investigations/data/Pages/AviationDataStats.aspx`, 2013.

[2] FAA, "FAA 14 CFR PART 121: Qualification, Service, and Use of Crewmembers and Aircraft Dispatchers; Final Rule," 2013.

[3] J. V. Foster and K. Cunningham and C. M. Fremaux and G. H. Shah and E. C. Stewart and R. A. Rivers and J. E. Wilborn and W. Gato, "Dynamics Modeling and Simulation of Large Transport Airplanes in Upset Conditions," *AIAA Guidance, Navigation, and Control Conference and Exhibit*, No. AIAA-2005-5933, American Institute of Aeronautics and Astronautics (AIAA), San Francisco, CA, USA, Aug 2005.

[4] M. J. O'Rourke and J. N. Ralston and J. W. Bell and S. F. Lash, "PC-Based Simulation of the F-16/MATV," *Modeling and Simulation Technologies Conference*, American Institute of Aeronautics and Astronautics (AIAA), New Orleans, LA, USA, Aug 1997, pp. 481–489.

[5] J. Kay and J. N. Ralston and S. F. Lash, "Development of Non-Linear, Low-Speed Aerodynamic Model for the F-16/VISTA," *22nd Atmospheric Flight Mechanics Conference*, American Institute of Aeronautics and Astronautics (AIAA), New Orleans, LA, USA, Aug 1997, pp. 822 – 830.

[6] C. J. O'Connor and J. N. Ralston and T. Fitzgerald, "Evaluation of the NAWC/AD F/A-18 C/D simulation including database coverage and dynamic data implementation techniques," *21st Atmospheric Flight Mechanics Conference*, American Institute of Aeronautics and Astronautics (AIAA), San Diego, CA, USA, Jul 1996, pp. 735 – 745.

[7] G. N. Malcolm, "Rotary-Balance Experiments on a Modern Fighter Aircraft Configuration at High Reynolds Numbers," *12th Atmospheric Flight Mechanics Conference*, American Institute of Aeronautics and Astronautics (AIAA), Snowmass, CO, USA, Aug 1985, pp. 462 – 482.

[8] N. B. Abramov and M. G. Goman and A. N. Khrabrov and E. N. Kolesnikov and L. Fucke and B. Soemarwoto and H. Smaili, "Pushing Ahead - SUPRA Airplane Model for Upset Recovery," *AIAA Modeling and Simulation Technologies Conference*, American Institute of Aeronautics and Astronautics (AIAA), Minneapolis, MN, USA, Aug 2012.

[9] Y. Nie and E. van Kampen and Q. P. Chu and T. Kier and G. Looye, "Geometry Based Quick Aircraft Modeling Method for Upset Recovery Applications," *Proceedings of the AIAA Modeling and Simulation Technologies Conference*, American Institute of Aeronautics and Astronautics (AIAA), Kissimmee, FL, USA, Jan 2015.

[10] T. T. Teng and T. S. Zhang and S. Liu and P. R. Grant, "Representative Post-Stall Modeling of T-tail Regional Jet and Turboprop Aircraft for Flight Training Simulator," *AIAA Modeling and Simulation Technologies Conference*, American Institute of Aeronautics and Astronautics (AIAA), Kissimmee, FL, USA, Jan 2015.

[11] D. R. Gingras and J. N. Ralston and R. Oltman and C. Wilkening and R. Watts and P. Desrochers, "Flight Simulator Augmentation for Stall and Upset Training," *AIAA Modeling and Simulation Technologies Conference*, American Institute of Aeronautics and Astronautics (AIAA), Jan 2014.

[12] J. A. Schroeder and J. Bürki-Cohen and D. A. Shikany and D. R. Gingras and P. Desrochers, "An Evaluation of Several Stall Models for Commercial Transport Training," *AIAA Modeling and Simulation Technologies Conference*, No. AIAA-2014-1002, American Institute of Aeronautics and Astronautics (AIAA), National Harbor, MD, USA, Jan 2014.

[13] E. A. Morelli and K. Cunningham and M. A. Hill, "Global Aerodynamic Modeling for Stall/Upset Recovery Training Using Efficient Piloted Flight Test Techniques," *AIAA Modeling and Simulation Technologies (MST) Conference*, American Institute of Aeronautics and Astronautics (AIAA), Boston, MA, USA, Aug 2013.

[14] S. Weiss and H. Friehmelt and E. Plaetschke and D. Rohlf, "X-31A System Identification Using Single-Surface Excitation at High Angles of Attack," *Journal of Aircraft*, Vol. 33, No. 3, May 1996, pp. 485–490.

[15] J. N. Dias, "Unsteady and Post-Stall Model Identification Using Dynamic Stall Maneuvers," *AIAA Atmospheric Flight Mechanics Conference*, American Institute of Aeronautics and Astronautics (AIAA), Dallas, TX, USA, Jun 2015.

[16] Cessna Aircraft Company, Wichita, Kansas, USA, *Operating Manual Mdoel 550 Citation II, Unit -0627 And On*, 1990.

[17] B. O. S. Teixeira and L. A. B. Tôrres and P. Iscold and L. A. Aguirre, "Flight path reconstruction –A comparison of nonlinear Kalman filter and smoother algorithms," *Aerospace Science and Technology*, Vol. 15, No. 1, Jan 2011, pp. 60–71.

[18] E. A. Wan and R. van der Merwe, "The Unscented Kalman Filter for Nonlinear Estimation," *Proceedings of the IEEE 2000 Adaptive Systems for Signal Processing, Communications, and Control Symposium (Cat. No.00EX373)*, Institute of Electrical & Electronics Engineers (IEEE), Alta, UT, USA, Oct 2000, pp. 153 – 158.

[19] S. Feng and R. Murray-Smith, "Fusing Kinect Sensor and Inertial Sensors with Multi-rate Kalman Filter," *IET Conference on Data Fusion & Target Tracking 2014: Algorithms and Applications*, Institution of Engineering and Technology (IET), Apr 2014, pp. 1 – 8.

[20] M. Laban, *On-Line Aircraft Aerodynamic Model Identification*, PhD thesis, Delft University of Technology, Faculty of Aerospace Engineering, Delft, The Netherlands, May 1994.

[21] A. V. Oppenheim and R. W. Schafer, and J. R. Buck, *Discrete-time Signal Processing (2Nd Ed.)*, Prentice-Hall, Inc., Upper Saddle River, NJ, USA, 1999.

[22] R. J. M. Bennis, *Non-linear State Estimation Techniques with Application to Dynamic Modelling of Angle of Attack Vane from Cessna Citation II Flight Data*, MSc thesis, Delft University of Technology, Faculty of Aerospace Engineering, Delft, The Netherlands, Aug 1998.

[23] P. M. T. Zaal and D. M. Pool and M. M. van Paassen and M. Mulder, "Comparing Multimodal Pilot Pitch Control Behavior Between Simulated and Real Flight," *Journal of Guidance, Control, and Dynamics*, Vol. 35, No. 5, Sep 2012, pp. 1456–1471.

[24] C. C. de Visser, *Global Nonlinear Model Identification with Multivariate Splines*, PhD thesis, Delft University of Technology, Faculty of Aerospace Engineering, Delft, The Netherlands, Jun 2011.

[25] B. L. Walcott and M. J. Corless and S. H. Żak, "Comparative study of non-linear state-observation techniques," *International Journal of Control*, Vol. 45, No. 6, Jun 1987, pp. 2109–2132.

[26] J. A. Mulder and J. K. Sridhar and J. H. Breeman, “AGARD Flight Test Techniques Series. Volume 3. Identification of Dynamic Systems-Applications to Aircraft. Part 2. Nonlinear Analysis and Manoeuvre Design.),” Tech. Rep. 2, DTIC Document, 7 Rue Ancelle, 92200 Neuilly-sur-Seine, France, 1994.

[27] V. Klein and E. A. Morelli, *Aircraft System Identification: Theory and Practice*, American Institute of Aeronautics and Astronautics (AIAA), Jan 2006.

[28] D. Fischenberg, “Identification of an unsteady aerodynamic stall model from flight test data,” *20th Atmospheric Flight Mechanics Conference*, American Institute of Aeronautics and Astronautics (AIAA), Baltimore, MD, USA, Aug 1995, pp. 138 – 146.

[29] D. Fischenberg and R. V. Jategaonkar, “Identification of Aircraft Stall Behavior from Flight Test Data,” *Proceedings of the RTO SCI Symposium on System Identification for Integrated Aircraft Development and Flight Testing*, No. RTO MP-11 in , German Aerospace Center (DLR), Braunschweig, Germany, Mar 1999, pp. 17–1 – 17–8.

[30] J. A. Mulder and W. H. J. J. van Staveren and J. C. van der Vaart and E. de Weerdt and C. C. de Visser and A. C. in ’t Veld and E. Mooij, *Lecture Notes AE3202: Flight Dynamics*, Delft University of Technology, Delft, The Netherlands, Mar 2013.

[31] J.J. Moré and D.C. Sorensen, “Computing a Trust Region Step,” *SIAM Journal on Scientific and Statistical Computing*, Vol. 4, No. 3, Sep 1983, pp. 553–572.

[32] T. F. Coleman and Y. Li, “An Interior Trust Region Approach for Nonlinear Minimization Subject to Bounds,” *SIAM J. Optim.*, Vol. 6, No. 2, May 1996, pp. 418–445.

[33] J. N. Dias, “High Angle of Attack Model Identification with Compressibility Effects,” *AIAA Atmospheric Flight Mechanics Conference*, American Institute of Aeronautics and Astronautics (AIAA), Kissimmee, FL, USA, Jan 2015.

[34] M. Goman and A. Khrabrov, “State-Space Representation of Aerodynamic Characteristics of an Aircraft at High Angles of Attack,” *Journal of Aircraft*, Vol. 31, No. 5, sep 1994, pp. 1109–1115.

[35] M. A. van den Hoek and D. M. Pool and C. C. de Visser and M. Mulder, “Identification and Implementation of a High-Fidelity Cessna Citation II Simulation model based on Flight Test Data,” Delft University of Technology, Aug 2016.

Part II

Preliminary Thesis

Chapter 1

Introduction

1-1 Background/ Motivation

The largest cause of fatalities in general aviation and an important contributor to accidents in airliners is loss of control in flight (NTSB, 2013). A major contributor to this loss of control are aerodynamic stalls. An aerodynamic stall is a highly dynamic and non-stationary condition where the flow over the wings of the aircraft detaches in unpredictable ways. This can lead to dangerous upset conditions if left uncorrected.

To solve this, the FAA stated that all pilots flying for air-carriers in the United States are obliged to receive training in stall recovery in 2019 (FAA, 2013). Current stall training is often done in smaller (single engine) aircraft, however, the dynamics of such an aircraft differ from large airliners. Due to the risk and cost involved in stall training with these larger aircraft, it is most likely that pilots will receive upset recovery training in FTSD.

Current development of stall models is mostly based on flight test, wind tunnel and CFD data. Flight tests are both expensive and definitely not without danger. Furthermore by using only flight test data it is nearly impossible to model fully developed stalls, such as a (flat) spin. Therefore state-of-the-art flight models are often combined with wind tunnel and/ or CFD analysis to predict the aerodynamics in fully developed stalls.

The major disadvantage of current stall model developments is the huge cost that is involved. Although large aircraft manufactures have the means to use these expensive methods to create stall models, this situation does not apply for smaller GA aircraft manufacturers. Furthermore it is difficult to obtain fully developed stall data for all commercial aircraft (Schroeder et al., 2014).

For this reason, the division on C&S at DUT has set up a 'task force' to develop a new methodology for creating stall models at much lower cost. The first step in this project will consist of the development of a stall model for the Cessna Citation II laboratory aircraft, based on existing flight test data collected over more than a decade of flight tests. This newly identified stall model will be combined with a new high-fidelity dynamics model of the aircraft. This will result in a fully integrated model that can be used to simulate stall onset and initial stall development in SRS at DUT.

1-2 Delft University Aircraft Simulation Model and Analysis Tool

Throughout this literature study extensive use is made of the Delft University Aircraft Simulation Model and Analysis tool (DASMAT), which is a nonlinear aircraft model of the Cessna Citation I. This flight model is available in the MATLAB/ Simulink environment. DASMAT includes a set of tools including: an aerodynamic and engine model, trim function, linearization function and an aircraft animation tool (Linden, 1996). What DASMAT is lacking, is an accurate representation of the stall dynamics. A part of this thesis is to develop such a stall model. The baseline model of DASMAT will also be changed to match the Cessna Citation II more closely. The development of this baseline model, however, is part of another thesis project. Lastly for this thesis an extra sensor model is included, to match the increase the fidelity of the state estimation.

1-3 Project Objective for Cessna Citation II Stall Model

For the current project a specific model will be created, i.e. a model based on real life flight data. The reason for doing this is twofold. First there is no current stall model available for the Cessna Citation II. That means that there is no baseline model which can be used for comparison, which increases the difficulty of the validation of more sophisticated stall models, such as those based on CFD analysis and/ or geometrical properties. Secondly a lot of flight data is already available. This means that the costs already have been made and that a lot of time can be saved in comparison with, e.g. obtaining aerodynamic data from wind tunnel testing. This flight data is something unique at Delft University of Technology, since it owns an aircraft together with the Nederlands Lucht- en Ruimtevaartcentrum (NLR).

The outcome of this thesis project, is thus a stall model based on real life flight data. This stall model can then in the future be used to validate the work of later projects on stall modeling, e.g. when a stall model based on geometrical properties will be made. Furthermore this stall model can be used for other projects, for which a stall model is needed. Such a research project could for example be on stall for pilots in stall recovery.

In this research only quasi-steady stalls are used. These are used to identify different stall characteristics. The research question is as follows: **Which stall characteristics are identifiable using quasi-steady stalls**. To answer this question, state estimation techniques have to be applied first, to obtain more accurate results for regressor variables such as the angle of attack. The second step is the estimation of the parameters. The sub-questions can be composed as follows:

1. Which state estimation technique gives the most accurate results.
2. What are typical stall characteristics?
3. How can the stall characteristics be modeled mathematically?
4. What parameter estimation techniques are suitable stall model identification?

1-4 Project Outline

This project will have five major steps that will be taken. The first step is to identify so called stall properties. These properties, such as a degradation in static/dynamic lateral-directional stability (Ralston, Gingras, Wilkening, & Descrochers, 2012) will be summarized. These properties can then be used as a set of requirements for stall modeling. In Chapter 2 several requirements as proposed by the FAA regarding stall modeling are given. Lastly a mathematical approach to model stall dynamics will be given in Chapter 2, to be used for the real-time simulation of an aerodynamic stall model.

The second step involves Flight Path Reconstruction (FPR). This is the part where the state of the aircraft will be determined, such that it can be used for stall modeling. With FPR the state of the aircraft can be reconstructed, consisting of the body velocities and Euler angles. This state reconstruction allows the determination of Inertial Measurement Unit (IMU) biases and body induced velocities on the air flow measurements.

In Chapter 3 several Kalman filters and smoothers will be discussed, which is one of several methods for flight path reconstruction. The main reason to choose for the Kalman filter is the expertise within C&S on not only Kalman filters but also the two-step method (Mulder, Chu, Sridhar, Breeman, & Laban, 1999). At the end of Chapter 3 a comparison is given between different kinds of Kalman filters and smoothers, for simulated flight data.

The third step in this project is the parameter estimation of the stall model itself. Although the equations are already given in Chapter 2, some nonlinear optimization techniques will be given in Chapter 4. These three nonlinear optimization algorithms are: Gauss-Newton, Levenberg-Marquardt and Nelder-Mead. The main reason to use nonlinear optimization techniques is because the equations that will be used for stall modeling are nonlinear, which seems logical since stalls show nonlinear behavior. Therefore it is not possible to use linear regression techniques such as ordinary least squares.

The fourth step is to combine the stall model with the updated Cessna Citation II framework. Since these will be two separate projects it is important to investigate the blending two aerodynamic models: one for normal flight conditions and one for the stall model to predict behavior outside of the flight envelope. When using aerodynamic derivatives, such as C_{L_α} it is possible to blend the model in two separate ways (Ralston et al., 2012). The first one is replacing part of the baseline flight model by the stall model. The second option is to calculate the difference between the baseline model and the stall model and add an incremental addition to the baseline model in the stall regime. To prevent any strange behavior due to discontinuities in the aerodynamic flight model it is important to also have a smooth transition between the two models.

The last step is to verify and validate the stall model. The FAA published a federal register with information about extended envelope training tasks with FTSD (FAA, 2014). In this register it is stated that for stall training tasks the model has to be validated through at least 10 degrees beyond the critical angle of attack. Since the aerodynamics within the stall region are unstable there are no strict tolerances for aircraft behavior. To compensate for this a Statement of Compliance (SOC) is required. To obtain this SOC the stall model has to be tested by a Subject Matter Expert (SME), with knowledge and experience in the types of stall in the type of aircraft. Furthermore the FAA describes aircraft upsets to be an airplane unintentionally exceeding: a pitch attitude greater than 25 degrees nose up, a pitch attitude greater than 10 degrees nose down, bank angles greater than 45 degrees or being within the mentioned parameters, but flying at an airspeed inappropriate for the given conditions (FAA, 2014).

Chapter 2

Stall Modelling

In this chapter first a precise definition of a stall is given, after which the effects are summarized which influence the stall. Then different methods of indicating stalls with respect to the flight envelope are given. Thirdly the stall model features as proposed by the International Committee for Aviation Training in Extended Envelopes (ICATEE) will be described. Then some different methods for stall modeling, as proposed by industry and research institutes is given in section 2-2. Lastly the most promising method for real-time stall modeling, i.e. using Kirchoff's flow separation theory, is introduced and discussed.

2-1 Stall Dynamics

A stall happens when the airflow starts separating from the main wings. This is caused when the angle of attack of wings exceed the critical angle of attack on an airfoil. When the flow separates from the wing the lift created by the wings is reduced. An important note is that when the wing stalls the lift does not drop to zero, which is a common misconception. The critical angle of attack of a wing and the corresponding maximum lift coefficient however is influenced by several factors. As shown in Figure 2-1 the maximum lift coefficient increases with an positive of angle of attack rate.

This effect was shown by a study performed by the National Advisory Committee for Aeronautics (NACA) (Gadeberg, 1951). Where it was concluded that the maximum lift coefficient is approximately linear with respect to the angle of attack rate for value of $\frac{\bar{c}}{V}\dot{\alpha}$ up to 0.66 degrees.

Another factor influencing the critical angle of attack is the use of flaps. Although flaps increase the maximum lift coefficient they also tend to decrease the critical angle of attack of the overall aircraft. This is caused by a change of the chord of the wings, which increases the angle of attack locally. This effect can be seen in Figure 2-2. As shown the camber of the wing changes when the flaps are deployed. Due to this increased camber the chord line changes which causes the local angle of attack to change. The critical angle of attack does not change locally, i.e. at the wing. The overall critical angle of attack however, i.e. compared to the

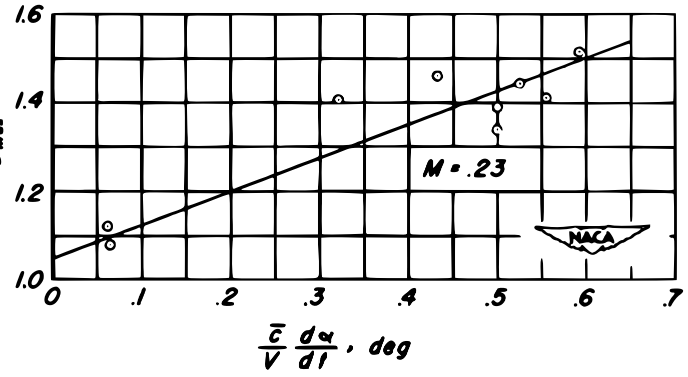

Figure 2-1: Relation between the maximum lift coefficient and the angle of attack rate (Gadeberg, 1951)

whole aircraft is now lower than the critical angle of attack at the wing. The overall critical angle of attack is thus reduced. The opposite effect happens when the aircraft is equipped with leading edge flaps or slats. These "rotate" the chord line downward and thus reduce the local angle of attack at the wing.

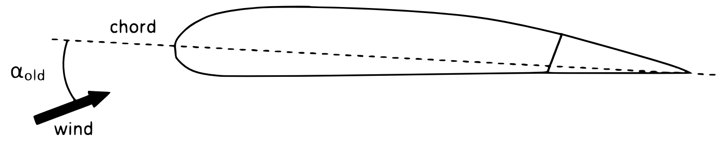

(a) Airfoil without flaps extended

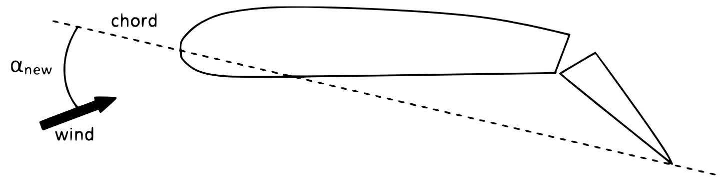

(b) Airfoil with flaps extended

Figure 2-2: Difference in angle of attack between an wing with flaps extended and flaps retracted

A less predictable effect on the critical angle of attack is wing contamination. These effects can be caused by phenomena such as ice on the wing, but also dirt and dents can contaminate the wings. This effect however is hard to measure and thus will be neglected for modelling stall behavior.

Lastly the Mach number and Reynolds number influence the critical angle of attack as well as shown in (Furlong & Fitzpatrick, 1947). It was shown that the largest critical angle of attack was reached at a Mach number of approximately 0.25 to 0.30, for a NACA 230-series airfoil with flaps retracted. Beyond this Mach number the critical angle of attack decreases. Furthermore it was shown that an increase in Reynolds number increased the the critical angle of attack.

2-1-1 Flight Envelope

When an aircraft stalls it is also said that the aircraft goes outside its flight envelope. This flight envelope can be described in several ways. In this subsection three different methods of flight envelope presentations will be discussed, i.e.: airspeed vs. load factor, airspeed vs. altitude and angle of attack vs. angle of side slip

Although in the last subsection it was discussed that a stall is merely depended on the angle of attack it must not be forgotten that an aircraft is still able to maintain level flight if the maximum producible lift can equal its weight. This lift is not only a function the angle of attack, but also on the airspeed and density. The latter one is again a function of altitude and therefore airspeed and altitude are also often used to describe the flight envelope.

Airspeed vs. Load Factor

Probably one of the most well known ways to describe the flight envelope of the aircraft is by the so called V-n diagram. An example of such a diagram is given in Figure 2-3. From the V-n diagram it is possible to obtain the maximum allowed load factor and maximum speed. These can be found on the right side of the V-n diagram. On the left side of the V-n diagram however the so called "stall line" is shown. When the aircraft's state enters the left side of this slope the aircraft will stall. This line can be easily be produced from the standard aircraft dynamics and lift equation and is given by Eq. 2-3.

$$V_{stall} = \sqrt{\frac{2nmg}{\rho S C_{L_{max}}}} \tag{2-1}$$

From the V-n diagram it can be easily seen that the stall speed increases when the load factor increases. The reason for this is that the lift that needs to be generated is the weight of the aircraft times the load factor. Furthermore from Eq. 2-3 it can be seen that this stall line is a function of the mass and density as well, whereas the density can be written as function of the altitude. So the V-n diagram only describes the situation for one condition of mass and altitude.

Airspeed vs. Altitude

To see the effect of altitude on the stall speed more clearly a so called airspeed vs. altitude diagram can be made, as shown in Figure 2-4. In this figure only the stall line is shown, and not the altitude ceiling and maximum velocity. To construct this stall line Eq. 2-1 can be used. Now however with the load factor equal to one and a varying density. This density can be calculated from the International Standard Atmosphere (ISA). As can be seen in Figure 2-4, the stall speed increases with altitude due to a decrease in the density. Furthermore the stall speed increases with increasing mass of the aircraft as well. Note that in the maximum lift coefficient and critical angle of attack were assumed constant. As explained in the previous section however these change with the Mach number and Reynolds number. The speed of sound decreases and the stall speed increases with altitude. Together this implies an increase in the Mach number. The Reynolds can be calculated by:

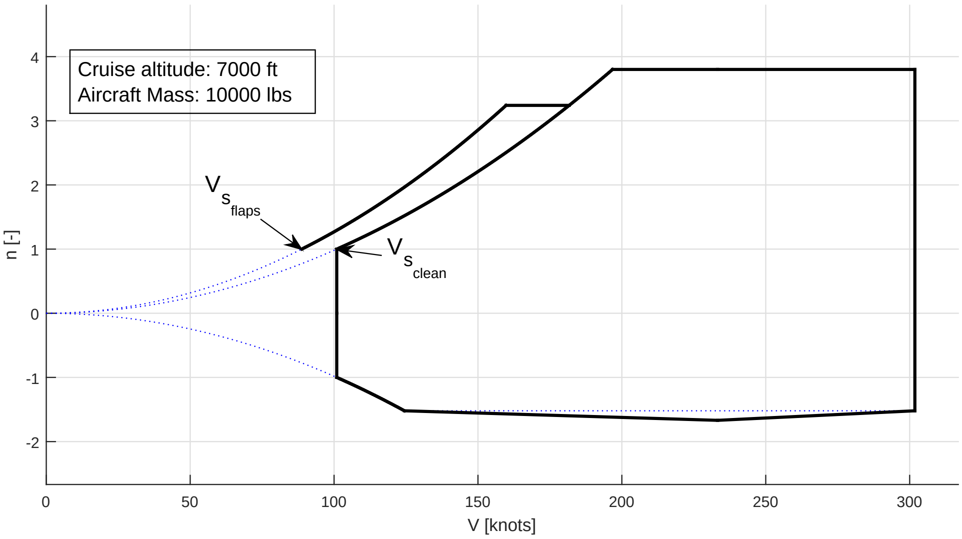

Figure 2-3: Example of a V-n diagram

$$Re = \frac{\rho v L}{\mu}$$

Where ρ is the density, v the velocity over the object, L the length of the object (for a wing the chord) and μ the dynamic viscosity. As can be seen the Reynolds number decreases somewhat due to the decrease in density but increases due to the increase in stall speed. These however do not compensate for each other. Due to a non constant Mach number and Reynolds number the assumption that the critical angle of attack and maximum lift coefficient are constant is not perfectly valid. For simply demonstrating the effect of altitude and mass on the stall speed however this assumption was made.

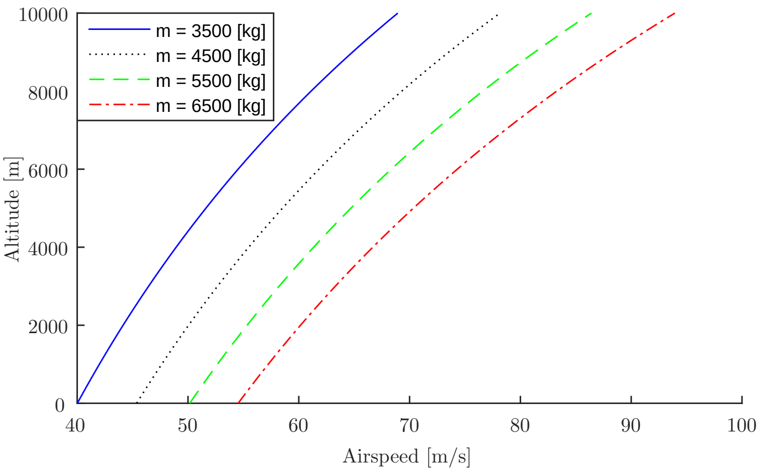

Figure 2-4: Airspeed vs. Altitude diagram

Angle of attack vs. Angle of side slip

A somewhat less intuitive way of describing the flight envelope is by a diagram of the angle of attack vs. the angle of side slip. The reason for stalling as explained before is when the angle of attack exceeds the critical angle of attack. A side slip will decrease the angle of attack on the forward wing for a low wing aircraft such as the Cessna Citation II (Mulder et al., 2013). The angle of attack on the backward wing however will increase. For an aircraft with a high wing configuration this effect is reversed. This effect, caused by the wing-fuselage interaction is shown in Figure 2-5.

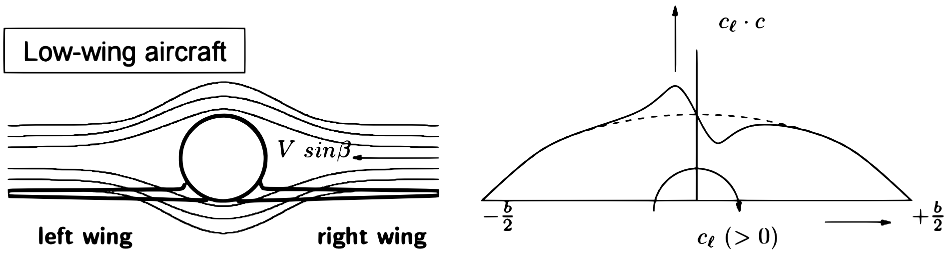

Figure 2-5: Rolling moment caused by wing-fuselage interaction in side slipping flight (Mulder et al., 2013)

Although the wing fuselage interaction does have an effect on the local angle of attack at the wing due to a side slip, a (possibly) larger effect is caused by the wing dihedral (Mulder et al., 2013). Lets assume that the aircraft flies straight and level, but has a side slip from the right as shown in Figure 2-6a. It can be seen that, assuming a small dihedral:

$$V_{n_r} = w \cos\Gamma + v \sin\Gamma \approx w + v\Gamma \tag{2-2}$$

Furthermore from Figure 2-6a it can be derived from simple trigonometry that:

$$v = V \sin\beta \approx V\beta \quad \text{and} \quad w = V \sin\alpha \approx V\alpha \tag{2-3}$$

Substituting Eq. 2-3 into Eq. 2-2 results into:

$$V_{n_r} \approx V\left(\alpha + \beta\Gamma\right) \tag{2-4}$$

The local angle of attack at the right wing is then:

$$\alpha_{w_r} = \arctan\left(\frac{V_{n_r}}{u}\right) \approx \alpha + \beta\Gamma \tag{2-5}$$

Similarly as in Eq. 2-5 the angle of attack on the left wing can be derived, finally resulting in:

$$\alpha_{w_l} \approx \alpha - \beta\Gamma \tag{2-6}$$

Due to the wing-fuselage effect and the wing-dihedral the angle of attack of one of the wings is increased in a side slipping flight. Therefore the critical angle of attack of the whole aircraft is reduced when a side slip is introduced. An example of a flight envelope is given by the green area given in Figure 2-7.

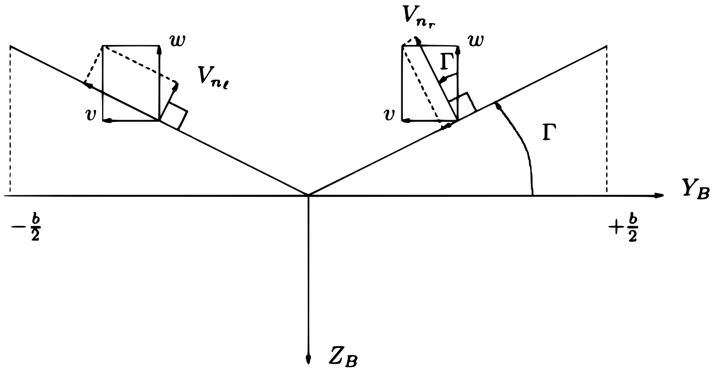

(a) Backview of the induced velocity at both wings

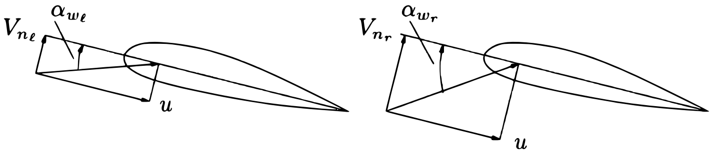

(b) Sideview of the induced velocity at both wings

Figure 2-6: Effect of side slip on an aircraft with wing dihedral (Mulder et al., 2013).

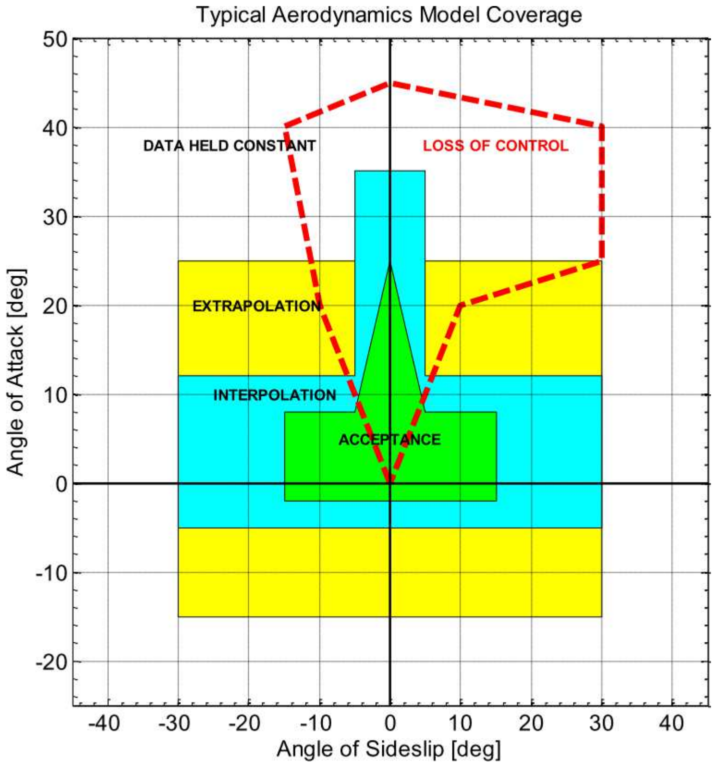

Figure 2-7: Flight envelope in terms of angle of attack and side slip angle (Ralston et al., 2012)

2-1-2 Stall model features

When an aircraft enters a stall the aircraft experiences several features, which are normally not experienced during flight within the normal flight envelope. The following (aerodynamic) features are proposed by the ICATEE as described in (Ralston et al., 2012):

- **Degradation in static/dynamic lateral-directional stability**
  When an aircraft enters a stall the static and dynamic lateral-directional stability degrades. The lateral stability concerns the the rolling stability where the directional stability indicates the stability with respect to the yawing of the aircraft. The most important aerodynamic parameters for the lateral-directional stability will be analyzed in normal flight and stall.

  - **Rolling moment due to a side slip (C_{l_β})**
    The rolling moment due to a side slip, also known as the effective dihedral in normal circumstances is desirably negative (Mulder et al., 2013). If due to a disturbance the aircraft rolls to the right then a positive side slip is introduced, meaning that the aircraft is side slipping to the right. With a negative value of C_{l_β} the aircraft starts to rotate to the left, making it a stable system. During stall however this value will start to get more positive towards zero. The reason for this can be explained as follows. The two major players in determining the effective dihedral are the wings and vertical tail (Mulder et al., 2013). When the aircraft starts side slipping to the right the induced angle of attack on the right wing is greater than on the left wing, as explained in Section 2-1-1. Now when the aircraft flies in the stall regime, the right wing will most likely stall due to the increased angle of attack. Therefore the lift on the right wing is reduced, while on the lift wing it is not and thus the aircraft will roll to the right even more. The vertical tail plane still generates a negative value for the effective dihedral. When the angle of attack however is large enough the vertical tail plane could get in the wake of the turbulent flow of the main wing, the vertical tail plane could thus be rendered useless. The overall value of C_{l_β} thus moves toward zero and could even get positive.
  - **Yawing moment due to a side slip (C_{n_β})**
    The yawing moment due to a side slip is a static directional stability term. It is also known as the weathercock stability. When a side slip is introduced it is desirable that the aircraft automatically reduces the side slip again by creating a moment in the direction of the side slip. Thus a positive side slip should cause a positive moment and therefore it is desirable that the value of C_{n_β} is positive. The largest contributor to the weathercock stability is the vertical tail plane (Mulder et al., 2013). Just as with the effective dihedral the vertical tail plane could get in the turbulent flow from the main wing, rendering the vertical tail plane (almost) useless. The only effect on the weathercock stability then is then from the fuselage, which is destabilizing (Mulder et al., 2013). Thus with only the fuselage contributing to the value of C_{n_β}, it can become negative for high angles of attack.
  - **Rolling moment due to rolling C_{l_p}**
    For normal flight conditions the rolling moment, i.e. the moment around the Y-axis of the aircraft, due to rolling is negative. The dominant term for C_{l_p} are the wings (Mulder et al., 2013). The reason that this term is negative in normal flight conditions is relatively simple. When an aircraft banks to the right, the angle of attack of the down going wing increases. This increases the lift on the down going wing, which in turn results in an opposite rotation. Therefore this term is also

known as the roll damping on an aircraft. At high angles of attack however it is possible that angle of attack of the down going wing exceeds the critical angle of attack. This causes the down going wing to stall and possibly amplify the rotation instead of damping it. Thus at high angles of attack the value of C_{l_p} tends to get positive.

- **Yawing moment due to rolling (C_{n_p})**
  The stability derivative C_{n_p} is the yawing moment due to rolling of the aircraft. The main contributors are the main wing and the vertical tail plane. The contribution of the main wing might be somewhat counter intuitive. When an aircraft is rolling the down going wing has an higher angle of attack then the up going wing. Due to this increased angle of attack on the low wing it looks as if the flow is coming more from below the wing. The lift vector, which is perpendicular to the oncoming flow, is thus rotated forward. Vice versa the lift vector of the up going wing rotates backward. Therefore the up going wing experiences an extra force backward in X_b-direction and the down going wing experiences an extra force forward (Mulder et al., 2013). Due to this force in X_b-direction the aircraft will rotate towards the up going wing. Thus with a positive rolling moment, i.e. the right wing going down, the aircraft will experience a negative yawing moment. The contribution of the wings is thus negative on C_{n_p}. This effect is also known as adverse yaw. During stall the flow separates from the wing, this increases the drag considerably and it can cause the extra force in X_b-direction to become negative. Thus reversing the effect of the wings on C_{n_p} by making the term more positive (Mulder et al., 2013). The effect of the vertical tail plane is positive on C_{n_p}. This can be easily seen, take for example the aircraft rolling to the right. The vertical tail plane will then experience force pointing towards the left, which in turn yaws the aircraft to the right. Positive rolling thus causes a positive yawing moment. The value of C_{n_p} can thus be either positive or negative during normal flight. During stall the contribution of the wing will become more positive. When the vertical tail plane however enters the wake of the main wing its contribution will become negligible. So it is most likely that the value of C_{n_p} becomes positive at high angles of attack.

- **Rolling moment due to yawing (C_{l_r})**
  The rolling moment due to yawing is determined by the contributions of the main wing and vertical tailplane as well (Mulder et al., 2013). In a yawing turn the inside wing experiences a slower local velocity than the outer wing. Therefore the outer wing produces more lift than the inward wing, causing a rolling moment in the direction of the yawing direction. The contribution of the wings on C_{l_r} is thus positive. When the aircraft yaws to the right, the vertical tail plane will experience an angle of attack from the left side, thus creating a force towards the right. Positive yawing thus causes a positive rolling moment, thus the contribution of the vertical tailplane on C_{l_r} is positive as well. In normal flight condition the value of C_{l_r} is thus certainly positive. At high angles of attack, both wings encounter the same angle of attack so the effect due to main wing stays positive. The vertical tail however can get in the wake of the main wing rendering it useless. Therefore the value of C_{l_r} becomes less positive.

- **Yawing moment due to yawing (C_{n_r})**
  Lastly the yawing moment caused by a rotational velocity around the yawing axis

is considered. Just as for C_{l_p}, the value of C_{n_r} is a damping term. The value of C_{n_r} is thus negative. The main contributor to this value is the vertical tailplane. A yawing moment to the right will create a force on the vertical tailplane to the right. This in turn creates a yawing moment to the left, thus the contribution of the vertical tailplane to C_{n_r} is negative. Although the contribution of the tailplane is the largest, the fuselage for modern aircraft can also contribute C_{n_r}. This contribution is negative as well (Mulder et al., 2013). During a stall however when the vertical tailplane enters the wake of the main wing, the contribution of the vertical tailplane goes to zero. Thus the value of C_{n_r} becomes less negative during stall, compared to normal flight operations.

- **Degradation in control response (pitch, roll, yaw)**
  Just as the lateral-directional stability of the aircraft reduces during stall, the control responses reduce as well. Due to turbulent flow around the wing and possibly around the vertical tailplane the aileron, rudder and elevator effectiveness is reduced. Each of those term thus goes towards zero. An interesting effect that could occur near stall regime is control reversal. Take for example an aileron input at high angles of attack. When turning towards the right the aileron on the left wing will deflect downward. This increase the local angle of attack on the left wing. In normal flight conditions this results in the lift created by the left wing to be greater than the lift on the right wing. It could happen though, at large angles of attack, that the left wing stalls due to the downward aileron deflection, while the right wing does not. The aircraft would then start to roll to the left instead of to the right. This effect is known as control reversal.

- **Uncommanded roll response or roll-off, requiring significant control deflection to counter**
  When entering a stall the aircraft will most likely roll. This can happen when one of the wings stalls earlier than the other. The stalling wing produces less lift than the non-stalling wing, creating an asymmetric lift distribution on the aircraft. This in turn creates a rolling motion. Next to an asymmetric lift distribution the drag of the stalled wing is also increased compared to the non stalling wing. This will cause and extra yawing moment in the direction of the stalling wing. Due to the roll-yaw coupling the aircraft will tend to roll even more.

- **Apparent randomness or non-repeatability**
  Because the aerodynamics during stall are highly nonlinear it is hard to predict what exactly happens with the airflow. Therefore it might happen that sometimes the left wing stall first and other times the right wing. Next to that the initial condition of the stall might influence the stall as well. Just before stall, the state trajectory becomes critical, i.e. even small disturbances can be quickly amplified into larger state excursions. Therefore stalls become rather unpredictable and thus is one of the features of a stall is randomness or non-repeatability.

- **Changes in pitch stability**
  The pitch stability of an aircraft changes as well during stall. This could happen due to a swept wing when e.g. the wing tips stall earlier than the root. In such a case, with the center of gravity in front of the aerodynamic center, the pitch stability would be reduced. The Cessna Citation II however does not have swept wings, but the pitch

stability can still change during stall. A change in the center of lift of a wing can also change the pitch stability, when the c.g. is in front of the wing and the center of lift of the wing moves aft, the pitch stability of the aircraft will increase. The center of lift for straight wing configurations however, such as the Cessna Citation II, does not change significantly due to stall (Crider & Foster, 2012). Another factor that influences the pitch stability is the horizontal tail. For a conventional-tail configuration the horizontal tail plane will most likely enter the wake of the main wing during stall. When the horizontal tail is in the wake the pitch stability C_{m_α} is temporarily reduced as shown by point 1 in Figure 2-8. When the angle of attack is increased even further the wake will pass above the horizontal tail as shown by point 2 in Figure 2-8. This causes the horizontal tail plane to operate in a region with smaller downwash angles and higher dynamic pressure, which increases the pitch stability (Loftin, 1985).

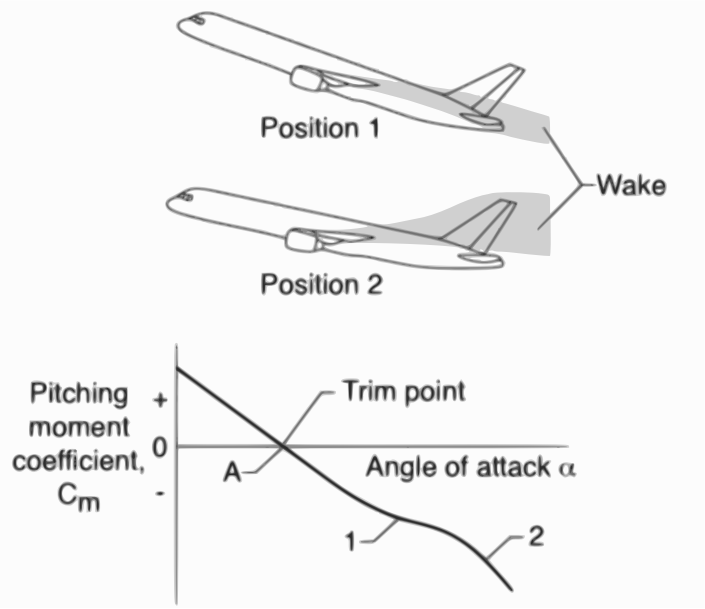

Figure 2-8: Effect of horizontal tail on the static longitudinal stability (Loftin, 1985)

- **Mach effects**
  When an aircraft flies close to a Mach number equal to one it can happen that flow over wing is higher than Mach one. This causes the shock waves on the wing, which can result in a stall as well (Anderson, 2001). This however is not the objective of this research and thus will not be discussed further.

- **Stall buffet**
  When an aircraft is stalling, a (strong) vibration can be felt inside the aircraft. This vibration is caused by the turbulent flow around the wing and is known as (aerodynamic) stall buffet. This stall buffet is one of the important cues for pilots that the aircraft is stalling (Foster et al., 2005).

- **Stall Hysteresis**
  Another very important effect of a stall is the so called stall hysteresis. In short this means that the lift coefficient due to the angle of attack (C_{L_α}) does not follow the same

path forward as backward when the wing has stalled. This is caused by the phenomena that the stall reattaches at lower angles of attack than that it detached in the first place. This effect can be modeled by Kirchoff's flow separation theory as described by (Fischenberg, 1995) where the flow separation point is described as a function of the angle of attack and the angle of attack rate.

2-2 Stall Model types

Now the aerodynamics during and post-stall are better understood, it is time to distinguish the different ways a stall model could be developed. One method of creating a stall model is by using real-life flight data, also called a specific model. Another option would be to use wind tunnel data and CFD analysis, known as representative model. These two model types have already been compared for flight simulation training (Schroeder et al., 2014). A third option would be to create a model based on the aircraft geometry as proposed by (Nie, van Kampen, Chu, Kier, & Looye, 2015). Lastly a pure phenomenological, which only simulates the phenomena during stall.

2-2-1 Specific Model

The specific model is based on flight test data and is currently standard for developing stall models. The benefit of using real flight test data is that this data captures the dynamics of the aircraft as close as possible. Effects such as a difference in Reynolds number are the easiest to obtain with real life flight tests. A disadvantage of using a specific model is that the flight data has to be analyzed and some variables, such as the c.g. location, vary during the flight. Another disadvantage is that with flying a real aircraft very high values of angle of attack and angle of side slip are unable to be captured. It is not easily doable and also unsafe to put an aircraft for example in a spin, to capture the effects an angle of attack up to 90 degrees. Lastly obtaining real life flight data is most likely the most expensive option of obtaining stall data. This last disadvantage might make it impossible, economically wise, to make a stall model, especially for smaller aircraft.

2-2-2 Representative Model

Another way of obtaining aerodynamic data is by using wind tunnel experiments and CFD analysis. Wind tunnel testing for studying stall and post-stall dynamics has already been done for fighter jets in the past (Nguyen et al., 1979). The National Aeronautics and Space Administration (NASA) however also conducted a research on aerodynamic modeling of post-stall and spin dynamics of large transport airplanes (Murch & Foster, 2007). This has been done in a wind tunnel as well, where both static and dynamic aerodynamic derivatives were estimated. The latter are predicted by forced oscillations in a wind tunnel. The disadvantage of using wind tunnel data is that the Reynolds number does not match that of the real aircraft most often. To compensate for this effect so called Reynolds number scaling has to be applied to get the correct aerodynamic coefficients (Laster, Stanewsky, Sinclair, & Sickles, 1998). Wind tunnel tests however are also known to be rather expensive. Therefore the modeling of a representative model is often assisted by CFD analysis. Stall dynamics however tend to be very nonlinear, which can be hard to solve using CFD analysis. When using CFD analysis it is also necessary to have an accurate 3D model of an aircraft, which can be also very costly and time consuming to obtain. Lastly stalls are dynamic, meaning that the CFD meshes need to be modified between time-steps, making the approach computationally expensive.

2-2-3 Geometry Based Model

Since acquiring a specific model or representative model can be time consuming and more importantly costly, current research is also going into geometry based stall modeling. It is possible to combine (simple) CFD analysis with geometry based modeling (Nie et al., 2015). Another method is to use a baseline aircraft and model the effects of different configurations (Teng, Zhang, Liu, & Grant, 2015). The disadvantage of the latter one however is that it is still based on a baseline aircraft of which the stall dynamics are known. It is a promising research field however, especially since it is low cost compared to the specific model and representative model.

2-2-4 Phenomenological Model

A last possibility to create a stall model is purely phenomenological. As described in the previous section the basic features of the stall dynamics are known. It is known that the static/ dynamic lateral-directional stability degrades as well as the control responses among other features. These characteristics of a stall can be easily implemented without modeling the modeling the aerodynamics precisely. For example the aileron effectiveness on the roll ($C_{l_{\delta_a}}$) can be assumed to be a function of angle of attack, where at higher angles of attack it tends to go to zero. Although this does not precisely model the stall dynamics, it might be sufficient to train pilots the correct behavior. A research to using different models has already been done by (Schroeder et al., 2014). Where it was concluded that an alternative approach, by using: wind tunnel data, CFD analysis and a SME could be feasible. A purely phenomenological has not been tested yet however.

2-3 State of the art

Stall modeling is not a new field of research. Simulation of high angle of attack maneuvers for fighter jets (O'Rourke et al., 1997),(Kay et al., 1997),(O'Connor, Ralston, & Fitzgerald, 1996). These models were mainly based on wind tunnel data, this included both static tests and dynamic tests using a rotary balance (Malcolm, 1985).

Current research however not only focuses on fighter jets, but also on general aviation and large transport jets. An European effort into stall modeling has been performed by the SUPRA project. During this project a stall model for a generic transport aircraft has been created, mainly based on wind tunnel and CFD data (Abramov et al., 2012). Another contribution was made by NASA, who has researched the development of upset conditions for large transport aircraft. One issue regarding wind tunnel modeling is the aerodynamic scale effects, e.g. Reynolds number (Foster et al., 2005).

Another method for obtaining aerodynamic stall models is using semi-empirical and analytical data, which uses computational methods such as the Vortex Lattice Methods (VLM). These methods are mostly used for preliminary design of an aircraft (Nie et al., 2015), but have been successful for stall simulation as well (Gingras et al., 2014),(Schroeder et al., 2014). This could even be taken a step further, by modeling the stall characteristics of each part of the aircraft (Teng et al., 2015).

Although such an semi-emperical model has been used succesfully, it does not represent a stall as precise as a stall model based on flight data. Using a combination of wind tunnel data, CFD and flight data is the current practice of creating realistic stall models. Currently, when basing a stall model on flight data, specifically designed input maneuvers have been applied for parameter identification (Morelli, Cunningham, & Hill, 2013),(Weiss, Friehmelt, Plaetschke, & Rohlf, 1996). A comparison between a quasi-steady stall and a dynamic stall has made, showing that the quasi-steady stall model was less robust (Dias, 2015). It is currently unpublished however, which stall characteristics can be modeled using such quasi-steady stalls. That is where this research will fill the gap in knowledge. Using a mathematical model of a stall, based on Kirchoff's flow separation theory (Fischenberg & Jategaonkar, 1999),(Singh & Jategaonkar, 1996), a stall model will be created using only quasi-steady stall data. It will then be shown which stall characteristics are identifiable using such quasi-steady stalls.

2-4 Kirchoff's Flow Separation Theory

As discussed before an approximation of Kirchoff's theory of flow separation can be used to model the hysteresis and other nonlinear effects during a stall (Fischenberg, 1995). The main idea is to let the function of the lift coefficient depend on the flow separation point on the wing. This can be done using Eq. 2-7, where 'X' is the flow separation point w.r.t. the chord of the wing.

$$C_L\left(\alpha, X\right) = C_{L_\alpha}\left\{\frac{1+\sqrt{X}}{2}\right\}^2 \alpha \tag{2-7}$$

This equation can of course also be extended with other terms such as C_{L_0}, C_{L_q} and $C_{L_{\delta_e}}$. For demonstrating purposes however these effects, except for C_{L_0} will be excluded. For the final stall model however the effects due to pitch rate and elevator deflection will be included. In Eq. 2-8 the formulation for the flow separation point is given. The flow separation point is a normalized coordinate, i.e. it has a value between zero and one, where a value of one means that flow is attached and a value of zero indicates a fully separated flow.

$$\tau_1 \frac{dX}{dt} + X = \frac{1}{2}\left\{1 - \tanh\left(a_1\left(\alpha - \tau_2\dot{\alpha} - \alpha^*\right)\right)\right\} \tag{2-8}$$

As can be seen in Eq. 2-8, the flow separation point is a function of the angle of attack and the angle of attack rate. In total there are four parameters that can be used to tune this function, i.e.: τ_1, τ_2, a_1 and α^*. To reduce the complexity for parameter estimation the parameter τ_1 is often excluded. In this section however the effects of each of the four parameters will be discussed. First the parameters a_1 and α^* will be investigated, these parameters have an effect on the steady effects. This can be easily seen if τ_1 is set to zero and it is assumed that $\dot{\alpha} = 0$ then the flow separation point is only a function of the angle of attack itself:

$$X_0 = \frac{1}{2}\left\{1 - \tanh\left(a_1\left(\alpha - \alpha^*\right)\right)\right\} \tag{2-9}$$

After the steady effects are discussed the parameters influencing the dynamic effects, i.e. τ_1 and τ_2 will be investigated.

2-4-1 Parameter a_1

The parameter a_1, as given in Eq. 2-9 is the parameter that influences the abruptness of the stall. The effect can be seen in Figure 2-9. A low value of a_1 indicates that the stall is not very abrupt, while a high value does the opposite. A higher value of a_1 also increases the maximum obtainable lift coefficient.

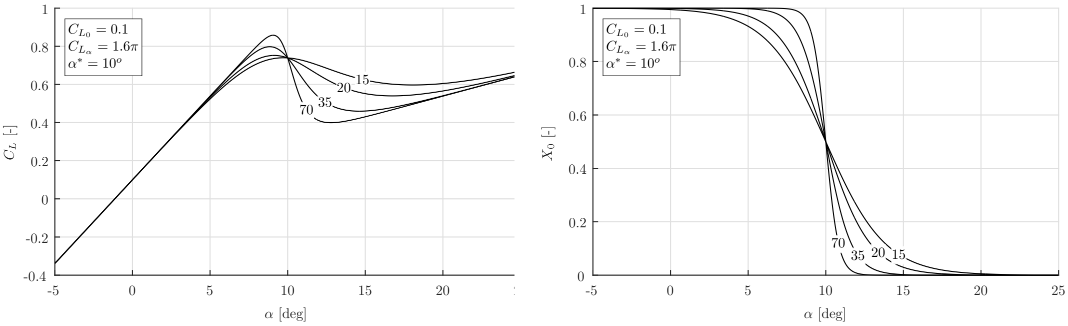

(a) Lift coefficient **(b)** Flow separation point

Figure 2-9: Effect of a_1 on the lift coefficient and flow separation point in steady conditions

2-4-2 Parameter α^*

The parameter α^* is the other parameter which influences the steady flow separation effects. This is a delay term for the flow separation. A higher value of α^* indicates an extended flow separation as shown in Figure 2-10. Due to the delay in flow separation with respect to the angle of attack the maximum lift coefficient as well as the critical angle of attack are increased.

2-4-3 Parameter τ_1

The effect of τ_1 influences the transient effects of the flow separation points as can be seen in Figure 2-11. The parameter τ_1 essentially influences the time delay of the flow separation point. A higher value indicates a larger delay whereas a lower value indicates a low time delay.

For showing the effects due to τ_1 and τ_2 an oscillating value is used for the angle of attack. The angle of attack is described by Eq. 2-10

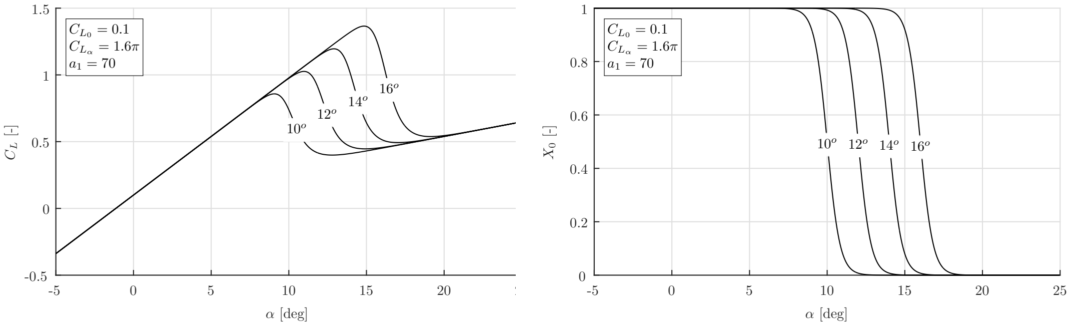

(a) Lift coefficient **(b)** Flow separation point

Figure 2-10: Effect of α^* on the lift coefficient and flow separation point in steady conditions

$$\alpha = 10^\circ - 10^\circ \cos(t), \quad t = [0, 2\pi] \tag{2-10}$$

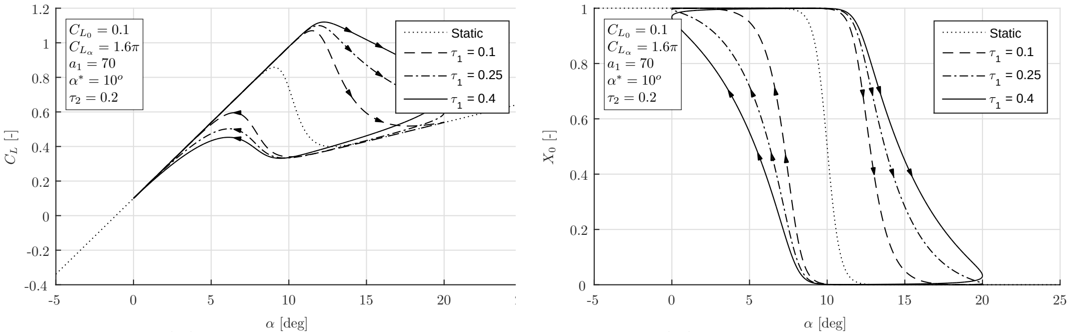

(a) Lift coefficient **(b)** Flow separation point

Figure 2-11: Effect of τ_1 on the lift coefficient and flow separation point in dynamic conditions

2-4-4 Parameter τ_2

The last tuning parameter is τ_2. This parameter can also be expressed as the hysteresis constant. A higher value indicates the flow separation occurs later, however flow reattachment occurs at lower angle of attack as well. This effect can be seen in Figure 2-12, where a graph is shown for two different values of τ_2.

2-5 Parameter Estimation

Due to the nonlinear hyperbolic tangent function, as given in Eq. 2-8, it not possible to apply linear optimization techniques such as ordinary least squares. More information on possible nonlinear optimization algorithms can be found in Chapter 4. In this section the equations will be given, that will be used for modeling the stall dynamics. The first equation is an extension of the lift equation as given in Eq. 2-7:

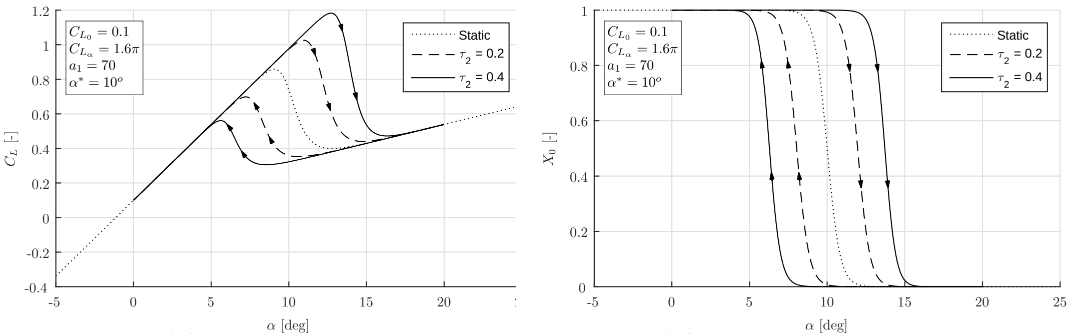

(a) Lift coefficient **(b)** Flow separation point

Figure 2-12: Effect of τ_2 on the lift coefficient and flow separation point in dynamic conditions

$$C_L = C_{L_\alpha} \left\{ \frac{1+\sqrt{X}}{2} \right\}^2 \alpha + C_{L_q} \frac{q\bar{c}}{V} + C_{L_{\delta_e}} \delta_e \tag{2-11}$$

The drag equation will be written somewhat different than using the well known standard polynomial. In this case the drag equation will be a function of the lift coefficient and an extra term on the flow separation point, as shown in Eq. 2-12

$$C_D = C_{D_0} + \frac{1}{e\pi\Lambda} C_L^2 + \frac{\partial C_D}{\partial X} (1 - X) \tag{2-12}$$

Lastly the equation for the moment coefficient is given by Eq. 2-13

$$C_m = C_{m_0} + C_{m_\alpha} \alpha + C_{m_q} \frac{q\bar{c}}{V} + C_{m_{\delta_e}} \delta_e + \frac{\partial C_m}{\partial X} (1 - X) \tag{2-13}$$

2-6 Lateral stall modeling

In the previous section only the equations for the longitudinal dynamics are given. Calculating the angle of attack for the two wings separately allows to model the asymmetric behavior of a stall (Fischenberg & Jategaonkar, 1999). The differential lift and drag can then be calculated as using Eqs. 2-14 and 2-15.

$$\Delta C_l = \left(C_{N_{left}} - C_{N_{right}} \right) \Delta y \tag{2-14}$$

$$\Delta C_n = \left(C_{T_{left}} - C_{T_{right}} \right) \Delta y \tag{2-15}$$

Where Δy is the effective lever arm. Furthermore:

$$\Delta C_L = C_N \cos(\alpha) - C_T \sin(\alpha) \tag{2-16}$$

$$\Delta C_D = C_T \cos(\alpha) + C_N \sin(\alpha) \tag{2-17}$$

This method however neglects both the horizontal and vertical tail surfaces. At high angles of attack however it is quite likely that these will (partially) be in the wake of the main wing. Therefore the main wing has the most influence on the lateral behavior during stall. This still has to be investigated though.

2-7 Model blending

The stall model must be blended together with a certain baseline model. It seems for now that the easiest way in doing so is by blending the output of the models, i.e. the forces and moments, together. This blending will be done using two sigmoid functions, as activation level. This is shown in Figure 2-13. In theory this should work fine, since the forces and moments that will be generated at the crossover by the two models should be approximately equal. It is however not yet done in practice.

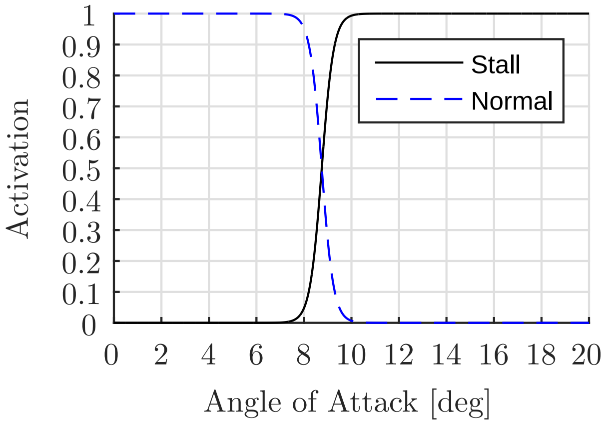

Figure 2-13: An example of an activation function, for blending the baseline and the stall models together.

2-8 Conclusion

In this chapter the main stall characteristics are presented. These include:

- Stall Hysteresis,
- Stall buffet,
- Uncommanded roll response or roll-off, requiring significant control deflection to counter,
- Apparent randomness or non-repeatability,
- Changes in pitch stability,

- Degradation in control response (pitch, roll, yaw),
- Degradation in static/dynamic lateral-directional stability,
- Mach effects,

Using Kirchoff's theory of flow separation a stall can be modeled, including the hysteresis effect. It must be noted however that after the stall angle a positive slope occurs for the C_L vs. α curve. Such an effect can happen with airfoils (Ostowari & Naik, 1985). The proposed model however does not drop after this small positive slope. Therefore this model will only be limited in terms of the angle of attack.

For modeling the lateral effects, the forces generated by both wings can be generated separately. A difference in normal force causes a rolling moment, whereas a difference in tangential force causes a yawing moment.

Chapter 3

Flight Path Reconstruction

The first step for (post-stall) model identification is FPR. With FPR the state of the aircraft, based on flight test data can be estimated. After the estimation of the aircraft state, it can be used for model identification. This chapter described the basics of FPR. First one of the most common used methods for FPR will be discussed, which is the Kalman Filter. Next to that Kalman smoothers will also be discussed. After that the kinematic and observation model that will be used are discussed. Furthermore the simulation model, especially the sensor model will be explained. Lastly a comparison between different Kalman Filters and smoothers will be given.

3-1 Kalman Filter

To estimate the state of a dynamic system based on measurements a Kalman Filter can be used. This section will described different types of Kalman Filters and smoothers. All these filters are based on the general description of a dynamic system given by:

$$\dot{\boldsymbol{x}}\left(t\right) = f\left(x\left(t\right), u\left(t\right), \boldsymbol{w}\left(t\right)\right) \tag{3-1}$$

$$\boldsymbol{y}\left(t\right) = h\left(\boldsymbol{x}\left(t\right), \boldsymbol{u}\left(t\right), \boldsymbol{v}\left(t\right)\right) \tag{3-2}$$

A Kalman Filter consist of two main parts. The first one being the prediction step and the second the correction step. The prediction step is based on the aircraft state, which is used to integrate the kinematics over a (usually small) time step. The correction step uses the measurement and the predicted measurement to correct the state. If a smoother is used a third step is involved, which is smoothing of the states after the Kalman Filter finished its forward run. A common Kalman Filter is the Iterated Extended Kalman Filter (IEKF). The Unscented Kalman Filter (UKF), is another Kalman Filter which is essentially a combination of a Kalman Filter and a Particle Filter. First the IEKF will be discussed, then the UKF. After those the smoothers will be discussed as well.

A Kalman Filter always has to be initialized with at least four "parameters": An initial state x_0, an initial covariance matrix P_0, the input noise matrix Q and the observation noise matrix R. The reason that an initial state is needed is that the prediction step is applied before the correction step. To make a prediction the state of the aircraft needs to be known. One way of obtaining an initial state is by using the first unfiltered measurement, as described by (Mulder et al., 1999). Just as with the initial state an initial covariance matrix is needed. The initial covariance is essentially a measure of how certain the estimation of the initial state is. A initial covariance of zero means that one is very certain about its initial state estimate. When the initial state estimate is very uncertain the initial covariance should be large as well.

The input noise matrix Q is essentially the uncertainty on the input for the state space system. If the uncertainty of the input is very large the Q-matrix should be large as well, if the uncertainty is low however the Q-matrix should be small. Normally the Q-matrix depends on the covariance of the input signals as follows:

$$Q := \begin{bmatrix} \sigma_{u_1}^2 & 0 & \cdots & 0 \\ 0 & \sigma_{u_2}^2 & 0 & 0 \\ \vdots & 0 & \ddots & 0 \\ 0 & 0 & 0 & \sigma_{u_n}^2 \end{bmatrix} \tag{3-3}$$

Where σ_u is the standard deviation of the input signal and n the number of input signals. Just as the input noise matrix the observation noise matrix R is a measure of the certainty of the measurements. Also here a R-matrix of zero indicates that one is very certain about the measurements, while a very large R-matrix indicates that one is very uncertain about its measurements. The R-matrix is defined as:

$$R := \begin{bmatrix} \sigma_{y_1}^2 & 0 & \cdots & 0 \\ 0 & \sigma_{y_2}^2 & 0 & 0 \\ \vdots & 0 & \ddots & 0 \\ 0 & 0 & 0 & \sigma_{y_m}^2 \end{bmatrix} \tag{3-4}$$

Where σ_y is the standard deviation of the measurement signal and m the number of measurement signals.

3-1-1 Iterated Extended Kalman Filter

The IEKF is an extension on the standard linear Kalman Filter. The method described here will be mainly based on (Mulder et al., 1999). The first step is the prediction step:

$$\hat{\underline{x}}_{k+1,k} = \hat{\underline{x}}_{k,k} + \int_{t_k}^{t_{k+1}} f\left(\hat{\underline{x}}_{k,k}, \underline{u}_k, t\right) dt, \quad x_{0,0} = x_0 \tag{3-5}$$

With the predicted state a predicted output can obtained:

$$\hat{\underline{y}}_{k,k+1} = h\left(\hat{\underline{x}}_{k+1,k}, \underline{u}_k\right) \tag{3-6}$$

The following step is the discretization of the state transition and input matrices, as follows:

$$\Phi_{k,k} = \sum_{n=0}^{\infty} \frac{F_x^n\left(\bullet\right)\left(t_{k+1} - t_k\right)^n}{n!} \tag{3-7}$$

$$\Gamma_{k,k} = \sum_{n=0}^{\infty} \frac{F_x^n\left(\bullet\right)\left(t_{k+1} - t_k\right)^n}{n!} \cdot F_u\left(\bullet\right) \tag{3-8}$$

Although it is not possible to calculate the sum till infinity, a high enough number would suffice in this case. The Jacobians F_x and F_u are given by:

$$F_x = \frac{\partial}{\partial \underline{x}} f\left(\underline{x}\left(t\right), \underline{u}\left(t\right)\right)\Big|_{\underline{x}=\hat{\underline{x}}_{k,k}} \tag{3-9}$$

$$F_u = \frac{\partial}{\partial \underline{u}} f\left(\underline{x}\left(t\right), \underline{u}\left(t\right)\right)\Big|_{\underline{x}=\hat{\underline{x}}_{k,k}} \tag{3-10}$$

Now the system is discretized, the covariance matrix can be calculated in the same manner as for the linear Kalman filter:

$$P_{k+1,k} = \Phi_{k,k}\left(\bullet\right) P_{k,k} \Phi_{k,k}^T\left(\bullet\right) + \Gamma_{k,k}\left(\bullet\right) Q\left(\bullet\right) \Gamma_{k,k}^T\left(\bullet\right), \quad P_{0,0} = P_0 \tag{3-11}$$

Where Q is the input noise matrix as explained earlier. After predicting the covariance matrix of the state the iterative part of the IEKF starts. If the error of the measurement update is small enough the following steps will be reiterated: First the Jacobian of the measurement equation is (re-) calculated:

$$H_x\left(\underline{\eta}_i\right) = \frac{\partial}{\partial x} \underline{h}\left(\hat{\underline{\eta}}_i, \underline{u}_k, t\right) \tag{3-12}$$

Where the initial iterator (η_0) is the predicted state: $\hat{\underline{x}}_{k+1,k}$.

After the Jacobian of the measurement equation is calculated, the Kalman gain can be (re-) calculated as well. This is done by:

$$K_{k+1}\left(\underline{\eta}_i\right) = P_{k+1,k}\left(\bullet\right) H_x^T\left(\underline{\eta}_i\right) \left[H_x\left(\underline{\eta}_i\right) P_{k+1,k}\left(\bullet\right) H_x^T\left(\underline{\eta}_i\right) + R\left(\bullet\right)\right]^{-1} \tag{3-13}$$

Where R is the observation noise matrix. The last part of the iterative part is the correction step:

$$\underline{\eta}_{i+1} = \hat{\underline{x}}_{k+1,k} + K_{k+1}\left(\underline{\eta}_i\right) \left[\underline{y}_{k+1} - h\left(\hat{\underline{x}}_{k+1,k}, \underline{u}_k\right) - H_x\left(\underline{\eta}_i\right) \left(\hat{\underline{x}}_{k+1,k} - \underline{\eta}_i\right)\right] \tag{3-14}$$

Where $\underline{y}_{k+1}$ is the measurement, which should not be confused with the predicted output $\hat{\underline{y}}_{k+1,k}$. The iteration part is terminated by two criteria:

$$\frac{\left|\left|\underline{\eta}_{i+1}-\underline{\eta}_{i}\right|\right|}{\left|\left|\underline{\eta}_{i}\right|\right|}<\epsilon \quad \text{or} \quad i>N_{max} \tag{3-15}$$

Where ϵ is usually a small number, e.g. $\epsilon = 10^{-10}$. The variable N_{max} is the maximum number of iterations before the iterator is terminated. When the iteration is terminated the one-step-ahead optimal state estimation ($\hat{\underline{x}}_{k+1,k+1}$) is set to the last value of the iterator: $\underline{\eta}_{i+1}$.

Finally in the last step of the IEKF the covariance matrix of the state estimation error is calculated as follows:

$$\begin{aligned}P_{k+1,k+1} = &\left[I - K_{k+1}\left(\hat{\underline{x}}_{k+1,k+1}\right) H_x\left(\hat{\underline{x}}_{k+1,k+1}\right)\right] P_{k+1,k}\left[I - K_{k+1}\left(\hat{\underline{x}}_{k+1,k+1}\right) H_x\left(\hat{\underline{x}}_{k+1,k+1}\right)\right]^T\\ &+ K_{k+1}\left(\hat{\underline{x}}_{k+1,k+1}\right) R\left(\bullet\right) K^T_{k+1}\left(\hat{\underline{x}}_{k+1,k+1}\right)\end{aligned} \tag{3-16}$$

3-1-2 Unscented Kalman Filter

The UKF has the advantage that no linearization is needed for the state reconstruction. This is especially useful in highly nonlinear dynamics. The UKF is based on the scaled unscented transformation as described by (Julier, 2002). The algorithm described here is mainly based on the work of (Wan & van der Merwe, 2000) and (Teixeira, Tôrres, Iscold, & Aguirre, 2011). The UKF involves creating so called sigma points ($\mathcal{X}$), which will be propagated trough the system dynamics equations. The sigma points are grouped in a matrix of $2L+1$ sigma vectors $\boldsymbol{\mathcal{X}}$, with L being the dimension of the state vector. The sigma vectors are calculated as:

$$\begin{aligned}\boldsymbol{\mathcal{X}}_0 &= \bar{\boldsymbol{x}}\\ \boldsymbol{\mathcal{X}}_i &= \bar{\boldsymbol{x}} + \sqrt{\left(L+\lambda\right)\boldsymbol{P_x}}, \quad i = 1, ..., L\\ \boldsymbol{\mathcal{X}}_i &= \bar{\boldsymbol{x}} - \sqrt{\left(L+\lambda\right)\boldsymbol{P_x}}, \quad i = L+1, ..., 2L\end{aligned} \tag{3-17}$$

In Eq. 3-17, $\bar{\boldsymbol{x}}$ is the expected value of $\boldsymbol{x}$, i.e.: $\bar{\boldsymbol{x}} = \mathbf{E}\left[\boldsymbol{x}\right]$. $\boldsymbol{P_x}$ is the covariance matrix of $\boldsymbol{x}$, i.e.: $\boldsymbol{P_x} = \mathbf{E}\left[\left(\boldsymbol{x}-\bar{\boldsymbol{x}}\right)\left(\boldsymbol{x}-\bar{\boldsymbol{x}}\right)^T\right]$, finally the parameter λ is defined as:

$$\lambda = \alpha^2\left(L+\kappa\right) - L \tag{3-18}$$

Where α and κ are scaling parameters. Corresponding to the sigma vectors are the weights, defined as:

$$\begin{aligned}W_0^{(m)} &= \lambda/\left(L+\lambda\right)\\ W_0^{(c)} &= \lambda/\left(L+\lambda\right) + \left(1-\alpha^2+\beta\right)\\ W_i^{(m)} &= W_i^{(c)} = 1/\left\{2\left(L+\lambda\right)\right\}, \quad i = 1, ..., 2L\end{aligned} \tag{3-19}$$

In Eq. 3-19, the value of β should be a non-negative value. For Gaussian distributions a value of $\beta = 2$ is optimal (Julier, 2002). So there are three tuning parameters for the UKF. The values of α of κ are used to set the distribution size of the sigma points around the mean as shown in Figure 3-1. The value of α can be set anywhere between zero and one, but normally a small value is taken, e.g. $1e-3$ (Wan & van der Merwe, 2000). The value for κ can be used as well for tuning the UKF and can be either negative or positive, as long as $\lambda \neq 0$. With a negative value of λ it is possible to calculate a non-positive, semi-definite $\boldsymbol{P_{k,k+1}}$ (Julier, Uhlmann, & Durrant-Whyte, 2000). In case a non-positive semi-definite covariance matrix is obtained the UKF will not work. This can be fixed by calculating the covariance around $\mathcal{X}_{0|k,k+1}$ instead of $\hat{\underline{x}}_{k,k+1}$, as described by Eq. 3-25.

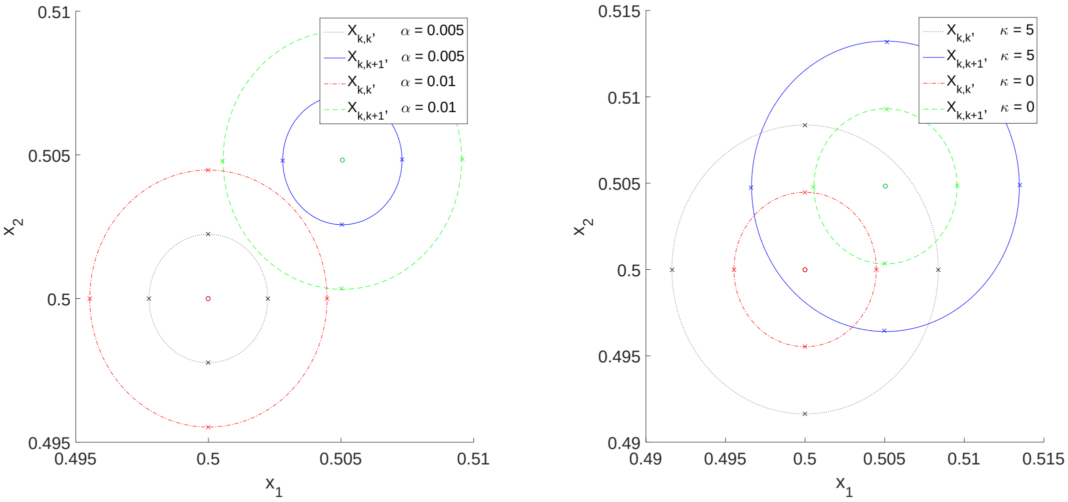

(a) Effect of α on the distribution of sigma points around the mean

(b) Effect of κ on the distribution of sigma points around the mean

Figure 3-1: Effect of tuning parameters of the UKF

Before creating the sigma points for use in the UKF, the state variable is expanded with process and observation noise variables: $\boldsymbol{x_k^a} = [\boldsymbol{x_k}\ \boldsymbol{v_k}\ \boldsymbol{w_k}]^T$. The augmented state vector is then given as:

$$\hat{\underline{\boldsymbol{x}}}^a_{k,k} = E\left\{\underline{\boldsymbol{x}}^a_{k,k}\right\} = \left\{\hat{\underline{\boldsymbol{x}}}_{k,k}\ \mathbf{0}\ \mathbf{0}\right\}^T \tag{3-20}$$

With the corresponding augmented covariance matrix:

$$P^a_{k,k} = E\left\{\underline{\boldsymbol{x}}^a_{k,k} - \hat{\underline{\boldsymbol{x}}}^a_{k,k}\right\} = \begin{bmatrix} P_{k,k} & 0 & 0 \\ 0 & Q & 0 \\ 0 & 0 & R \end{bmatrix} \tag{3-21}$$

Where Q is the input noise covariance matrix and R the process noise covariance matrix. With the definition of the augmented state vector and covariance matrix, the augmented sigma points can be calculated, as given in Eq. 3-22. Using the method as described by Eqs. 3-17 and 3-19.

$$\boldsymbol{\mathcal{X}}^a_{k,k} = \left[\underline{\hat{\boldsymbol{x}}}^a_{k,k} \quad \underline{\hat{\boldsymbol{x}}}^a_{k,k} + \sqrt{(L+\lambda)\,P^a_{k,k}} \quad \underline{\hat{\boldsymbol{x}}}^a_{k,k} - \sqrt{(L+\lambda)\,P^a_{k,k}}\right] = \left[(\boldsymbol{\mathcal{X}}^{\boldsymbol{x}})^T \;\; (\boldsymbol{\mathcal{X}}^{\boldsymbol{v}})^T \;\; (\boldsymbol{\mathcal{X}}^{\boldsymbol{w}})^T\right]^T \tag{3-22}$$

Where L is the dimension of the augmented state vector. Thus it is the dimension of the state space, plus the dimensions of the input and process noises. The value of λ is calculated by Eq. 3-18.

Now the augmented sigma points are calculated, it is time for the prediction step of the UKF. This involves a prediction of the state vector and measurement vector. First the sigma points are transformed through the nonlinear state space equations:

$$\boldsymbol{\mathcal{X}}^x_{k+1,k} = \boldsymbol{\mathcal{X}}^x_{k,k} + \int_{t_k}^{t_{k+1}} f\left(\boldsymbol{\mathcal{X}}^x_{k,k}, \boldsymbol{\mathcal{X}}^v_{k,k}, t\right) dt \tag{3-23}$$

Just as with the IEKF, an initial state vector and covariance matrix have to be determined prior to starting the UKF. The predicted state estimate is given as:

$$\underline{\hat{x}}_{k+1,k} = \sum_{i=0}^{2L} W_i^{(m)} \boldsymbol{\mathcal{X}}^x_{i|k+1,k} \tag{3-24}$$

The corresponding covariance matrix can be calculated by:

$$P_{k+1,k} = \sum_{i=0}^{2L} W_i^{(c)} \left[\boldsymbol{\mathcal{X}}^x_{i|k+1,k} - \underline{\hat{x}}_{k,k+1}\right] \left[\boldsymbol{\mathcal{X}}^x_{i|k+1,k} - \underline{\hat{x}}_{k,k+1}\right]^T \tag{3-25}$$

The prediction of the measurement is essentially the same as the prediction of the state vector:

$$\boldsymbol{\mathcal{Y}}_{k+1,k} = h\left(\boldsymbol{\mathcal{X}}^x_{k+1,k}, \boldsymbol{\mathcal{X}}^w_{k,k}\right) \tag{3-26}$$

$$\underline{\hat{y}}_{k+1,k} = \sum_{i=0}^{2L} W_i^{(m)} \boldsymbol{\mathcal{Y}}_{k+1,k} \tag{3-27}$$

After the prediction step is completed the correction step is performed. First the innovation covariance $P_{\hat{y}_k,\hat{y}_k}$ and the cross covariance $P_{\hat{x}_k,\hat{y}_k}$ are calculated:

$$P_{\hat{y}_k,\hat{y}_k} = \sum_{i=0}^{2L} W_i^{(c)} \left[\boldsymbol{\mathcal{Y}}_{k+1,k} - \underline{\hat{y}}_{k+1,k}\right] \left[\boldsymbol{\mathcal{Y}}_{k+1,k} - \underline{\hat{y}}_{k+1,k}\right]^T \tag{3-28}$$

$$P_{\hat{x}_k,\hat{y}_k} = \sum_{i=0}^{2L} W_i^{(c)} \left[\boldsymbol{\mathcal{X}}_{i|k+1,k} - \underline{\hat{x}}_{k+1,k}\right] \left[\boldsymbol{\mathcal{Y}}_{k+1,k} - \underline{\hat{y}}_{k+1,k}\right]^T \tag{3-29}$$

Then the Kalman Gain can be calculated as:

$$K_{k+1} = P_{\hat{x}_k,\hat{y}_k} P^{-1}_{\hat{y}_k,\hat{y}_k} \tag{3-30}$$

With the Kalman gain the corrected state and covariance matrix can be calculated:

$$\hat{\underline{x}}_{k+1,k+1} = \hat{\underline{x}}_{k+1,k} + K_{k+1}\left(\underline{y}_{k+1} - \hat{\underline{y}}_{k+1,k}\right) \tag{3-31}$$

$$P_{k+1,k+1} = P_{k+1,k} - K_{k+1} P_{\hat{y}_k,\hat{y}_k} K^T_{k+1} \tag{3-32}$$

3-2 Smoothers

Due to the offline nature of flight path reconstruction a Kalman smoother can be used as well. A Kalman Filter estimates the states given all observations from y_0 up to the current time k. A Kalman smoother however estimates the states given all observations from the past and the future. In this section two common Kalman smoother will be discussed. First the Kalman filter based on Euler discretization approximation will be discussed, which is mainly based on (Haykin, 2001). The derivation of this smoother is beyond the scope of this preliminary report, but a detailed derivation for the linear case can be found in (Lewis, Xie, & Popa, 2007). The second smoother is the Rauch-Tung-Striebel smoother (Rauch, Striebel, & Tung, 1965). Both an implementation is made for the IEKF, based on (Hartikainen, Solin, & Särkkä, 2011) and for the UKF, based on (Särkkä, 2008).

3-2-1 Euler Discretization Approximation

The main idea behind a Kalman smoother is to use data from both the past and the future to estimate the state. One way of doing so is by running a Kalman filter forward in time and a separate Kalman filter backwards in time. Both runs will then give a state estimate which can be combined together to obtain the smoothed state estimate. To run a Kalman filter backwards in time however the inverse kinematics of the system have to be known. Deriving these inverse kinematics from first principles is not an easy task though, especially for aircraft kinematics. One way of solving this is by training a backward predictor using a neural network, as proposed in (Haykin, 2001). This would make the Kalman smoother rather complicated however, since neural networks also have to be verified and validated over the whole range of inputs/ outputs.

Therefore, as proposed by (Särkkä, 2008; Teixeira et al., 2011), the inverse kinematics are obtained by changing the direction of time and applying Euler's discretization approximation. When the time steps are small, the kinematics can be considered to be linear. Meaning that inverting the kinematics is a simple as taking negative of $\dot{x}$. In equation form this can be expressed as:

$$\dot{x}\left(-t\right) = -f\left(x\left(-t\right), u\left(-t\right)\right) \tag{3-33}$$

Both the forward and backward pass produce a covariance and a state estimate. These two estimates are then combined using (Haykin, 2001):

$$(P_k^s)^{-1} = \left(P_k^f\right)^{-1} + \left(P_k^b\right)^{-1} \tag{3-34}$$

$$\underline{\hat{x}}_k^s = (P_k^s) \left[\left(P_k^f\right)^{-1} \underline{\hat{x}}_k^f + \left(P_k^b\right)^{-1} \underline{\hat{x}}_k^b \right] \tag{3-35}$$

Where superscript f means the data from the forward pass and b from the backward pass. The subscript k in Eq. 3-34 and Eq. 3-35 indicates the time step of the Kalman filter, which runs from zero to N. This essentially concludes the Kalman smoother based on the Euler discretization approximation.

3-2-2 Rauch-Tung-Striebel

Another method for applying a smoother is the so called Rauch-Tung-Striebel smoother. A full derivation of this smoother, based on the linear Kalman filter, can be found in (Rauch et al., 1965). This subsection will only describe the algorithm, once for the IEKF (Hartikainen et al., 2011) and once for the UKF (Särkkä, 2008).

Iterated Extended Rauch Tung Striebel Smoother

First the Rauch Tung Striebel (RTS) smoother for the IEKF will be discussed, this smoother will be called the Iterated Extended Rauch Tung Striebel Smoother (IERTSS). The main difference between the extended RTS and the original RTS is the same as for the Extended Kalman Filter (EKF) and the orginal Kalman filter, i.e. the linear A-matrix is replaced by the Jacobian (F_x). The first step for the Kalman smoother is to obtain the one step ahead prediction:

$$\underline{\hat{x}}_{k+1}^- = \underline{\hat{x}}_k + \int_{t_k}^{t_{k+1}} f\left(\underline{\hat{x}}_k, \underline{u}_k, t\right) dt \tag{3-36}$$

$$P_{k+1}^- = \Phi_k\left(\bullet\right) P_k \Phi_k^T\left(\bullet\right) + \Gamma_k\left(\bullet\right) Q\left(\bullet\right) \Gamma_k^T\left(\bullet\right) \tag{3-37}$$

Then the smoother gain can be calculated:

$$D_k = P_k \Phi_k \left[P_{k+1}^-\right]^{-1} \tag{3-38}$$

With the smoother gain, the smoothed covariance and state can be estimated:

$$P_k^s = P_k + D_k \left[P_{k+1}^s - P_{k+1}^-\right] D_k^T \tag{3-39}$$

$$\underline{\hat{x}}_k^s = \underline{\hat{x}}_k + D_k \left[\underline{\hat{x}}_{k+1}^s - \underline{\hat{x}}_{k+1}^-\right] \tag{3-40}$$

The values of $\underline{\hat{x}}_k$ and P_k are the state and covariance at time step k, where k runs from $N-1$ to zero. The initial conditions, which are needed for $\underline{\hat{x}}_{k+1=N}^s$ and $P_{k+1=N}^s$ are the last values of the state and covariance obtained by the IEKF.

Unscented Rauch Tung Striebel Smoother

The principle behind the Unscented Rauch Tung Striebel Smoother (URTSS) is the same as the IERTSS, however using the UKF as basis. This means that first a matrix of sigma points is created, using Eq. 3-22. These sigma points are then propagated through the dynamic model:

$$\boldsymbol{\mathcal{X}}^{-}_{k+1} = \boldsymbol{\mathcal{X}}^{x}_{k,k} + \int_{t_k}^{t_{k+1}} f\left(\boldsymbol{\mathcal{X}}^{x}_{k}, \boldsymbol{\mathcal{X}}^{v}_{k}, t\right) dt \tag{3-41}$$

These sigma points are then used to calculate the mean state, the predicted covariance and the cross-covariance as follows:

$$\underline{\hat{x}}^{-}_{k+1} = \sum_{i=0}^{2L} W_i^{(m)} \boldsymbol{\mathcal{X}}^{x}_{i|k+1} \tag{3-42}$$

$$P^{-}_{k+1} = \sum_{i=0}^{2L} W_i^{(c)} \left[\boldsymbol{\mathcal{X}}^{-}_{i|k+1} - \underline{\hat{x}}^{-}_{k+1}\right] \left[\boldsymbol{\mathcal{X}}^{-}_{i|k+1} - \underline{\hat{x}}^{-}_{k+1}\right]^T \tag{3-43}$$

$$C_{k+1} = \sum_{i=0}^{2L} W_i^{(c)} \left[\boldsymbol{\mathcal{X}}^{x}_{i|k+1} - \underline{\hat{x}}^{-}_{k+1}\right] \left[\boldsymbol{\mathcal{X}}^{-}_{i|k+1} - \underline{\hat{x}}_{k}\right]^T \tag{3-44}$$

Where the weights are the same as used for the UKF, as given in Eq. 3-19. Having the predicted covariance and cross covariance the smoother gain can be calculated:

$$D_{k+1} = C_{k+1}\left[P^{-}_{k+1}\right] \tag{3-45}$$

From which it is possible to calculate the smoothed state and covariance:

$$P^{s}_{k} = P_k + D_k\left[P^{s}_{k+1} - P^{-}_{k+1}\right] D_k^T \tag{3-46}$$

$$\underline{\hat{x}}^{s}_{k} = \underline{\hat{x}}_{k} + D_k\left[\underline{\hat{x}}^{s}_{k+1} - \underline{\hat{x}}^{-}_{k+1}\right] \tag{3-47}$$

Just as with the IERTSS, the URTSS runs from $N-1$ to zero, the initial conditions for the last smoothed state and covariance are the last state and covariance as estimated by the UKF.

3-3 Kinematic Model

The Kalman filter needs two models, a (nonlinear) system dynamic model and an observation model. This section will describe the former. The system dynamic model for aircraft FPR are essentially the kinematics for an aircraft in the Earth Centered Earth Fixed (ECEF) frame.

The most essential part of the kinematic model describeds the state of the aircraft, which is done by using the body velocities of the aircraft (u, v, w):

$$\begin{aligned}\dot{u} &= A_x - g\sin\theta - qw + rv \\ \dot{v} &= A_y + g\cos\theta\sin\phi - ru + pw \\ \dot{w} &= A_z + g\cos\theta\cos\phi - pv + qu\end{aligned} \tag{3-48}$$

And the attitude (Euler) angles (ϕ, θ, ψ):

$$\begin{aligned}\dot{\phi} &= p + (q\sin\phi + r\cos\phi)\tan\theta \\ \dot{\theta} &= q\cos\phi - r\sin\phi \\ \dot{\psi} &= q\frac{\sin\phi}{\cos\theta} + r\frac{\cos\phi}{\cos\theta}\end{aligned} \tag{3-49}$$

And finally the aircraft position (x_E, y_E, z_E):

$$\begin{aligned}\dot{x}_E &= [u\cos\theta + (v\sin\phi + w\cos\phi)\sin\theta]\cos\psi - (v\cos\phi - w\sin\phi)\sin\psi + W_{x_E} \\ \dot{y}_E &= [u\cos\theta + (v\sin\phi + w\cos\phi)\sin\theta]\sin\psi + (v\cos\phi - w\sin\phi)\cos\psi + W_{y_E} \\ \dot{z}_E &= -u\sin\theta + (v\sin\phi + w\cos\phi)\cos\theta + W_{z_E}\end{aligned} \tag{3-50}$$

In Eqs. 3-49 and 3-50 the values: A_x, A_y, A_z are the accelerations in the c.g. of the aircraft and p, q and r are the rotational rates. These six provide the input of the aircraft. The inputs however are most often biased, therefore an extra bias term will be added to inputs. The inputs are then as follows:

$$\begin{aligned}A_{x_m} &= A_x + \lambda_x + w_x \\ A_{y_m} &= A_y + \lambda_y + w_y \\ A_{z_m} &= A_z + \lambda_z + w_z \\ p_m &= p + \lambda_p + w_p \\ q_m &= q + \lambda_q + w_q \\ r_m &= r + \lambda_r + w_r\end{aligned} \tag{3-51}$$

Where the subscript m stands for the measured value, λ is the bias term and w is the white noise signal. In practice the measured value is thus the true value plus the bias term. To include bias terms Eqs. 3-49 and 3-50 have to be rewritten as follows:

$$\begin{aligned}\dot{u} &= (A_x - \lambda_x) - g\sin\theta - (q - \lambda_q)\,w + (r - \lambda_r)\,v \\ \dot{v} &= (A_y - \lambda_y) + g\cos\theta\sin\phi - (r - \lambda_r)\,u + (p - \lambda_p)\,w \\ \dot{w} &= (A_z - \lambda_z) + g\cos\theta\cos\phi - (p - \lambda_p)\,v + (q - \lambda_q)\,u\end{aligned} \tag{3-52}$$

$$\begin{aligned}
\dot{\phi} &= (p-\lambda_p) + (q-\lambda_q)\sin\phi\tan\theta + (r-\lambda_r)\cos\phi\tan\theta \\
\dot{\theta} &= (q-\lambda_q)\cos\phi - (r-\lambda_r)\sin\phi \\
\dot{\psi} &= (q-\lambda_q)\frac{\sin\phi}{\cos\theta} + (r-\lambda_r)\frac{\cos\phi}{\cos\theta}
\end{aligned} \tag{3-53}$$

The only problem left solving is to obtain the values for the biases (λ) and for the wind velocity (W_{x_E},W_{y_E},W_{z_E}). This problem can be solved by adding those to the state vector as well. It is assumed that the biases and wind velocities do not change in the time span of one maneuver and thus their derivatives are all set to zero. So at this moment the state vector consists of:

$$\boldsymbol{x} = [x \quad y \quad z \quad u \quad v \quad w \quad \phi \quad \theta \quad \psi \quad W_{x_E} \quad W_{y_E} \quad W_{z_E}]^T \tag{3-54}$$

The augmented state vector, i.e. the state vector including the bias terms is given by:

$$\boldsymbol{x_{aug}} = [\boldsymbol{x} \quad \lambda_x \quad \lambda_y \quad \lambda_z \quad \lambda_p \quad \lambda_q \quad \lambda_r]^T \tag{3-55}$$

3-4 Observation Model

The Kalman filter uses two steps, i.e. prediction and correction. For the correction step measurements are needed. These measurement either measure the state directly, such as the Euler angles or indirectly, e.g. the true airspeed. Next to that the input as defined in the previous section is a measurement as well. In the Cessna Citation II the measurements are provided by the Flight Test Instrumentation System (FTIS).

The Euler angles: ϕ, θ and ψ are directly measurable from the Attitude Heading Reference System (AHRS). The x and y locations in the ECEF are measured by the Global Positioning System (GPS) system and the altitude by the Digital Air Data Computer (DADC). Note however that the measured altitude is not equal to z_E, but rather to $-z_E$! Furthermore the rate of climb is also measured, and thus can be added as well to the observation equations.

Furthermore the true airspeed as measured by the DADC can be used for reconstructing the body velocities, since the true airspeed is defined as:

$$V_{TAS} := \sqrt{u^2 + v^2 + w^2} \tag{3-56}$$

Two very important measurements are the angle of attack (AOA) and angle of side slip (AOSS). They not only help with reconstructing the state, these measurements are also very important for creating an aerodynamic stall model. The main reason being that aerodynamic coefficients are often a function of: AOA (α), AOSS (β), Altitude (h) and Mach (M).

The angle of attack is measured by the angle of attack vane, which is measured on the right side of the fuselage in front of the wing. This vane, however, is mainly used for stall warning.

Therefore a noseboom with an AOA and AOSS vane can be mounted in front of the fuselage. These measurements however do not measure the true geometric angle of attack and angle of side slip as defined by Eqs. 3-57 and 3-58

$$\alpha := \arctan\left(\frac{w}{u}\right) \tag{3-57}$$

$$\beta := \arctan\left(\frac{u}{\sqrt{u^2+w^2}}\right) \tag{3-58}$$

The true measurements however are influenced by:

- Body induced velocities, such as an upwash component due to the fuselage. As illustrated in Figure 3-2
- Kinematic induced effects, such as the pitch rate (q).
- Unknown wind components

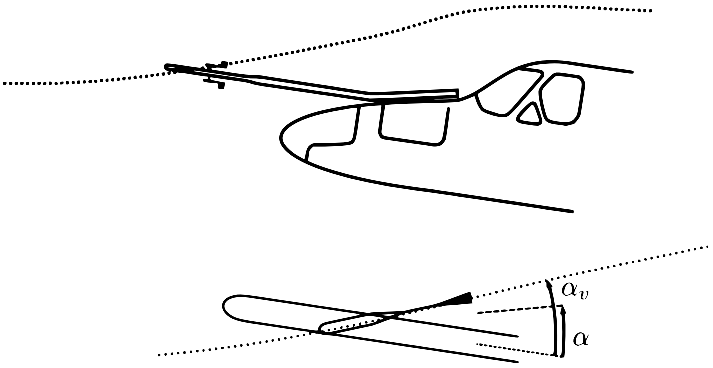

Figure 3-2: Fuselage induced velocity on the angle of attack vane (α_v), compared to the true geometric angle of attack (α) (Laban, 1994)

The measured angle of attack and angle of side slip are thus defined by (Laban, 1994; de Visser, 2011):

$$\alpha_v = \left(1 + C_{\alpha_{up}}\right)\alpha - \frac{(q-\lambda_q)\,x_{v_\alpha}}{V_{TAS}} + C_{\alpha_0} \tag{3-59}$$

$$\beta_v = (1 + C_{\beta_{si}})\,\beta - \frac{(r-\lambda_r)\,x_{v_\beta}}{V_{TAS}} + \frac{(p-\lambda_p)\,z_{v_\beta}}{V_{TAS}} + C_{\beta_0} \tag{3-60}$$

This however introduces seven more unknown variables: $C_{\alpha_{up}}$, C_{α_0}, $C_{\beta_{si}}$, C_{β_0}, x_{v_α}, x_{v_β} and z_{v_β}. The latter three can be measured, since these are the distances between the c.g. and the vane in longitudinal and vertical direction. That leaves only four extra variables to be estimated. These could be included into the state as well, just as the wind velocities and IMU biases. The state, as defined in Eq. 3-54 must then rewritten as:

$$\boldsymbol{x} = \begin{bmatrix} x & y & z & u & v & w & \phi & \theta & \psi & W_{x_E} & W_{y_E} & W_{z_E} & C_{\alpha_{up}} & C_{\alpha_0} & C_{\beta_{si}} & C_{\beta_0} \end{bmatrix}^T$$

Furthermore the rotational rates and body accelerations are directly measured as well. Although the position of rotational rate measurement does not have a influence on the measurement as shown in Figure 3-3, the position of the body acceleration measurements does have an effect. Preferably the body accelerations A_x, A_y and A_z should be measured in the center of gravity.

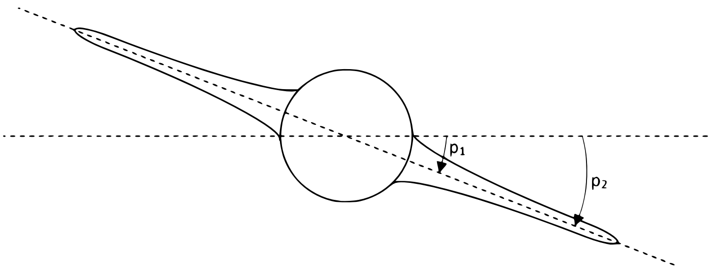

Figure 3-3: Schematic view of an aircraft, showing that the position of the rotational rate measurements is irrelevant.

Since the avionic upgrade for the Cessna Citation II the IMU measurements come from the ARINC system. This means that the accelerations are not measured close to the c.g. anymore. With the new FTIS system the linear acceleration measurements are now beneath the floor of the nose baggage compartment. This compartment is in front of the front pressure bulkhead, as shown in Figure 3-4

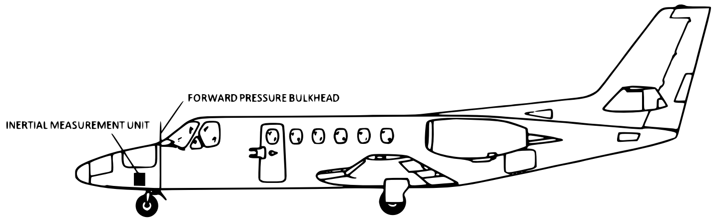

Figure 3-4: Position of the IMU of the ARINC FTIS

The c.g. of the Cessna Citation II on the other hand has the limits as described in Table 3-1, where the Datum is 2.39 meters forward of the front face of the forward pressure bulkhead (Cessna Aircraft Company, 2009).

This means that the distance between the center of gravity and the IMU is approximately five meters in longitudinal direction. Since the IMU is beneath the noise baggage compartment it is also likely that there is a small distance in the vertical direction as well. This distance can be corrected for, using Eq. 3-61, as indicated by (de Visser, 2011) and (Laban, 1994). One problem however is that for this correction the angular accelerations are needed. Although this might seem to be simply solved by differentiating the angular rates, it must be noted that these rates contain biases and noise. Furthermore there might be a misalignment in the IMU, meaning that the IMU axes are not perfectly aligned with the aircraft body axes. Thus

Table 3-1: Forward and Aft limit from Datum of the Cessna Citation 550 II, with gear extended (Cessna Aircraft Company, 2009).

Forward Limit:		
	≥ 3,874 kg & ≤ 6,033 kg	7.01- 7.11 m
	≤ 3,874 kg	7.01 m
Aft Limit:		
	≤ 6,033 kg	7.26 m

when trying to apply this correction it is most likely that an error will be introduced, which might not be necessarily better than ignoring the correction step.

$$\begin{aligned}
A_{x_{cg}} &= A_{x_{ac}} + (x_{cg} - x_{ac})\left(q^2 + r^2\right) - (y_{cg} - y_{ac})(pq - \dot{r}) - (z_{cg} - z_{ac})(pr - \dot{q}) \\
A_{y_{cg}} &= A_{y_{ac}} + (y_{cg} - y_{ac})\left(r^2 + p^2\right) - (z_{cg} - z_{ac})(qr - \dot{p}) - (x_{cg} - x_{ac})(qp - \dot{r}) \\
A_{z_{cg}} &= A_{z_{ac}} + (z_{cg} - z_{ac})\left(p^2 + q^2\right) - (x_{cg} - x_{ac})(rp - \dot{q}) - (y_{cg} - y_{ac})(rq - \dot{p})
\end{aligned} \tag{3-61}$$

3-5 State Observability

As described in the previous two sections a kinematic model and observation model can be made, the complete set is given by:

$$\begin{aligned}
\dot{\boldsymbol{x}} &= f\left(\boldsymbol{x}(t), \boldsymbol{u_m}(t), \boldsymbol{w}(t)\right) \\
&= \begin{bmatrix}
\left[u\cos\theta + (v\sin\phi + w\cos\phi)\sin\theta\right]\cos\psi - (v\cos\phi - w\sin\phi)\sin\psi + W_{x_E} \\
\left[u\cos\theta + (v\sin\phi + w\cos\phi)\sin\theta\right]\sin\psi + (v\cos\phi - w\sin\phi)\cos\psi + W_{y_E} \\
-u\sin\theta + (v\sin\phi + w\cos\phi)\cos\theta + W_{z_E} \\
(A_x - \lambda_x) - g\sin\theta - (q - \lambda_q)w + (r - \lambda_r)v \\
(A_y - \lambda_y) + g\cos\theta\sin\phi - (r - \lambda_r)u + (p - \lambda_p)w \\
(A_z - \lambda_z) + g\cos\theta\cos\phi - (p - \lambda_p)v + (q - \lambda_q)u \\
(p - \lambda_p) + (q - \lambda_q)\sin\phi\tan\theta + (r - \lambda_r)\cos\phi\tan\theta \\
(q - \lambda_q)\cos\phi - (r - \lambda_r)\sin\phi \\
(q - \lambda_q)\frac{\sin\phi}{\cos\theta} + (r - \lambda_r)\frac{\cos\phi}{\cos\theta} \\
\mathbf{0}_{13\times 1}
\end{bmatrix}
\end{aligned} \tag{3-62}$$

With:

$$\begin{aligned}
\boldsymbol{x} = \big[&x \quad y \quad z \quad u \quad v \quad w \quad \phi \quad \theta \quad \psi \quad W_{x_E} \quad W_{y_E} \quad W_{z_E} \quad C_{\alpha_{up}} \quad C_{\alpha_0} \\
&C_{\beta_{si}} \quad C_{\beta_0} \quad \lambda_x \quad \lambda_y \quad \lambda_z \quad \lambda_p \quad \lambda_q \quad \lambda_r\big]^T
\end{aligned} \tag{3-63}$$

And the observation model:

$$\begin{aligned}
\boldsymbol{y} &= h\left(\boldsymbol{x}\left(t\right), \boldsymbol{u_m}\left(t\right), \boldsymbol{v}\left(t\right)\right) \\
\begin{bmatrix} x_{gps} \\ y_{gps} \\ h_{DADC} \\ \dot{h}_{DADC} \\ \phi_{AHRS} \\ \theta_{AHRS} \\ \psi_{AHRS} \\ V_{TAS} \\ \alpha_v \\ \beta_v \end{bmatrix} &= \begin{bmatrix} x \\ y \\ -z \\ u\sin\theta - \left(v\sin\phi + w\cos\phi\right)\cos\theta - W_{z_E} \\ \phi \\ \theta \\ \psi \\ \sqrt{u^2+v^2+w^2} \\ \left(1+C_{\alpha_{up}}\right)\arctan\left(\frac{w}{u}\right) - \frac{(q-\lambda_q)x_{v_\alpha}}{V_{TAS}} + C_{\alpha_0} \\ \left(1+C_{\beta_{si}}\right)\arctan\left(\frac{v}{\sqrt{u^2+w^2}}\right) - \frac{(r-\lambda_r)x_{v_\beta}}{V_{TAS}} + \frac{(p-\lambda_p)z_{v_\beta}}{V_{TAS}} + C_{\beta_0} \end{bmatrix}
\end{aligned} \tag{3-64}$$

These represent the full kinematic and observation models. One question that comes to mind now is whether or not the whole state is observable. The calculation of this observability is not so trivial and often only local observability, i.e. around a point x_0 can be proved (Hermann & Krener, 1977). There are several methods for calculating the nonlinear observability, in this thesis however the algorithm as explained by (Walcott, Corless, & Zak, 1987) will be used, which has been used before by (de Visser, 2011). The nonlinear observability matrix is given by Eq. 3-65

$$\mathcal{O} = \begin{bmatrix} L_f^0 h\left(x\right) \\ L_f^1 h\left(x\right) \\ L_f^2 h\left(x\right) \\ \vdots \\ L_f^{n-1} h\left(x\right) \end{bmatrix} \tag{3-65}$$

Where n is the dimension of the system. The term $L_f h\left(x\right)$ is the Lie derivative of $h\left(x\right)$ with respect to $f\left(x\right)$, which can be calculated as follows:

$$L_f h\left(x\right) = \frac{\partial h}{\partial x}\left(x\right) f\left(x\right) \tag{3-66}$$

The Lie derivative thus represents the directional derivative of $h\left(x\right)$ along the direction of $f\left(x\right)$. The recursive set of Lie derivatives as given in Eq. 3-65 can be defined as:

$$\begin{aligned}
L_f^0 h\left(x\right) &= h\left(x\right) \\
L_f^1 h\left(x\right) &= L_f h\left(x\right) \\
L_f^2 h\left(x\right) &= L_f L_f h\left(x\right) \\
&\vdots \\
L_f^{n-1} h\left(x\right) &= L_f\left(L_f^{n-2} h\left(x\right)\right)
\end{aligned} \tag{3-67}$$

The nonlinear observability matrix, as given in Eq. 3-65, has the same form as the Kalman rank condition for observability. It can also be shown that in the linear case Eq. 3-65 turns into the Kalman rank condition. This proof is given by (Hermann & Krener, 1977), but is outside the scope of this thesis.

The calculation of the derivatives can become quiet tedious to do by hand, therefore the symbolic toolbox within MATLAB is used. It can be shown that the state as described by Eq. 3-63 can be (locally) observed by the observation model as described by Eq. 3-64. The state values for the state were given as the initial values for a simulated 3211 elevator maneuver, being (in SI units):

$$\begin{aligned}\boldsymbol{x}_0 = [&0 \quad 0 \quad -5000 \quad 100 \quad 0 \quad 0 \quad 0 \quad 0.6 \quad 0 \quad 0 \quad 0 \quad 0 \quad 0.2 \quad 0 \\ &0 \quad 0 \quad 0 \quad 0 \quad 0 \quad 0 \quad 0 \quad 0]^T\end{aligned} \tag{3-68}$$

In fact the full rank for the nonlinear observability was reached after calculating Eq. 3-65 up until $n = 3$. This analytical observability proof however is not a proof that the Kalman Filter will converge. Using the DASMAT model, trimmed at 5000 m and 100 m/s, and an added observation model as will be explained in Section 3-6, a simulation run was done using the full state and observation equations as described by Eq 3-62 and q 3-64 respectively. This was filtered with an UKF, because the UKF is more robust to initial conditions than the IEKF, as will be explained in Section 3-7. The results are shown in Figures 3-5, 3-6, 3-7 and 3-8. As can be seen the Kalman filter converges rather well. It must be noted however that the system in this case is fully excited, i.e. in longitudinal, lateral and vertical directions. If the system, i.e. the aircraft, is only excited in one direction the Kalman filter does not converge nicely. In Figures 3-9, 3-10, 3-11 and 3-12 this effect is shown, where only a 3-2-1-1 input on the elevator is given. It is expected that in this case the lateral components such as the angle of side slip and their components: $C_{\beta_{si}}$ and C_{β_0} do not optimally converge. In this case however the angle of attack is not converging very well either. Thus it looks as if the Kalman filter is not really robust when using the whole state, although it is fully observable.

Using the full state as given in Eq. 3-63 might thus give false information about the true state. To solve this problem some parameters from the state can be removed. The first parameter that was removed was the vertical wind component W_{z_E}, doing so means that it is assumed that the vertical wind component is zero. Most flight tests are made in fair weather, in which vertical wind components are in the order of 0.1 to 0.2 m/s (Mulder, Sridhar, & Breeman, 1994). Not only is the vertical wind component relatively small, but the extra induced angle of attack $\left(\alpha_w = \arctan\left(\frac{W_{z_E}}{V_{TAS}}\right)\right)$ is small as well and therefore can be neglected.

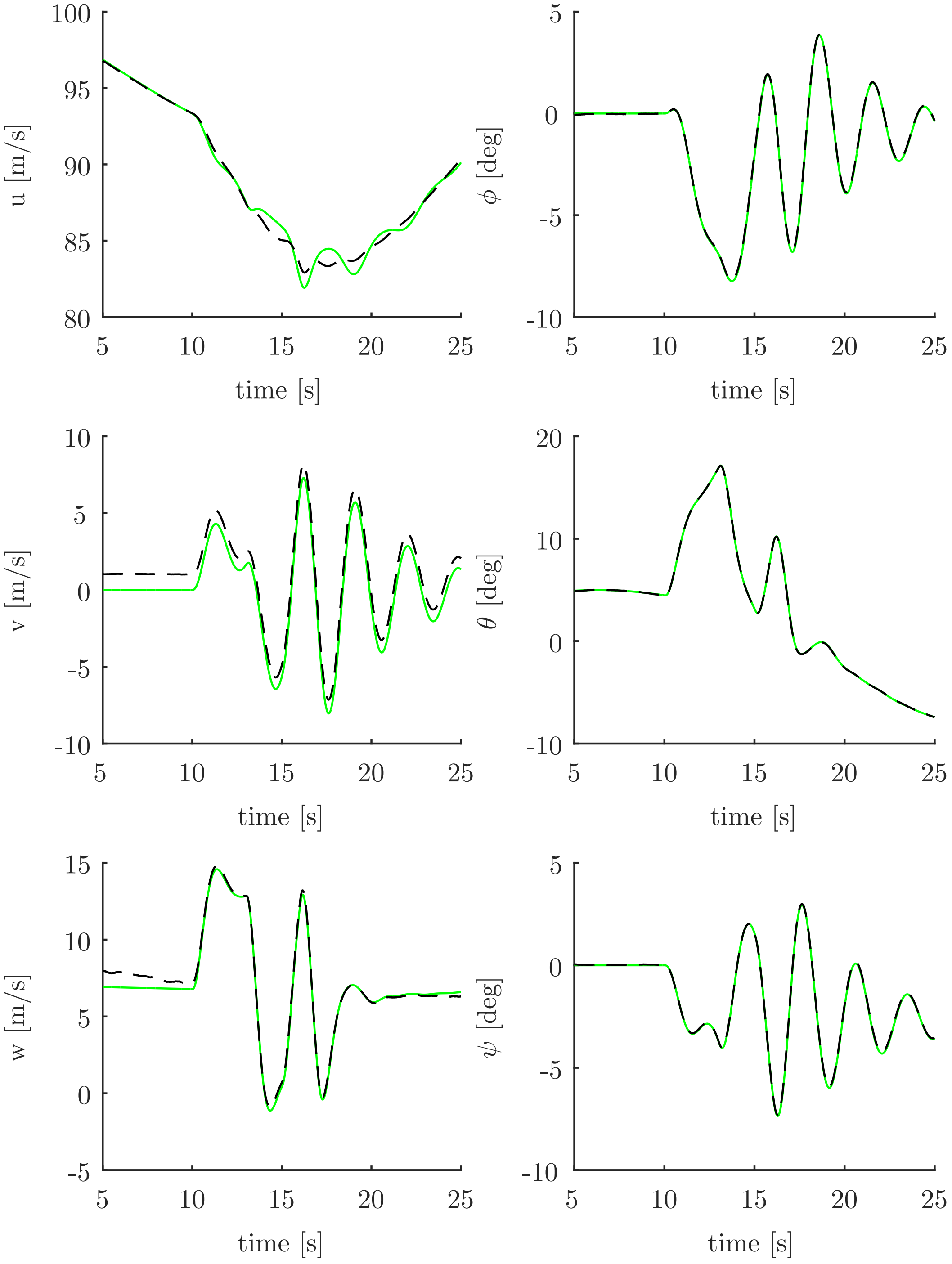

Figure 3-5: The Euler angles and body velocities, filtered by an UKF, using the full state: $\in \mathbb{R}^{22}$. With the true value (green-solid) and the estimated value (black-dashed). With a simultaneous de3211 and dr3211 input.

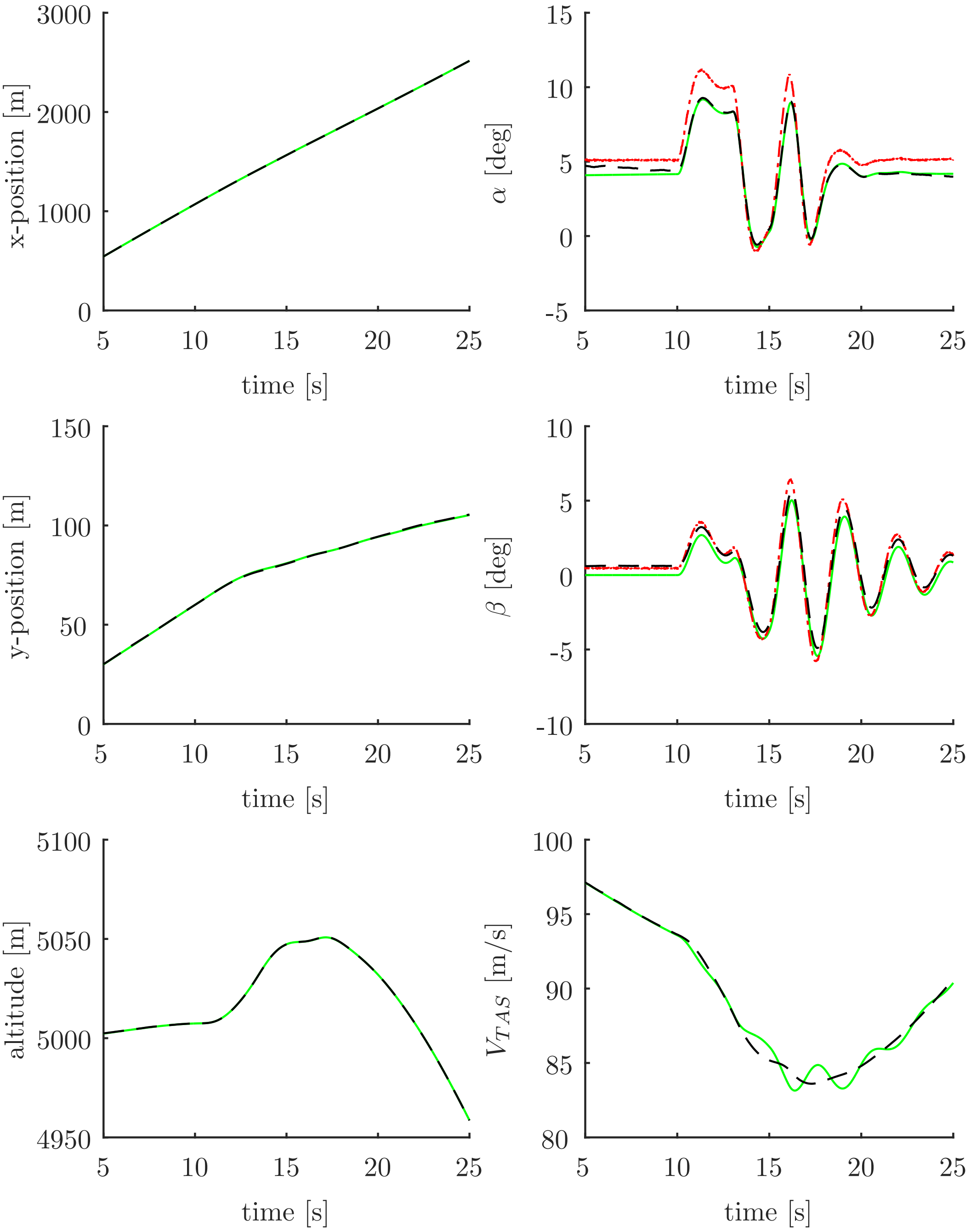

Figure 3-6: The position and air data, filtered by an UKF, using the full state: $\in \mathbb{R}^{22}$. With the true value (green-solid), the estimated value (black-dashed) and the measured value (red-dashed/dotted). With a simultaneous de3211 and dr3211 input.

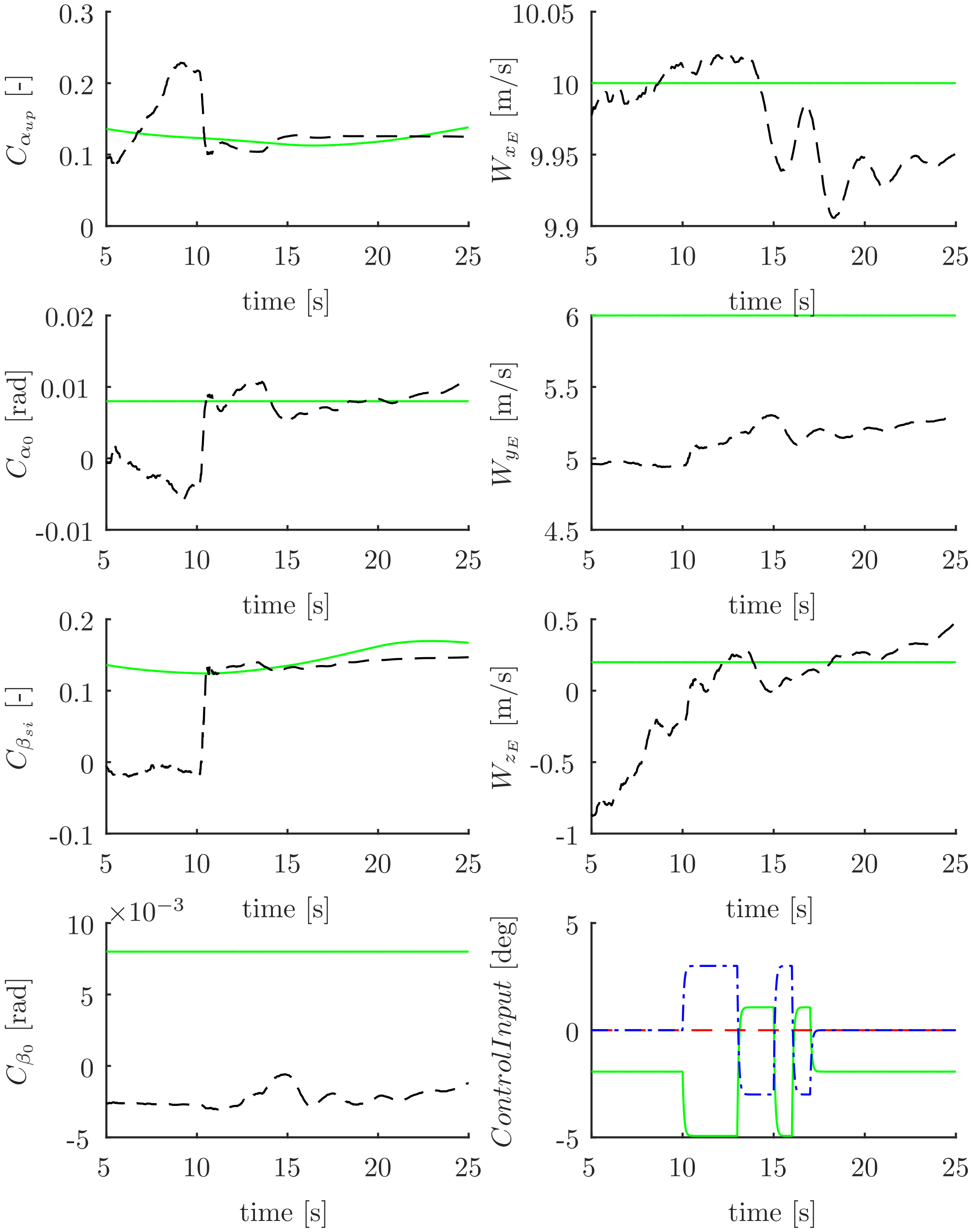

Figure 3-7: The coefficients influencing air flow measurement and wind velocities, using the full state: $\in \mathbb{R}^{22}$. With the true value (green-solid) and the estimated value (black-dashed). With a simultaneous de3211 and dr3211 input. For the control input on the bottom right plot: δ_e: green-solid, δ_a: red-dashed, δ_r: blue-dashed/dotted

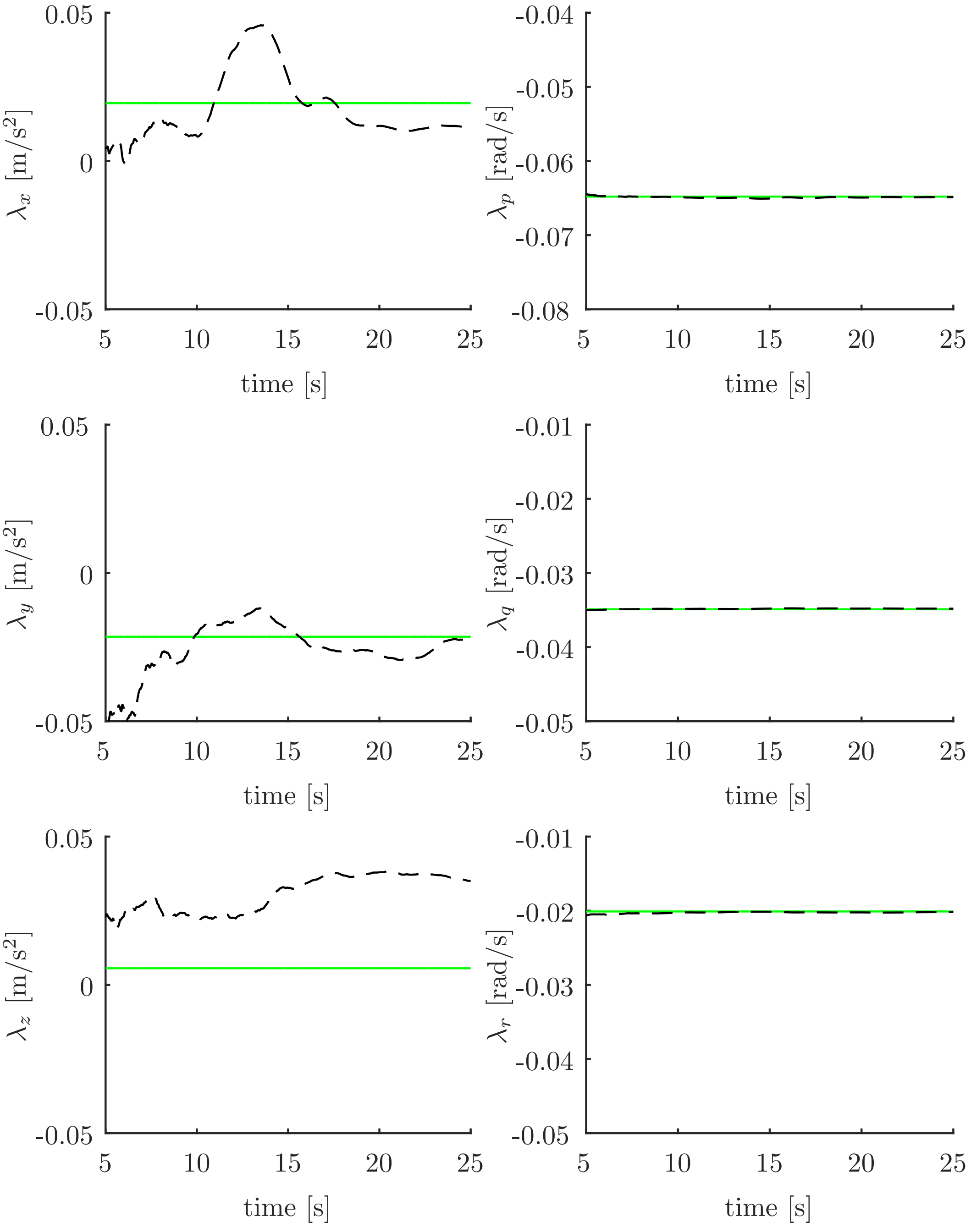

Figure 3-8: The IMU biases, filtered by an UKF, using the full state: $\in \mathbb{R}^{22}$. With the true value (green-solid) and the estimated value (black-dashed). With a simultaneous de3211 and dr3211 input.

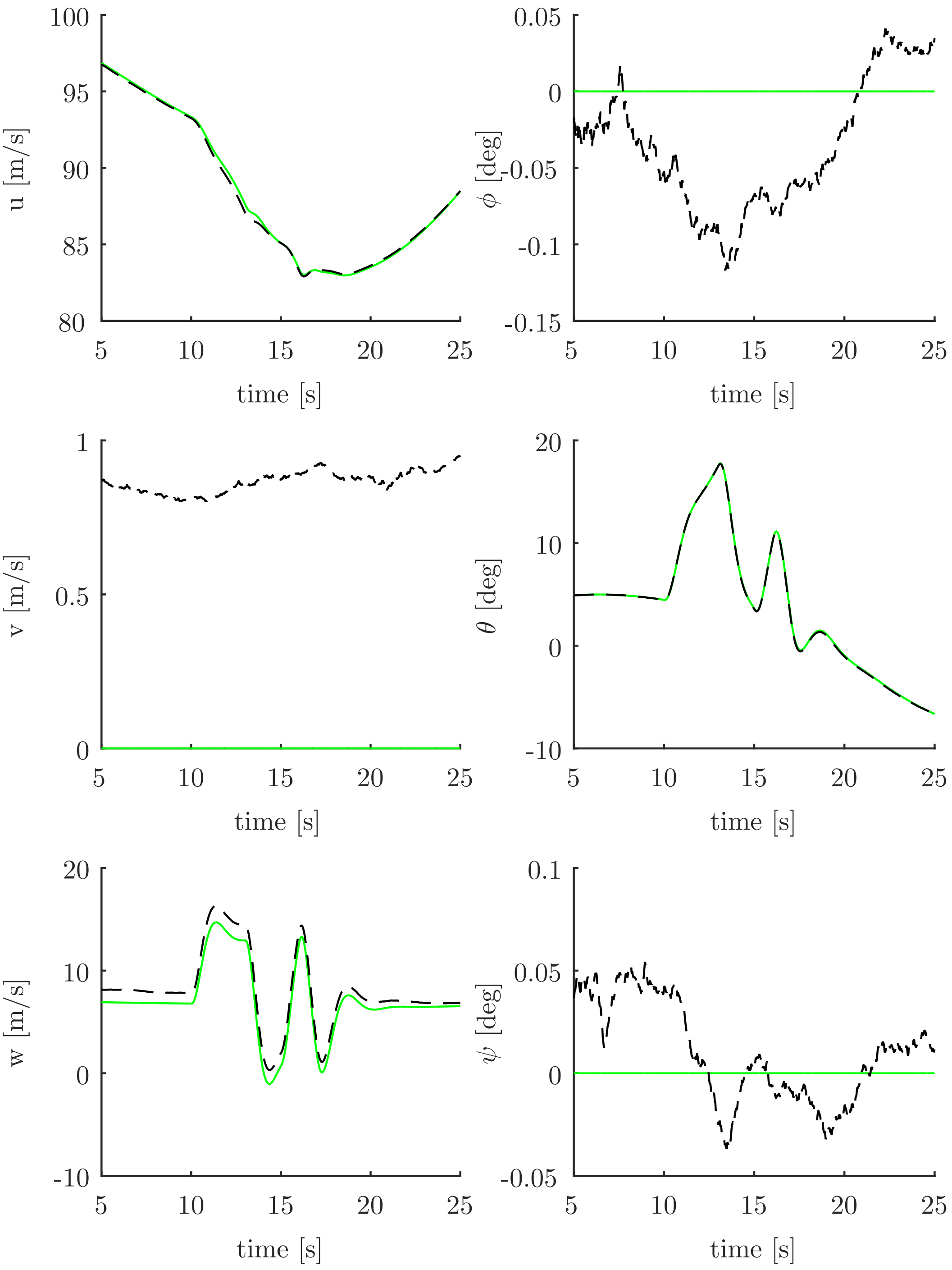

Figure 3-9: The Euler angles and body velocities, filtered by an UKF, using the full state: $\in \mathbb{R}^{22}$. With the true value (green-solid) and the estimated value (black-dashed). With only a 3211 input on the elevator.

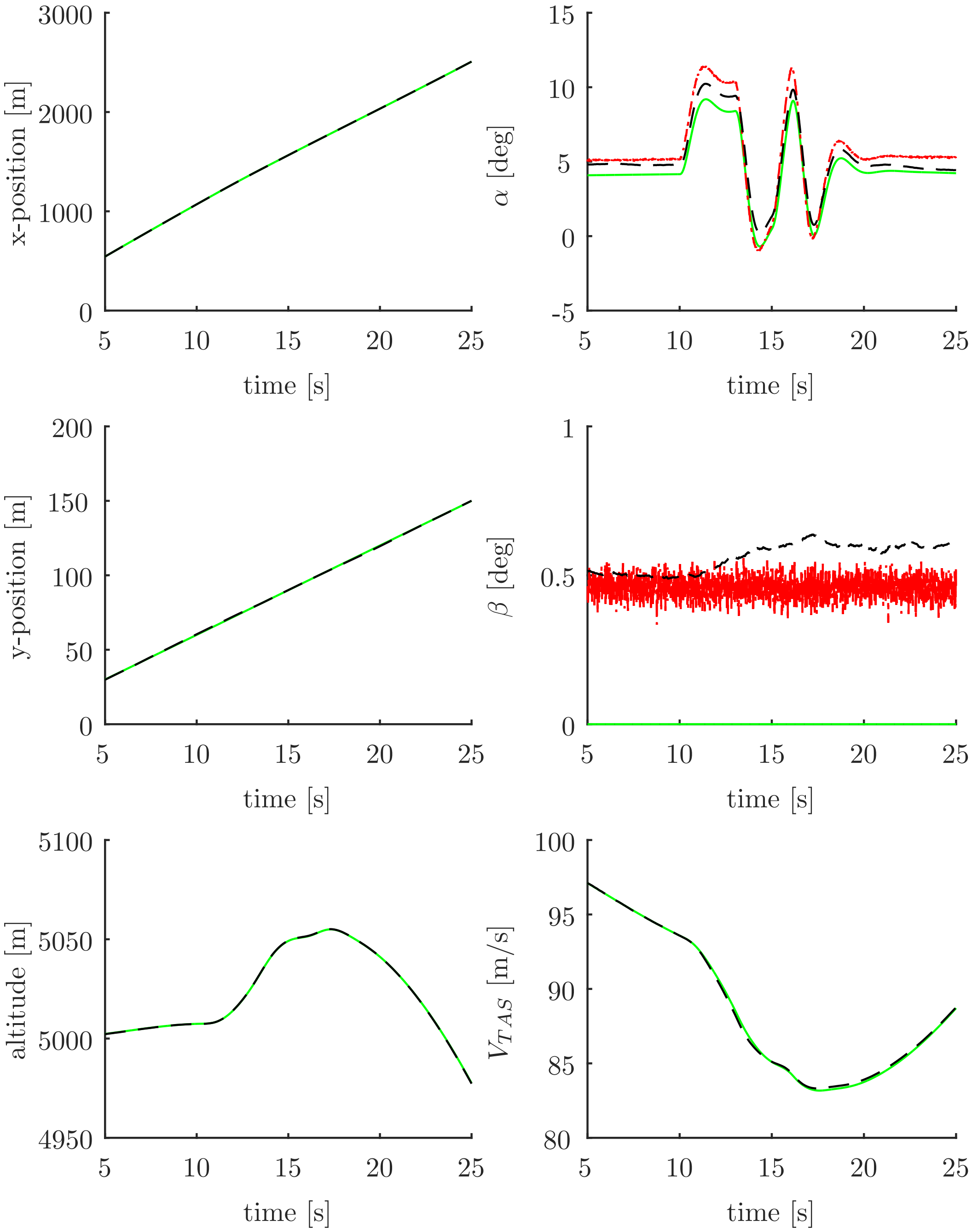

Figure 3-10: The position and air data, filtered by an UKF, using the full state: $\in \mathbb{R}^{22}$. With the true value (green-solid), the estimated value (black-dashed) and the measured value (red-dashed/dotted). With only a 3211 input on the elevator.

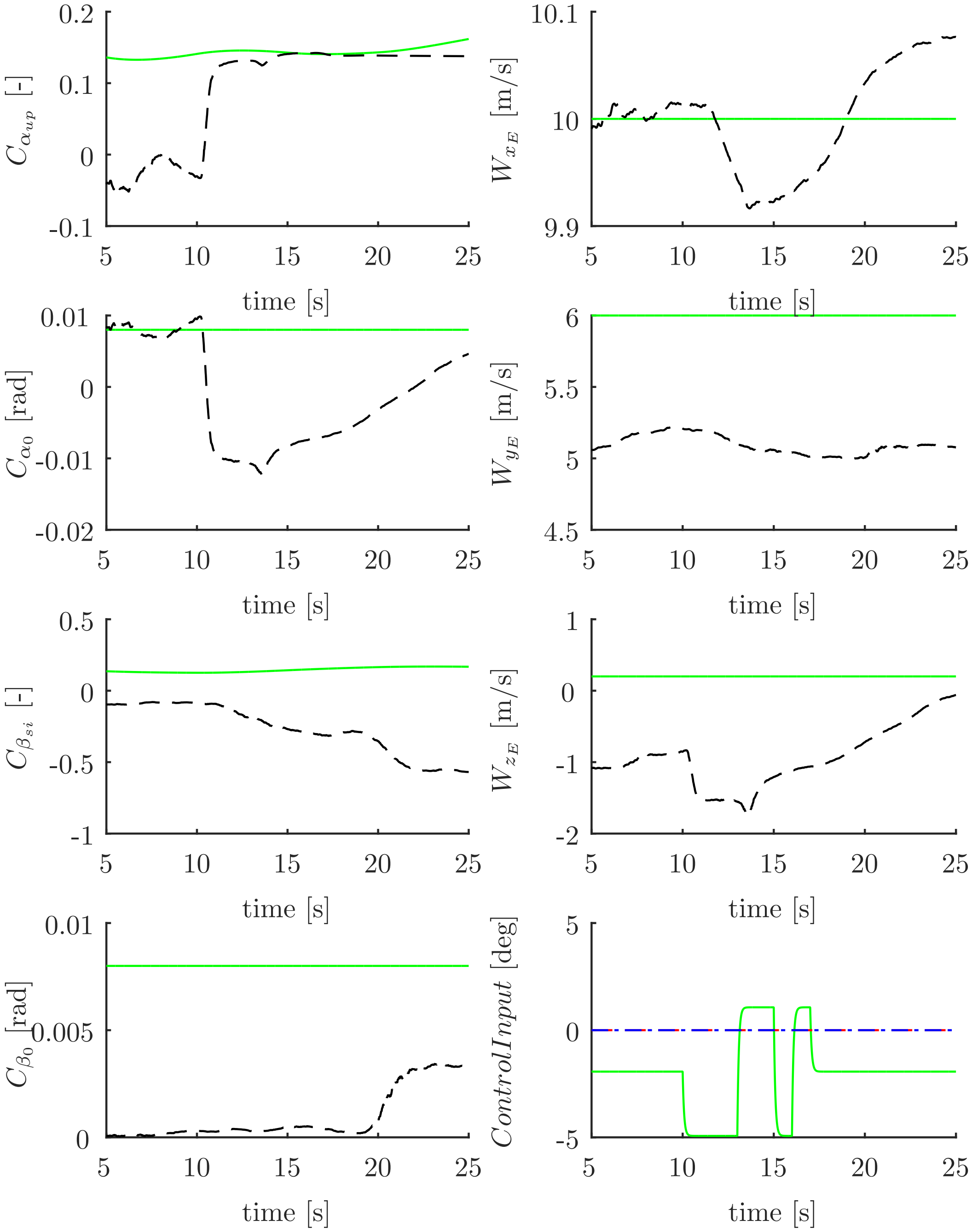

Figure 3-11: The coefficients influencing air flow measurement and wind velocities, using the full state: $\in \mathbb{R}^{22}$. With the true value (green-solid) and the estimated value (black-dashed). With only a 3211 input on the elevator. For the control input on the bottom right plot: δ_e: green-solid, δ_a: red-dashed, δ_r: blue-dashed/dotted

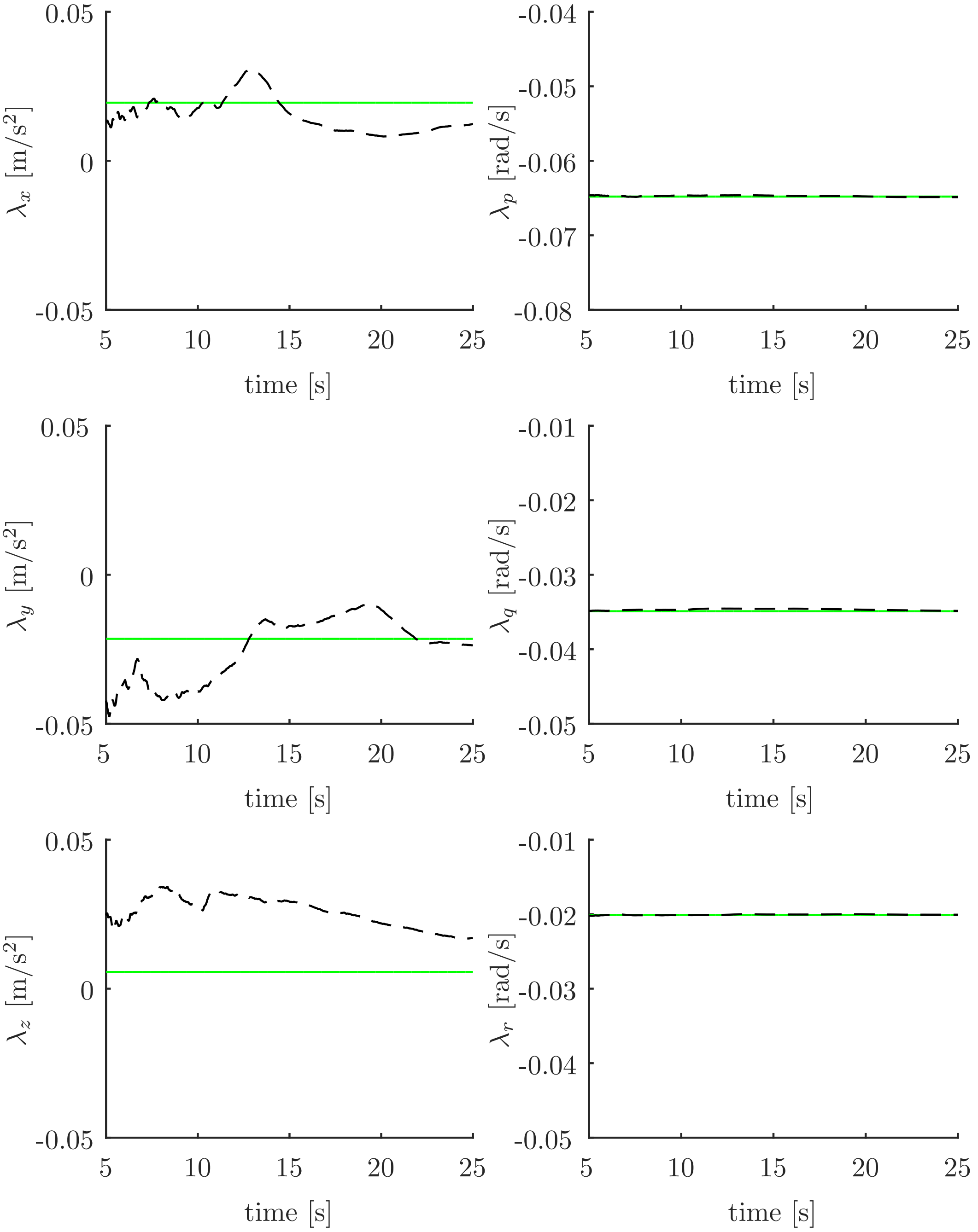

Figure 3-12: The IMU biases, filtered by an UKF, using the full state: $\in \mathbb{R}^{22}$. With the true value (green-solid) and the estimated value (black-dashed). With only a 3211 input on the elevator.

Furthermore the IEKF performs a linearization step, where the Jacobians: F_x, F_u and H_x need to be calculated. This linearization step essentially transforms the system to the well known linear state space system:

$$\dot{\boldsymbol{x}}(t) = A\boldsymbol{x} + B\boldsymbol{u} \tag{3-69}$$

$$\boldsymbol{y}(t) = C\boldsymbol{x} + D\boldsymbol{u} \tag{3-70}$$

Where in this case $D = 0$ and the A-, B- and C-matrices are: F_x, F_u and H_x respectively. Using the Kalman observability rank on this linear system:

$$\mathcal{O} = \begin{bmatrix} C \\ CA \\ CA^2 \\ \vdots \\ CA^{n-1} \end{bmatrix} \tag{3-71}$$

It can be found that the state, as described by Eq. 3-63, even without the vertical wind component is not observable when linearized. After some investigation it was found that also the terms: C_{α_0}, $C_{\beta si}$ and C_{β_0}, where not observable. It is however not necessary for the linearization to be observable in an IEKF, as long as the estimates are sufficiently close to the true state (Song & Grizzle, 1992). Nevertheless a simulation has been done where the linearization is observable as well. To make the linearization step observable however the initial state needed to be changed, the main reason was that the body velocity in vertical direction (w) was not allowed to be zero. Therefore the new initial condition, without the terms: W_{z_E}, C_{α_0}, $C_{\beta si}$ and C_{β_0} is as follows:

$$\begin{aligned} \boldsymbol{x}_0 = [0 \quad 0 \quad -5000 \quad 100 \quad 0 \quad 1 \quad 0 \quad 0.6 \quad 0 \quad 0 \quad 0.2 \\ 0 \quad 0 \quad 0 \quad 0 \quad 0 \quad 0 \quad 0]^T \end{aligned} \tag{3-72}$$

Where the state is described by:

$$\begin{aligned} \boldsymbol{x} = \big[x \quad y \quad z \quad u \quad v \quad w \quad \phi \quad \theta \quad \psi \quad W_{x_E} \quad W_{y_E} \quad C_{\alpha_{up}} \\ \lambda_x \quad \lambda_y \quad \lambda_z \quad \lambda_p \quad \lambda_q \quad \lambda_r\big]^T \end{aligned} \tag{3-73}$$

In Figure 3-13 the results are given for three different states: The original state as described by Eq. 3-63, the original state without W_{z_E} and the state as described by Eq. 3-73. Each were filtered with an UKF, which does not have the limitation of linearization. The comparison between the three different kinematic models is done for three types of input maneuvers. One were both elevator and rudder are excited, one were only the aileron is excited and one were only the elevator is excited.

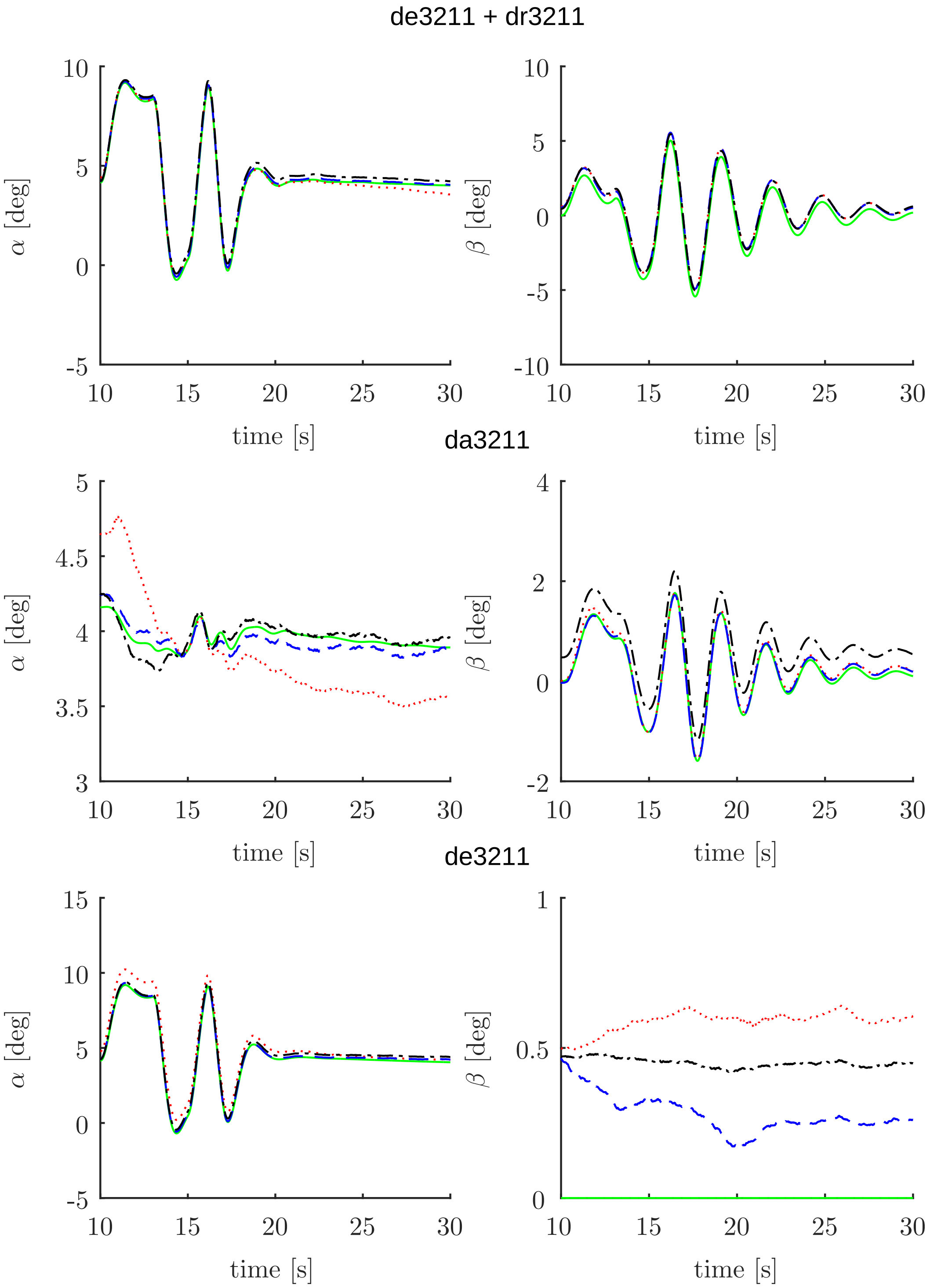

Figure 3-13: Comparison between three different kinematic models. With the true value (green-solid), full state (red-dotted), state w/o W_{z_E} (blue-dashed) and state w/o: W_{z_E}, C_{α_0} $C_{\beta_{si}}$ and C_{β_0} (black-dashed/dotted). For three different types of control input: top (de3211 + dr3211), middle (da3211), bottom (de3211). All results are obtained by DASMAT

The first interesting thing is that using the full state seems not so robust compared to the full state minus the vertical wind component. As shown in Figure 3-13 the full state converges to the correct Angle of Attack (AoA) and Angle of Side Slip (AoSS) when applying both a longitudinal and lateral input simultaneously. When only applying either a longitudinal or a lateral input, e.g. only an 3-2-1-1 maneuver on the elevator the estimate for both the AoA and AoSS are far for optimal. As stated before vertical wind component is often very small and therefore can be neglected. This result is also shown in Figure 3-13 as the blue-dashed line. This model seems to give the overall best performance. Lastly the results for the state as given in Eq. 3-73 is given as the black-bashed/dotted line. When applying a 3-2-1-1 input on the aileron however, the estimate is not very close to the true state, due to the missing parameters $C_{\beta_{si}}$ and C_{β_0}.

The final system, i.e. dynamical model and observation model that will be used for the rest of this thesis will be as follows:

$$\begin{aligned}\dot{\boldsymbol{x}} &= f\left(\boldsymbol{x}\left(t\right), \boldsymbol{u_m}\left(t\right), \boldsymbol{w}\left(t\right)\right)\\ &= \begin{bmatrix} \left[u\cos\theta + \left(v\sin\phi + w\cos\phi\right)\sin\theta\right]\cos\psi - \left(v\cos\phi - w\sin\phi\right)\sin\psi + W_{x_E} \\ \left[u\cos\theta + \left(v\sin\phi + w\cos\phi\right)\sin\theta\right]\sin\psi + \left(v\cos\phi - w\sin\phi\right)\cos\psi + W_{y_E} \\ -u\sin\theta + \left(v\sin\phi + w\cos\phi\right)\cos\theta \\ \left(A_x - \lambda_x\right) - g\sin\theta - \left(q - \lambda_q\right)w + \left(r - \lambda_r\right)v \\ \left(A_y - \lambda_y\right) + g\cos\theta\sin\phi - \left(r - \lambda_r\right)u + \left(p - \lambda_p\right)w \\ \left(A_z - \lambda_z\right) + g\cos\theta\cos\phi - \left(p - \lambda_p\right)v + \left(q - \lambda_q\right)u \\ \left(p - \lambda_p\right) + \left(q - \lambda_q\right)\sin\phi\tan\theta + \left(r - \lambda_r\right)\cos\phi\tan\theta \\ \left(q - \lambda_q\right)\cos\phi - \left(r - \lambda_r\right)\sin\phi \\ \left(q - \lambda_q\right)\frac{\sin\phi}{\cos\theta} + \left(r - \lambda_r\right)\frac{\cos\phi}{\cos\theta} \\ \mathbf{0}_{12\times1} \end{bmatrix}\end{aligned} \tag{3-74}$$

With:

$$\begin{aligned}\boldsymbol{x} = \big[&x \quad y \quad z \quad u \quad v \quad w \quad \phi \quad \theta \quad \psi \quad W_{x_E} \quad W_{y_E} \quad C_{\alpha_{up}} \quad C_{\alpha_0} \\ &C_{\beta_{si}} \quad C_{\beta_0} \quad \lambda_x \quad \lambda_y \quad \lambda_z \quad \lambda_p \quad \lambda_q \quad \lambda_r\big]^T\end{aligned} \tag{3-75}$$

And the observation model:

$$
\begin{aligned}
\boldsymbol{y} \quad &= h\left(\boldsymbol{x}\left(t\right), \boldsymbol{u_m}\left(t\right), \boldsymbol{v}\left(t\right)\right) \\
\begin{bmatrix} x_{gps} \\ y_{gps} \\ h_{DADC} \\ \dot{h}_{DADC} \\ \phi_{AHRS} \\ \theta_{AHRS} \\ \psi_{AHRS} \\ V_{TAS} \\ \alpha_v \\ \beta_v \end{bmatrix} &= \begin{bmatrix} x \\ y \\ -z \\ u\sin\theta - \left(v\sin\phi + w\cos\phi\right)\cos\theta \\ \phi \\ \theta \\ \psi \\ \sqrt{u^2+v^2+w^2} \\ \left(1+C_{\alpha_{up}}\right)\arctan\left(\frac{w}{u}\right) + \frac{(q-\lambda_q)x_{v_\alpha}}{V_{TAS}} + C_{\alpha_0} \\ \left(1+C_{\beta_{si}}\right)\arctan\left(\frac{v}{\sqrt{u^2+w^2}}\right) - \frac{(r-\lambda_r)x_{v_\beta}}{V_{TAS}} + \frac{(p-\lambda_p)z_{v_\beta}}{V_{TAS}} + C_{\beta_0} \end{bmatrix}
\end{aligned}
\tag{3-76}
$$

3-6 Simulation Model

In this section the model, which is used for simulations run, will be explained. The aircraft simulation is TU Delft's in house Cessna Citation I model, also known as DASMAT. On top of that a sensor model is created to match reality more closely. This includes adding white noise signals, different sampling rates,but also sensor biases and offsets and misalignments of the IMU.

3-6-1 Sensor noise & bias

The first step in creating a sensor model is to add white noise signals to the measurements. To create an as realistic as possible sensor model real life flight data, including a engine-off static test are used. This allowed to estimate standard deviations of the measurement signals and IMU biases. The results are given in Appendix III. For the GPS measurements a random offset between -10 and +10 meters is added, since GPS measurements are not only noisy, but also have a certain accuracy, better known as Dilution of Precision (DOP).

3-6-2 Sampling rates

Next to that real life measurement always contain noise, the measurements are also not infinitely fast. This effect is also modeled in the sensor model. Again the sample rates of the real life measurements are used to create an as realistic as possible sensor model. The sampling rates of the true measurements are given in Table 3-2.

3-6-3 IMU offset and misalignment

The measurements of the inertial measurement unit in a simulation are measured in the center of gravity and the axes are perfectly aligned with the body axes. In real life however this will never be the case. Not only does the c.g. in an aircraft shift during flight, the IMU will also

Table 3-2: Sampling frequencies of the measurements

Measurement	**Sampling frequency [hz]**
x	1
y	1
h	16.67
$\dot{h}$	16.67
ϕ	50
θ	50
ψ	10
V_{TAS}	16.67
α	1000
β	1000
p	50
q	50
r	50
A_x	50
A_y	50
A_z	50
δ_e	100
δ_a	100
δ_r	100

never be perfectly aligned with the body axes. These two effects are modeled as well in the sensor model.

The IMU offset is given by Eq. 3-61. The offsets that are used in the simulation model are random normally distributed values. The value for dx is somewhere between 5.3 and 5.9 meters, for dy between -0.2 and 0.2 meters and for dz between 0.8 and 1.2 meters. The main reason that the IMU correction is so large in x-direction is due the fact that the IMU is positioned beneath the floor of the nose baggage compartment, which is in front of the front pressure bulkhead as shown in Figure 3-4.

The measurements from the IMU are done by the AHRS of the Cessna Citation II. This AHRS is the AHS-3000 by Rockwell Collins. The primary function of this AHRS is to provide the attitude of the aircraft. Since this system is part of the FTIS of the Cessna Citation II it is expected that the IMU is relatively well aligned. Therefore in the sensor model an offset of only 0.1 degrees in all directions is used. This is done using a standard axes transformation as described by Eq. 3-77.

$$\mathbb{T} = \begin{bmatrix} \cos(\theta)\cos(\psi) & \cos(\theta)\sin(\psi) & -\sin(\theta) \\ \sin(\phi)\sin(\theta)\cos(\psi) - \cos(\phi)\sin(\psi) & \sin(\phi)\sin(\theta)\sin(\psi) + \cos(\phi)\cos(\psi) & \sin(\phi)\cos(\theta) \\ \cos(\phi)\sin(\theta)\cos(\psi) + \sin(\phi)\sin(\psi) & \cos(\phi)\sin(\theta)\sin(\psi) - \sin(\phi)\cos(\psi) & \cos(\phi)\cos(\theta) \end{bmatrix} \tag{3-77}$$

3-6-4 Higher fidelity AoA and AoSS measurements

Lastly the measurement of the angle of attack and angle of side slip are increased to a higher fidelity. As show in Eqs. 3-59 and 3-60 the AoA and AoSS are influenced by an upwash $\left(C_{\alpha_{up}}\right)$ and sidewash $(C_{\beta_{si}})$ component respectively. On top of that an unknown wind component is added to both the AoA and AoSS, i.e. (C_{α_0}) and (C_{β_0}). These components are added to the sensor model. Both unknown wind component are -0.008 rad ($\approx -0.46°$). The upwash and sidewash component are randomly created signals between 0.1 and 0.2, with a sample time of five seconds and filtered through a low pass filter with a natural frequency of 0.03 Hz. A typical example of such a signal is shown in Figure 3-14.

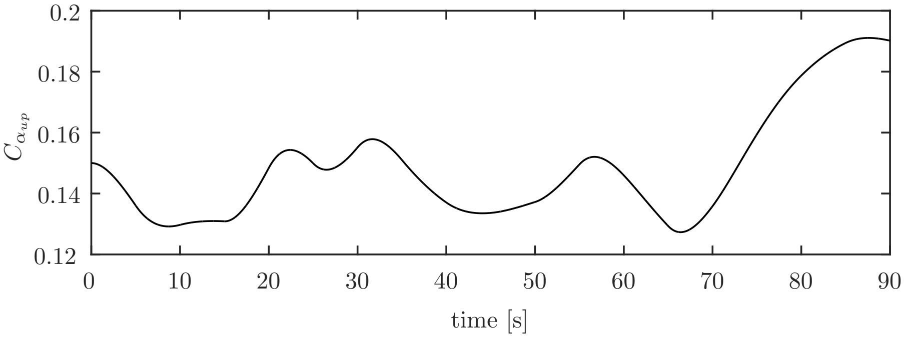

Figure 3-14: Typical value of $C_{\alpha_{up}}$ during a simulation run

Next to that the pitch, roll and yaw rate effects are also included. The values for x_{v_α}, x_{v_β} and z_{v_β} are 8, 8 and 1 meters respectively.

3-7 FPR Results

With the sensor model implemented in Simulink a simulation run is done to test different types of Kalman filters and smoothers. These filters are:

1. Iterated Extended Kalman Filter (IEKF)
2. Unscented Kalman Filter (UKF)
3. Iterated extended Kalman filter with a Rauch-Tung-Striebel smoother (IERTSS)
4. Unscented Kalman Smoother with Euler discretization approximation (UKS)
5. Unscented Kalman filter with a Rauch-Tung-Striebel smoother (URTSS)

The simulation was done for a 3-2-1-1 input on the elevator. In total 100 runs where used to get an as good as possible estimate of the filter performances. The initial results are given in Figures 3-15 and 3-16. The results are described in terms of the root-mean squared error (RMSE), from the filtered value minus the true value.

The first noticeable thing is that the smoothers are not necessarily better than the filters. Although for some states, such as the body-velocity u the smoothers perform better, in other crucial variables they perform less. For example in Figure 3-16 the estimates of the angle of attack is better by a filter. As can be seen in Figure 3-16 as well, the measurement of the side slip angle is rather bad. This can be explained by the fact that the excitation was a longitudinal excitation and not a lateral. Thus the lateral components are better estimated by smoothers, when there is no excitation in lateral direction.

Furthermore it can be seen that the angle of attack measurement is best estimated by an IEKF. However when a value of 0.008 for C_{α_0} and C_{β_0} were used instead of -0.008, the UKF gave a better estimate. Thus although it looks as if the IEKF performs better, this is not necessarily true. In fact for different conditions it might well be that the UKF performs better. Therefore there is no clear distinction whether the IEKF or UKF is better.

Although not proven, during user experience the UKF was more robust than the IEKF. Whereas with the IEKF the initial state needed to be relatively close to the true state for the UKF this was not the case. The same counts for the initial covariance, with the IEKF it was more difficult to tune the initial covariance than with the UKF.

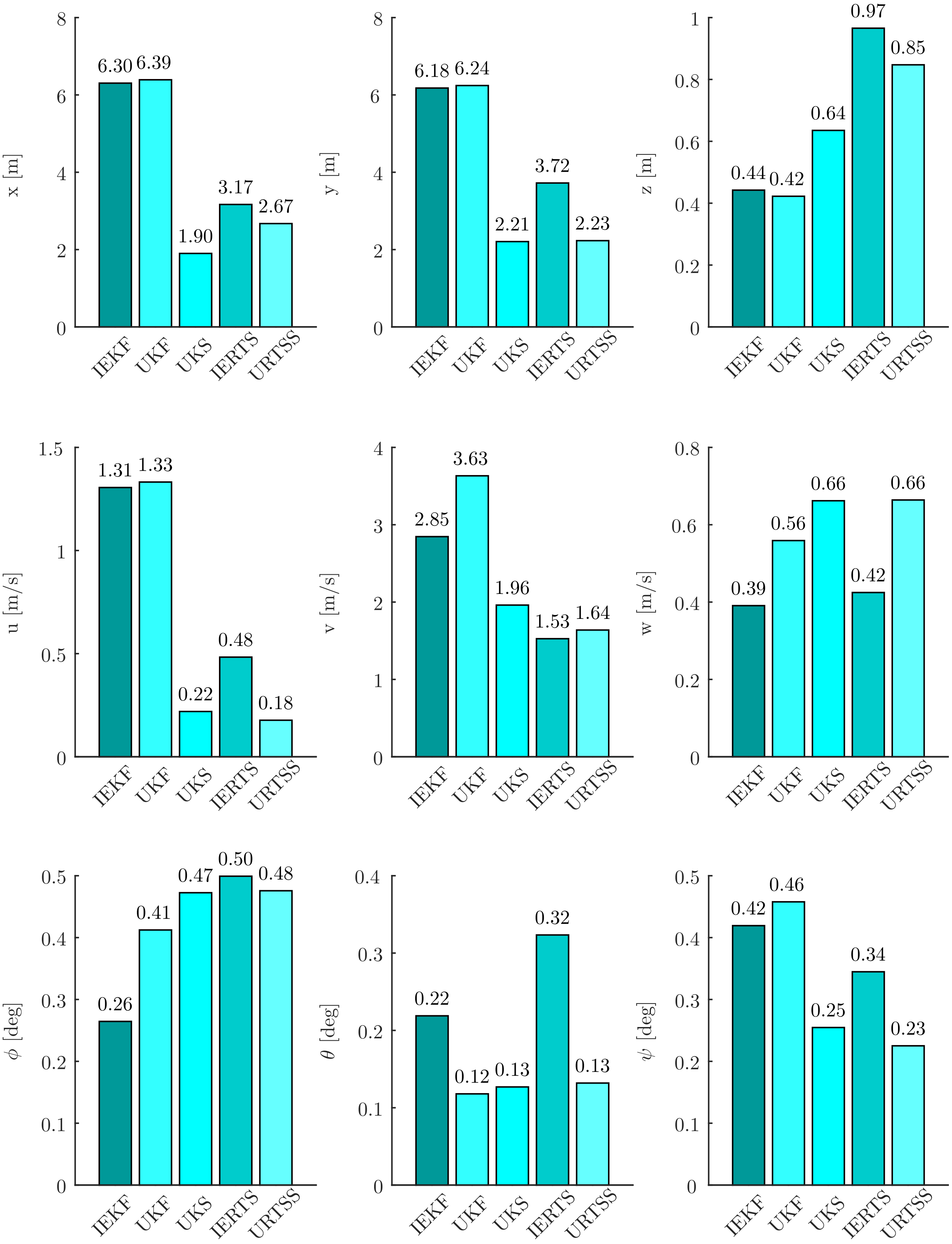

Figure 3-15: Root-mean square errors for the aircraft state, without a correction for the IMU measurements.

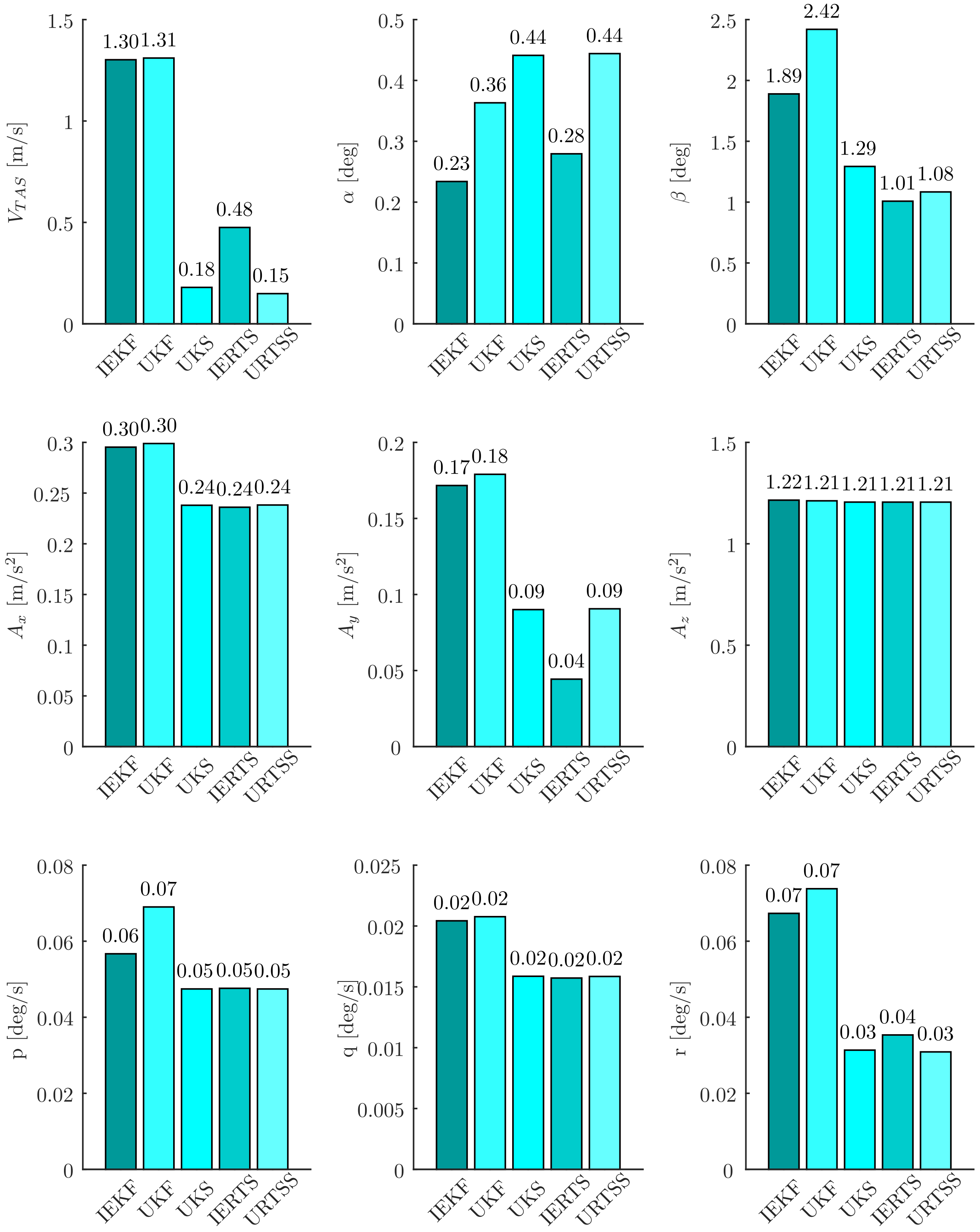

Figure 3-16: Root-mean square errors for the aircraft measurements, without a correction for the IMU measurements.

Something that was modeled in the sensor model was that the measurements of the IMU were not in the center of gravity. As can be seen in Figure 3-16 the error, especially in A_z is quite high. To reduce this value it has been investigated whether it is useful to first apply a correction for the IMU measurement. To do so first the rotational rates were smoothed with third order Butterworth low pass filter, with a cut of frequency at 3 Hz. Then the rates were numerically differentiated to obtain the rotational accelerations. Then Eq. 3-61 was used to apply a correction for the IMU measurements. The results are given in Figures 3-18 and 3-19. As can be seen the estimates for A_x and A_z have drastically improved. Not only that but the angle of attack estimate improves as well. It can thus be concluded that it is useful to first correct for the IMU position w.r.t. the center of gravity, in case the IMU is not placed at the center of gravity of course.

Furthermore the average run time of each of the filters and smoother was saved. The results are shown in Figure 3-17. As can be seen the IEKF runs a lot faster than the UKF. With the UKF there are: $2N + 1$ sets of sigma points, which needs to be propagated through the nonlinear dynamic equations. Where N is the dimension of the augmented state which, for this simulation, is 39 (= 21 states + 6 + input noise + 12 + output noise). So in total 79 sets of sigma points has to be propagated through the system, which is the most time consuming part of the UKF. Furthermore as shown in Figure 3-17 the run time for the Unscented Kalman Smoother (UKS) is approximately twice as long, which makes sense since it is actually twice an UKF, one running forward in time and the other backwards.

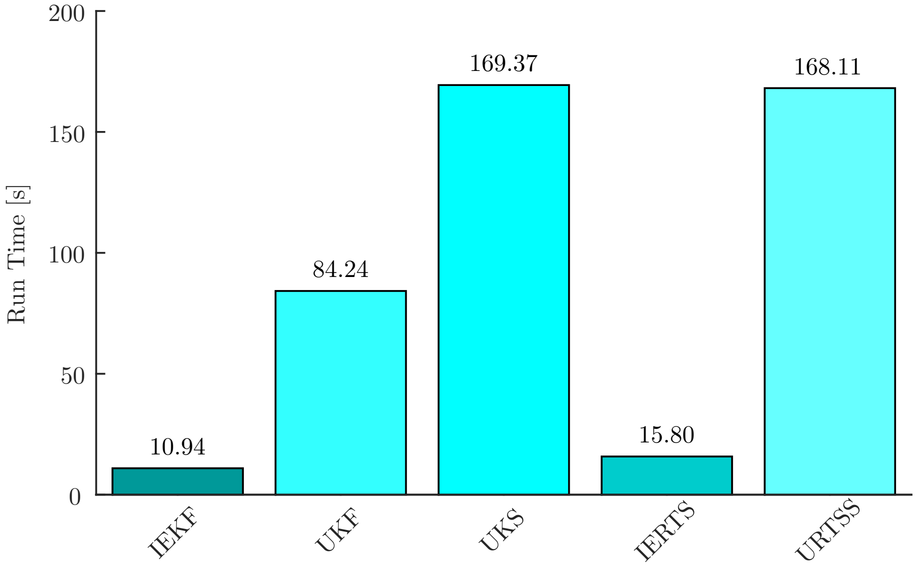

Figure 3-17: Average run time of each of the filters and smoothers, taken from 100 realizations

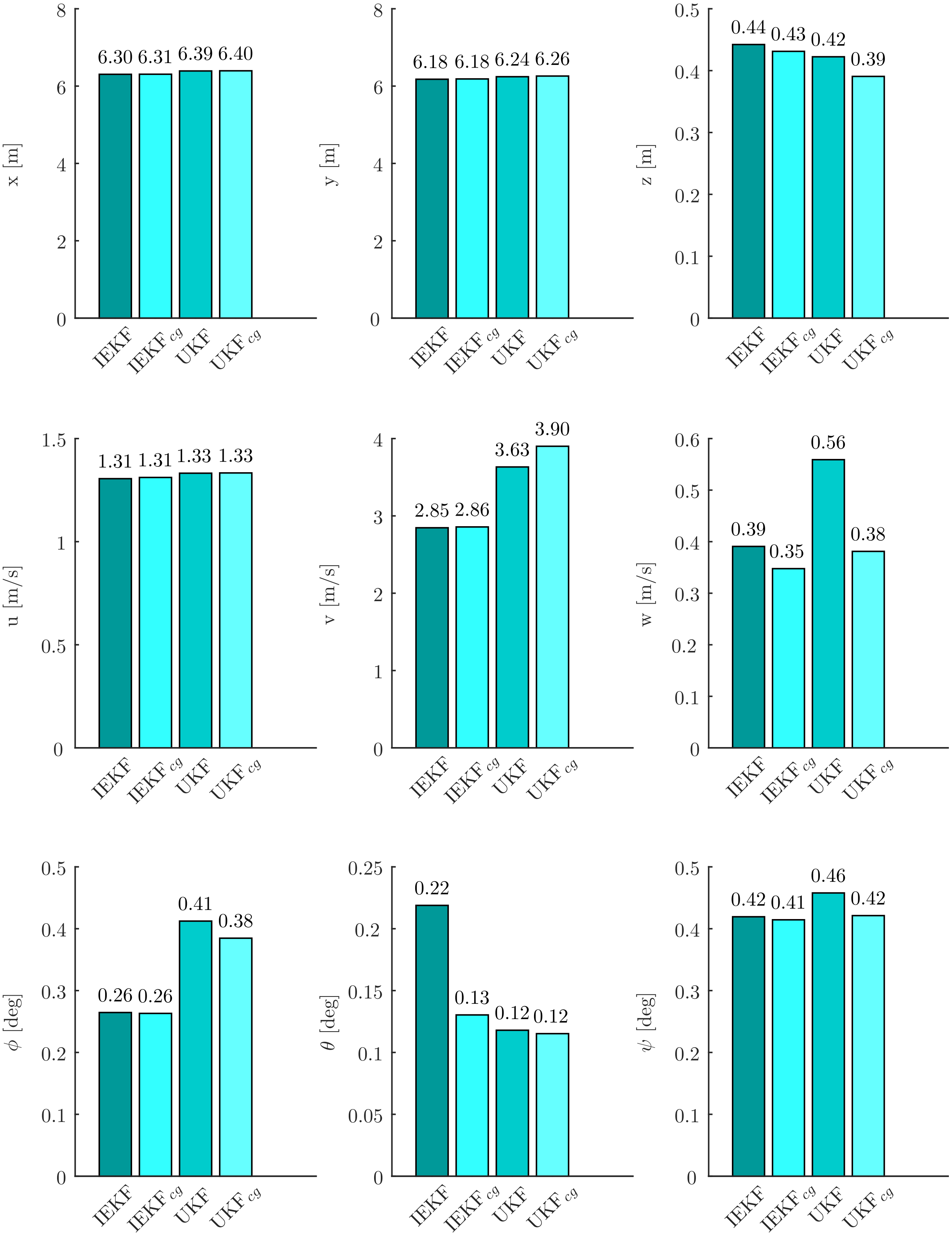

Figure 3-18: Root-mean square errors for the aircraft state. Subscript cg indicates that the IMU measurements were first corrected.

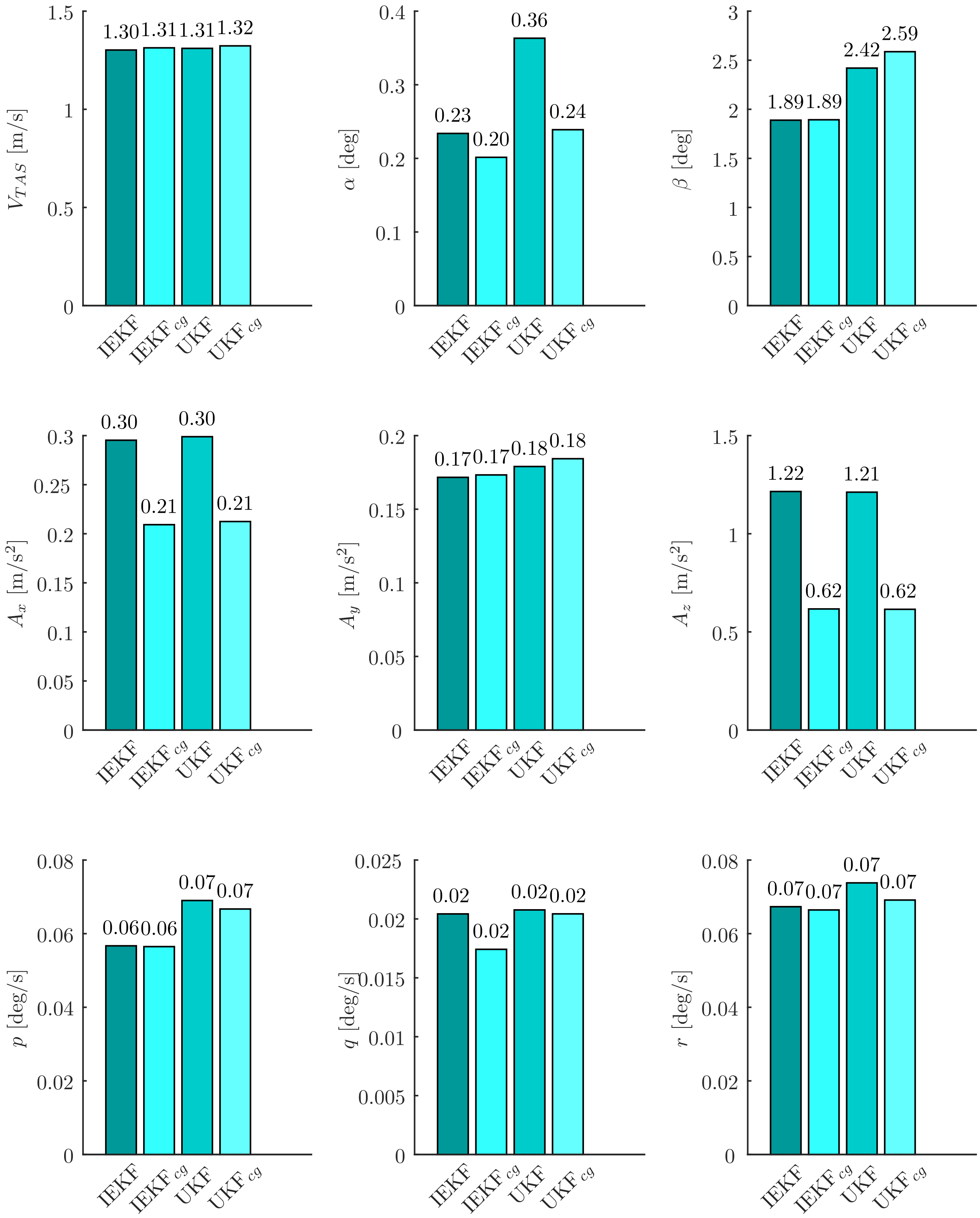

Figure 3-19: Root-mean square errors for the aircraft measurements. Subscript cg indicates that the IMU measurements were first corrected.

3-8 Conclusion

First and foremost it can be concluded that the performance between the UKF and the IEKF are not significantly different. The IEKF runs approximately eight times faster than the UKF. On the other hand, with the UKF the choice of the initial condition and covariance matrix is less crucial. Also the choice in terms of the process and measurement noise covariance matrices is less crucial with the UKF. Another advantage of the UKF is that it does not rely on linearization, and thus there is no need for calculating the Jacobians.

The smoother performed worse in terms of the "vertical" variables, such as w and α. This is most likely caused due to the upwash component in the angle of attack measured and errors in the IMU measurements, such as an offset with respect to the center of gravity. Therefore during the rest of this thesis only the Kalman filters are considered.

Since the measurements of the linear accelerations are not performed in the center of gravity, but instead beneath the floor of the nose baggage compartment, the measured accelerations are not the true acceleration of the aircraft. The bias terms in the linear accelerations also act as a garbage term, and thus effects due to an offset with respect to the center of gravity are partially compensated in this term. The IMU measurement can also be corrected, such that the accelerations are transformed as if the measurements are made in the center of gravity. To do so, the rotational accelerations are needed, which can be obtained from numerically differentiating the rotational rates, after the rates have been pre-filtered by a low-pass filter. This method neglects the bias term in the rotational rates, however these are so small, that this assumption is valid. It was found that this correction greatly improved the results and thus is deemed necessary.

Lastly it was found that the vertical wind component (W_{z_E}) cannot be estimated. In relatively calm weather however this component is relatively small, in the order of 0.1 to 0.2 m/s (Mulder et al., 1994). Thus although this assumption causes an error in the angle of attack, this effect should be relatively small.

Chapter 4

Parameter Estimation

The second step in the two-step method involves parameter estimation. These parameters are used to create look-up tables which are used to calculate the dimensionless force and moment coefficients. For the longitudinal case the following set of equations are used:

$$C_L = C_{L_0} + C_{L_\alpha} \left\{ \frac{1+\sqrt{X}}{2} \right\}^2 \alpha + C_{L_q} \frac{q\bar{c}}{V} + C_{L_{\delta_e}} \delta_e \tag{4-1}$$

$$C_D = C_{D_0} + \frac{1}{e\pi\Lambda} C_L^2 + \frac{\partial C_D}{\partial X} (1 - X) \tag{4-2}$$

$$C_m = C_{m_0} + C_{m_\alpha} \alpha + C_{m_q} \frac{q\bar{c}}{V} + C_{m_{\delta_e}} \delta_e + \frac{\partial C_m}{\partial X} (1 - X) \tag{4-3}$$

Where the flow separation point X is calculated as follows:

$$\tau_1 \frac{dX}{dt} + X = \frac{1}{2} \left\{ 1 - \tanh \left(a_1 \left(\alpha - \tau_2 \dot{\alpha} - \alpha^* \right) \right) \right\} \tag{4-4}$$

To simplify Eq. 4-4 the parameter τ_1 can be set equal to zero. This parameter is also only measurable when highly dynamic maneuvers are applied in the flow separated flight regime. Due to the tangent hyperbolic in the calculation of the flow separation point linear optimization techniques are useless in this situation. Therefore in this section some nonlinear optimization algorithms will be summarized. The nonlinear optimization algorithms that will be discussed in this chapter are: Gauss-Newton (Hartley, 1961), Levenberg-Marquardt (Marquardt, 1963) and Nelder-Mead (Nelder & Mead, 1965).

4-1 Gauss-Newton

The essential step in nonlinear parameter estimation is the cost function. In this case the cost function minimizes the squared error. Therefore this optimization algorithm can also be seen as a nonlinear least squares estimation. The cost function will be defined as:

$$S\left(\beta\right) = \sum_{i=1}^{m} \left[y_i - f\left(x_i, \beta\right)\right]^2 \tag{4-5}$$

Where β are the parameters to be estimated. The Gauss-Newton method is an iterative optimization algorithm, thus using an iterative method to obtain a new set of parameters every time. The new estimate for the set of parameters is given by: $\beta^{(k+1)} = \beta^{(k)} + \delta$. To determine the value for δ the function: $f\left(x_i, \beta + \delta\right)$ is approximated by its linearization:

$$f\left(x_i, \beta + \delta\right) \approx f\left(x_i, \beta\right) + J_i \delta \tag{4-6}$$

Where,

$$J_i = \frac{\partial f\left(x_i, \beta\right)}{\partial \beta} \tag{4-7}$$

Using the first order approximation in the cost function, the following is obtained:

$$S\left(\beta + \delta\right) \approx \sum_{i=1}^{m} \left[y_i - f\left(x_i, \beta\right) - J_i \delta\right]^2 \tag{4-8}$$

Taking the derivative with respect to δ and setting it equal to zero yields:

$$\left(J^T J\right) \delta = J^T \left[y - f\left(\beta\right)\right] \tag{4-9}$$

Since the new set of parameters is given by: $\beta^{(k+1)} = \beta^{(k)} + \delta$, and using δ as given in Eq. 4-9, the whole Gauss-Newton iterative optimization algorithm can be expressed using one equation:

$$\beta^{(k+1)} = \beta^{(k)} + \left(J^T J\right)^{-1} J^T \left[y - f\left(\beta\right)\right] \tag{4-10}$$

The iteration can be stopped when either the cost function is not decreasing anymore or the set of parameters hardly changes anymore.

4-2 Levenberg-Marquardt

The Levenberg-Marquardt algorithm is essentially a modification to the Gauss-Newton optimization algorithm. The calculation δ, as given in Eq. 4-9, was modified to include a damping term λI, which is Levenberg's contribution:

$$\left(J^T J + \lambda I\right) \delta = J^T \left[y - f\left(\beta\right)\right] \tag{4-11}$$

When the value of λ is low the algorithm tends towards the Gauss-Newton optimization algorithm. When the value of λ is increased the algorithm behaves more as the gradient descent algorithm. Marquardt introduced a scaling component, based on linear least squares problems. This scaling component is introduced by replacing λI with $\lambda \mathrm{diag}\left(J^T J\right)$, and improves the overall convergence of the algorithm. The calculation of δ then becomes:

$$\left(J^T J + \lambda \ \mathrm{diag}\left(J^T J\right)\right) \delta = J^T \left[y - f\left(\beta\right)\right] \tag{4-12}$$

The Levenberg-Marquardt algorithm can be expressed using one equation as well:

$$\beta^{(k+1)} = \beta^{(k)} + \left(J^T J + \lambda \ \mathrm{diag}\left(J^T J\right)\right)^{-1} J^T \left[y - f\left(\beta\right)\right] \tag{4-13}$$

The only question left unanswered is the choice of the value of λ. Marquardt proposed to set the initial value to: $\lambda^{(0)} = 10^{-2}$. Then the following set of rules is applied, where $v > 1$:

1. If $S^{(k+1)}\left(\lambda^{(k)}/v\right) \leq S^{(k)}$, let $\lambda^{(k+1)} = \lambda^{(k)}/v$.
2. If $S^{(k+1)}\left(\lambda^{(k)}/v\right) > S^{(k)}$ and $S^{(k+1)}\left(\lambda^{(k)}\right) < S^{(k)}$, let $\lambda^{(k+1)} = \lambda^{(k)}$.
3. If $S^{(k+1)}\left(\lambda^{(k)}/v\right) > S^{(k)}$ and $S^{(k+1)}\left(\lambda^{(k)}\right) > S^{(k)}$, increase λ by successive multiplication by v until for some smallest w: $S^{(k+1)}\left(\lambda^{(k)} v^w\right) \leq S^{(k)}$. Then let $\lambda^{(k+1)} = \lambda^{(k)} v^w$

4-3 Nelder-Mead

Although there are a lot more nonlinear optimization techniques the Nelder-Mead simplex method will be the last to be discussed. Although the original method was developed by Nelder and Mead, the algorithm discussed here is based on (Lagarias, Reeds, Wright, & Wright, 1998). First lets define the cost function as in Eq. 4-5. Then take $n + 1$ test points, where n is the amount of unknown parameters, thus in case of Eq. 4-1 the number n would be equal to eight. Then the Nelder-Mead algorithm works as follows:

1. **Order** the total number of vertices to satisfy:

$$S\left(\beta_1\right) \leq S\left(\beta_2\right) \leq \cdots \leq S\left(\beta_{n+1}\right)$$

2. Calculate the **centroid** of all the vertices except for β_{n+1}

$$\bar{\beta} = \sum_{i=1}^{n} \beta_i / n$$

3. Compute the **reflection** point β_r:

$$\beta_r = \bar{\beta} + \rho \left(\bar{\beta} - \beta_{n+1} \right)$$

   If $S(\beta_1) \leq S(\beta_r) < S(\beta_n)$, accept the reflected point and replace the worst vertex with the reflected point:

$$\beta_{n+1} = \beta_r$$

   Then terminate the iteration. If the cost function at the reflected point is not between the best and the second worst point, then continue the algorithm.

4. If $S(\beta_r) < S(\beta_1)$, then calculate the **expansion** point:

$$\beta_e = \beta_r + \chi \left(\beta_r - \bar{\beta} \right)$$

   If $S(\beta_e) < S(\beta_r)$ then accept β_e and replace it with β_{n+1}. Else accept β_r and replace it with β_{n+1}.

5. If $S(\beta_r) \geq S(\beta_n)$ then **contract**:

   (a) If $S(\beta_n) \leq S(\beta_r) < S(\beta_{n+1})$ then perform an **outside** contraction:

$$\beta_{co} = \bar{\beta} - \gamma \left(\beta_r - \bar{\beta} \right)$$

   If $S(\beta_{co}) \leq S(\beta_r)$ then accept β_{co} and replace it with β_{n+1} then stop the iteration, else go to step 6.

   (b) If $S(\beta_r) \geq S(\beta_{n+1})$ then perform an **inside** contraction:

$$\beta_{ci} = \bar{\beta} - \gamma \left(\bar{\beta} - \beta_{n+1} \right)$$

   If $S(\beta_{ci}) < S(\beta_{n+1})$, accept β_{ci} and stop the iteration, else go to step 6.

6. Perform a **shrink** step, i.e. replace all but the best vertices:

$$\beta_i = \beta_1 + \sigma \left(\beta_i - \beta_1 \right), \quad \text{for} i = 2, ..., n+1$$

The Nelder-Mead optimization algorithm can be tuned using four coefficients: *reflection* (ρ), *expansion* (χ), *contraction* (γ), *shrinkage* (σ). These parameters should satisfy:

$$\rho > 0, \quad \chi > 1, \quad 0 < \gamma < 1, \quad \text{and} \quad 0 < \sigma < 1$$

The standard choices for the Nelder-Mead algorithm are (Lagarias et al., 1998):

$$\rho = 1, \quad \chi = 2, \quad \gamma = \frac{1}{2}, \quad \text{and} \quad \sigma = \frac{1}{2}$$

4-4 Conclusion

Although there is not such an extensive research done in the parameter estimation as for the flight path reconstruction, it is still possible to draw a few conclusions. Note however that these conclusions are based on user experience.

Three different optimization methods were compared: Gauss-Newton, Levenberg-Marquardt and Nelder-Mead. It was found that the Nelder-Mead optimization algorithm was the most robust. This is most likely due to the fact that no matrix inversion is needed. It was also found however that the Nelder-Mead algorithm mostly led to sub-optimal parameter estimations. This is caused due to the relatively large amount of optima. The Nelder-Mead algorithm will always tend to the closest optimum to the initial condition.

The Gauss-Newton and Levenberg-Marquardt algorithms on the other hand were able to find the global optimum. One problem that occurred rather often however are the numerical instabilities due to the inversion of the Jacobian. This inversion was often (close to) singular. This problem was overcome by running the algorithm multiple times, e.g. a thousand times. Then after that all the solutions for which numerical instabilities were found were removed. The initial conditions were chosen "randomly". Initial guess were made where possible, e.g. the value of C_{L_α} is positive and is most likely somewhere close to 2π. This method is rather time consuming, but it led to a relatively robust parameter optimization.

Chapter 5

Conclusion

In this section the main conclusion of the three chapters: Stall modeling, Flight Path Reconstruction and Parameter Estimation will be given. This will include all major conclusions that can be drawn from this literature study. Any detailed information can be found in the chapters themselves.

5-1 Stall Modeling

Stall model features that are proposed by the ICATEE are:

- Stall Hysteresis,
- Stall buffet,
- Uncommanded roll response or roll-off, requiring significant control deflection to counter,
- Apparent randomness or non-repeatability,
- Changes in pitch stability,
- Degradation in control response (pitch, roll, yaw),
- Degradation in static/dynamic lateral-directional stability,
- Mach effects,

The stall characteristics that will be focused on the most are the stall hysteresis and buffet effect. Next to that an uncommanded roll-off will be modeled, together with an apparent randomness. Regarding the aerodynamics, only the longitudinal values will be estimated. The reason for doing so is that the flight test data does not contain a side slip measurement, which limits the lateral modeling capabilities.

This flight test data is gathered during the third year bachelor flight pratical, at DUT. During these flights the students will experience the dynamics of an aircraft, including effects such as: phugoid, dutch-roll and weightlessness. One part of this practical is to experience a stall as well, of which the data is used for this thesis. In total there were 86 stalls used for the development of the stall model, 82 of these stalls were flown quasi-steady. This means that the pitch rate is approximately zero during the approach to stall. The other four were flown using a pull-up maneuver, in which the aircraft pitched up with a load factor of approximately 1.3 g. Out of the 86 stalls, 80 were flown in a standard cruise configuration, i.e. flaps and gear up. The other six were flown in different configurations: flaps at 15° and landing gear up, flaps at 15° and landing gear down and flaps at 40° and landing gear down. In each of these non-cruise configuration two stalls were performed: One quasi-steady stall and a stall with a pull-up maneuver. An overview of the test maneuvers within the flight envelope are shown in Figure 5-1.

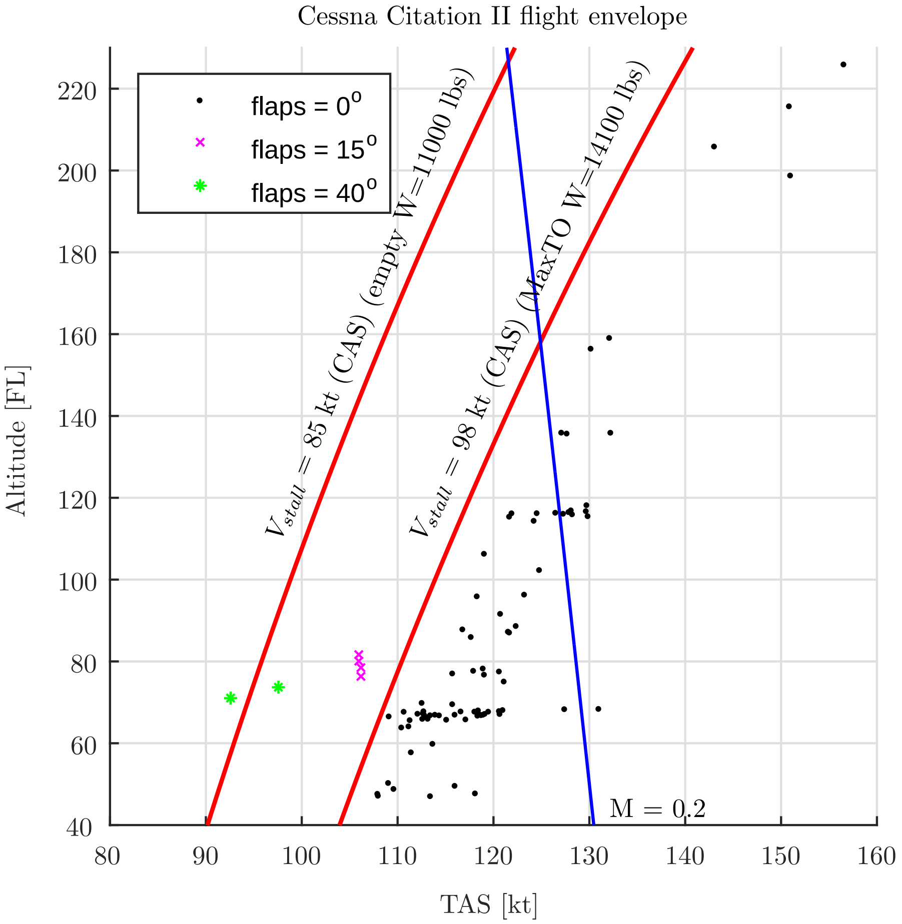

Figure 5-1: An overview of where the data points were captured within the flight envelope

A promising method of modeling the stall hysteresis is based on Kirchoff's flow separation theory (Fischenberg, 1995), which has been applied with success before (Dias, 2015). This however leads to the use of nonlinear parameter estimation techniques. Nonlinear parameter estimation techniques, in contrast to linear parameter estimation techniques tend to find local optimum solutions instead of the global optimum. Furthermore a set of initial parameters need to be provided for nonlinear parameter estimation, preferably close to the global optimum.

Furthermore the differential equation as given in Eq. 2-8 can only be estimated using highly dynamic maneuvers in the flow separated flight regime. If these however are not available then the parameter that influences the transient effect (τ_1) should be removed, reducing the differential equation to just a ordinary equation.

Lastly the lateral dynamics of the stall model will be modeled by calculating the forces generated by both wings separately. The difference in normal and tangential force generate a rolling and yawing moment respectively. The blending of the two models will be done by blending the forces and moments generated by the baseline and stall model.

5-2 Flight Path Reconstruction

For flight path reconstruction both filters and smoothers can be used. Due to the errors in the measurements of the airflow and the biases in the IMU measurements, the filters perform better than the smoothers.

Although the result tend to favor the IEKF, there is not really a large distinction between the performance of the IEKF and the UKF. Both filters predict the state variables reasonably well. The UKF however tends to be more robust than the IEKF, although this has not been proven, during user experience a larger variation in initial condition and initial covariance could be used with the UKF. Next to that the variation of the process and measurement noise covariance matrices were better handled by the UKF as well. This is all however at the cost of a higher run time, which is approximately eight times longer.

5-3 Parameter Estimation

Although the parameter estimation chapter only describes three different algorithms, it is still possible to draw a few conclusions through user experience.

Overall the Nelder-Mead optimization algorithm is the most robust option, most likely due to the fact that no matrix inversions need to be applied. This however also led to sub-optimal parameter estimations. The Nelder-Mead algorithm thus tends to fall into a local optimum.

The Levenberg-Marquardt algorithm on the other hand was able to find the global optimum more often than Nelder-Mead. One problem that occurred often are numerical instabilities due to the inversion of the Jacobian. This inversion was often (close to) singular. This could be solved by running the optimization algorithm multiple times, e.g. a thousand times. Then removing all the solutions in which numerical instabilities occurred. The multiple runs were all started at "random" initial conditions. Of course some initial estimates were made, such as that C_{L_α} is positive. This process is time consuming, but it led to a relatively robust optimization of the parameter estimation.

Recapping on the research question. The main research question: **Which stall characteristics are identifiable using quasi-steady stalls**, cannot be answered yet at the end of this preliminary thesis. The expectation is that the longitudinal aerodynamics can be captured, except for dynamic effects, such as C_{m_q}. To answer this question the real flight data has to be used, whereas now only simulated data from DASMAT was used. Typical stall characteristics however were recommend by the ICATEE. A few important characteristics are: Hysteresis effect, buffet effect, an uncommanded roll-off and apparent randomness. The hysteresis effect can be modeled using an approximation of Kirchoff's flow separation theory. For the buffet effect however a clear answer as yet to be found. A proposal is to look into the frequency domain of signals such as the accelerations and control surface deflections. These accelerations could show a certain dominant frequency and amplitude which can be used for modeling the stall buffet. The parameter estimation will be most likely done using a Levenberg-Marquardt algorithm. The reason for doing so is that the Nelder-Mead algorithm led to local optima more often than Levenberg-Marquardt.

Bibliography

Abramov, N., Goman, M., Khrabrov, A., Kolesnikov, E., Fucke, L., Soemarwoto, B., et al. (2012, aug). Pushing ahead - SUPRA airplane model for upset recovery. In *AIAA modeling and simulation technologies conference.* American Institute of Aeronautics and Astronautics (AIAA). Available from `http://dx.doi.org/10.2514/6.2012-4631`

Anderson, J. (2001). *Fundamentals of aerodynamics.* McGraw-Hill.

Bennis, R. (1998). *Non-linear State Estimation Techniques with Application to Dynamic Modelling of Angle of Attack Vane from Cessna Citation II Flight Data.* Unpublished master's thesis, Delft University of Technology, the Netherlands.

Cessna Aircraft Company. (2009, mar). *Type–Certificate Data Sheet for Cessna 500,550,S550,560 and 560XL (Citations).* European Aviation Safety Agency. Available from `https://easa.europa.eu/system/files/dfu/EASA-TCDS-A.207_(IM)_Cessna_500,_550,_S550,_560_and_560XL-02-05032009.pdf`

Crider, D., & Foster, J. (2012, aug). Simulation modeling requirements for loss-of-control accident prevention of turboprop transport aircraft. In *AIAA modeling and simulation technologies conference.* Hampton (VA), USA: American Institute of Aeronautics and Astronautics (AIAA). Available from `http://dx.doi.org/10.2514/6.2012-4569`

de Visser, C. C. (2011). *Global Nonlinear Model Identification with Multivariate Splines.* Phd thesis, Delft University of Technology, Faculty of Aerospace Engineering, Delft, The Netherlands.

Dias, J. N. (2015, jun). Unsteady and post-stall model identification using dynamic stall maneuvers. In *AIAA atmospheric flight mechanics conference.* Dallas (TX), USA: American Institute of Aeronautics and Astronautics (AIAA). Available from `http://dx.doi.org/10.2514/6.2015-2705`

FAA. (2013). *FAA 14 CFR PART 121: Qualification, Service, and Use of Crewmembers and Aircraft Dispatchers; Final Rule* (Vol. 78) (No. 218).

FAA. (2014). *FAA 14 CFR PART 60: Flight Simulation Training Device Qualification Standards for Extended Envelope and Adverse Weather Event Training Tasks* (Vol. 79) (No. 132).

Fischenberg, D. (1995, aug). Identification of an unsteady aerodynamic stall model from flight test data. In *20th atmospheric flight mechanics conference.* Baltimore (MD), USA: American Institute of Aeronautics and Astronautics (AIAA). Available from `http://dx.doi.org/10.2514/6.1995-3438`

Fischenberg, D., & Jategaonkar, R. (1999, March). Identification of Aircraft Stall behavior from Flight Test Data. In *Proceedings of the rto sci symposium on system identification for integrated aircraft development and flight testing.* Braunschweig, Germany: German Aerospace Center (DLR).

Foster, J. V., Cunningham, K., Fremaux, C. M., Shah, G. H., Stewart, E. C., Rivers, R. A., et al. (2005, aug). Dynamics modeling and simulation of large transport airplanes in upset conditions. In *AIAA guidance, navigation, and control conference and exhibit.* San Francisco (CA), USA: American Institute of Aeronautics and Astronautics (AIAA). Available from `http://dx.doi.org/10.2514/6.2005-5933`

Furlong, G. C., & Fitzpatrick, J. E. (1947, May). *Effects of mach number and reynolds number on the maximum lift coefficient of a wing of naca 230-series airfoil sections* (Technical Note No. 1299). Washington (DC): National Advisory Committee for Aeronautics.

Gadeberg, B. L. (1951, October). *The effect of rate of change of angle of attack on the maximum lift coefficient of a pursuit airplane* (Technical Note No. 2525). Washington (DC), USA: National Advisory Committee for Aeronautics.

Gingras, D. R., Ralston, J. N., Oltman, R., Wilkening, C., Watts, R., & Derochers, P. (2014, jan). Flight simulator augmentation for stall and upset training. In *AIAA modeling and simulation technologies conference.* American Institute of Aeronautics and Astronautics (AIAA). Available from `http://dx.doi.org/10.2514/6.2014-1003`

Gracey, W. (1958, August). *Summary of methods of measuring angle of attack on aircraft* (Technical Note No. 4351). Washington (DC): National Advisory Committee for Aeronautics.

Hartikainen, J., Solin, A., & Särkkä, S. (2011, aug). Optimal filtering with kalman filters and smoothers. *Department of Biomedica Engineering and Computational Sciences, Aalto University School of Science: Greater Helsinki, Finland*.

Hartley, H. O. (1961, may). The modified gauss-newton method for the fitting of non-linear regression functions by least squares. *Technometrics*, *3*(2), 269. Available from `http://dx.doi.org/10.2307/1266117`

Haykin, S. (Ed.). (2001). *Kalman filtering and neural networks.* Hamilton (ON), Canada: Wiley-Blackwell. Available from `http://dx.doi.org/10.1002/0471221546`

Hermann, R., & Krener, A. (1977, oct). Nonlinear controllability and observability. *IEEE Transactions on Automatic Control*, *22*(5), 728–740. Available from `http://dx.doi.org/10.1109/tac.1977.1101601`

Julier, S. (2002, May). The scaled unscented transformation. In *Proceedings of the 2002 american control conference (IEEE)* (Vol. 6, pp. 4555–4559). Jefferson City (MO), USA: Institute of Electrical & Electronics Engineers (IEEE). Available from `http://dx.doi.org/10.1109/acc.2002.1025369`

Julier, S., Uhlmann, J., & Durrant-Whyte, H. (2000, mar). A new method for the nonlinear transformation of means and covariances in filters and estimators. *IEEE Transactions on Automatic Control*, *45*(3), 477–482. Available from `http://dx.doi.org/10.1109/9.847726`

Kay, J., Ralston, J., Lash, S., Kay, J., Ralston, J., & Lash, S. (1997, aug). Development of non-linear, low-speed aerodynamic model for the f-16/VISTA. In *22nd atmospheric flight mechanics conference.* American Institute of Aeronautics and Astronautics (AIAA). Available from `http://dx.doi.org/10.2514/6.1997-3576`

Laban, M. (1994). *On-Line Aircraft Aerodynamic Model Identification.* Phd thesis, Delft University of Technology, Faculty of Aerospace Engineering, Delft, The Netherlands.

Lagarias, J. C., Reeds, J. A., Wright, M. H., & Wright, P. E. (1998, jan). Convergence properties of the nelder–mead simplex method in low dimensions. *SIAM J. Optim.*, *9*(1), 112–147. Available from `http://dx.doi.org/10.1137/s1052623496303470`

Laster, M., Stanewsky, E., Sinclair, D., & Sickles, W. (1998, jun). Reynolds number scaling at transonic speeds. In *20th AIAA advanced measurement and ground testing technology conference.* Albuquerque (NM), USA: American Institute of Aeronautics and Astronautics (AIAA). Available from `http://dx.doi.org/10.2514/6.1998-2878`

Lewis, F., Xie, L., & Popa, D. (2007). *Optimal and robust estimation: With an introduction to stochastic control theory, second edition.* Boca Raton (FL), USA: CRC Press. Available from `https://books.google.nl/books?id=hNXLBQAAQBAJ`

Linden, C. van der. (1996). *DASMAT-Delft University Aircraft Simulation Model and Analysis Tool)* (Vol. 1; Tech. Rep. No. 1). 2600 GB Delft, The Netherlands: Delft University of Technology.

Loftin, L. K. (1985). *Quest for performance: The evolution of modern aircraft* (No. NASA SP-468). Washington (DC): National Aeronautics and Space Administration (NASA).

Malcolm, G. (1985, aug). Rotary-balance experiments on a modern fighter aircraft configuration at high reynolds numbers. In *12th atmospheric flight mechanics conference.* American Institute of Aeronautics and Astronautics (AIAA). Available from `http://dx.doi.org/10.2514/6.1985-1829`

Marquardt, D. W. (1963, jun). An algorithm for least-squares estimation of nonlinear parameters. *Journal of the Society for Industrial and Applied Mathematics*, *11*(2), 431–441. Available from `http://dx.doi.org/10.1137/0111030`

Morelli, E. A., Cunningham, K., & Hill, M. A. (2013, aug). Global aerodynamic modeling for stall/upset recovery training using efficient piloted flight test techniques. In *AIAA modeling and simulation technologies (MST) conference.* American Institute of Aeronautics and Astronautics (AIAA). Available from `http://dx.doi.org/10.2514/6.2013-4976`

Mulder, J., Chu, Q., Sridhar, J., Breeman, J., & Laban, M. (1999, oct). Non-linear aircraft flight path reconstruction review and new advances. *Progress in Aerospace Sciences*, *35*(7), 673–726. Available from `http://dx.doi.org/10.1016/s0376-0421(99)00005-6`

Mulder, J., Sridhar, J., & Breeman, J. (1994). *Agard flight test techniques series. volume 3. identification of dynamic systems-applications to aircraft. part 2. nonlinear analysis and manoeuvre design.)* (Vol. 3; Tech. Rep. No. 2). 7 Rue Ancelle, 92200 Neuilly-sur-Seine, France: DTIC Document.

Mulder, J., van Staveren, W., van der Vaart, J., de Weerdt, E., de Visser, C., in 't Veld, A., et al. (2013). *Lecture notes ae3202: Flight dynamics.* Delft, The Netherlands: Delft University of Technology.

Murch, A., & Foster, J. (2007, jan). Recent NASA research on aerodynamic modeling of post-stall and spin dynamics of large transport airplanes. In *45th AIAA aerospace sciences meeting and exhibit.* Hampton (VA), USA: American Institute of Aeronautics and Astronautics. Available from `http://dx.doi.org/10.2514/6.2007-463`

Nelder, J. A., & Mead, R. (1965, jan). A simplex method for function minimization. *The Computer Journal*, *7*(4), 308–313. Available from `http://dx.doi.org/10.1093/comjnl/7.4.308`

Nguyen, L. T., Ogburn, M. E., Gilbert, W. P., Kibler, K. S., Brown, P. W., & Deal, P. L. (1979, December). *Simulator study of stall/post-stall characteristics of a fighter airplane with relaxed longitudinal static stability* (Technical Paper No. 1538). Washington: National Aeronautics and Space Administration.

Nie, Y., van Kampen, E.-J., Chu, Q. P., Kier, T., & Looye, G. H. N. (2015, jan). Geometry Based Quick Aircraft Modeling Method for Upset Recovery Applications. In *Proceedings of the aiaa modeling and simulation technologies conference, kissimmee (fl).* Delft, The Netherlands: American Institute of Aeronautics and Astronautics (AIAA). Available from `http://dx.doi.org/10.2514/6.2015-2034`

NTSB. (2013). *Annual Review 2013 – Data and Statistics.* `http://www.ntsb.gov/investigations/data/Pages/AviationDataStats.aspx`. (Accessed on 03–22–2016)

O'Connor, C., Ralston, J., & Fitzgerald, T. (1996, jul). Evaluation of the NAWC/AD f/a-18 c/d simulation including database coverage and dynamic data implementation techniques. In *21st atmospheric flight mechanics conference.* American Institute of Aeronautics and Astronautics (AIAA). Available from `http://dx.doi.org/10.2514/6.1996-3365`

O'Rourke, M., Ralston, J., Bell, J., Lash, S., O'Rourke, M., Ralston, J., et al. (1997, aug). PC-based simulation of the f-16/MATV. In *Modeling and simulation technologies conference.* American Institute of Aeronautics and Astronautics (AIAA). Available from `http://dx.doi.org/10.2514/6.1997-3728`

Ostowari, C., & Naik, D. (1985, jan). *Post-stall wind tunnel data for NACA 44xx series airfoil sections* (Tech. Rep.). Available from `http://dx.doi.org/10.2172/5791328`

Ralston, J., Gingras, D., Wilkening, C., & Descrochers, P. (2012, aug). The application of potential data sources for simulator compliance with ICATEE recommended stall modeling requirements. In *AIAA modeling and simulation technologies conference.* Minneapolis (MN), USA: American Institute of Aeronautics and Astronautics (AIAA). Available from `http://dx.doi.org/10.2514/6.2012-4568`

Rauch, H. E., Striebel, C. T., & Tung, F. (1965, aug). Maximum likelihood estimates of linear dynamic systems. *AIAA Journal*, *3*(8), 1445–1450. Available from `http://dx.doi.org/10.2514/3.3166`

Särkkä, S. (2008, apr). Unscented rauch–tung–striebel smoother. *IEEE Transactions on Automatic Control*, *53*(3), 845–849. Available from `http://dx.doi.org/10.1109/tac.2008.919531`

Schroeder, J. A., Bürki-Cohen, J., Shikany, D. A., Gingras, D. R., & Desrochers, P. (2014, jan). An Evaluation of Several Stall Models for Commercial Transport Training. In *AIAA modeling and simulation technologies conference.* National Harbor (MD), USA: American Institute of Aeronautics and Astronautics (AIAA). Available from `http://dx.doi.org/10.2514/6.2014-1002`

Singh, J., & Jategaonkar, R. V. (1996, may). Identification of lateral-directional behavior in stall from flight data. *Journal of Aircraft*, *33*(3), 627–630. Available from `http://dx.doi.org/10.2514/3.46993`

Song, Y., & Grizzle, J. W. (1992, June). The extended kalman filter as a local asymptotic observer for nonlinear discrete-time systems. In *American control conference, 1992* (pp. 3365–3369). Ann Arbor (MI), USA: IEEE Journal of Mathematical Systems, Estimation and Control.

Teixeira, B. O., Tôrres, L. A., Iscold, P., & Aguirre, L. A. (2011, jan). Flight path reconstruction – a comparison of nonlinear kalman filter and smoother algorithms. *Aerospace*

Science and Technology, *15*(1), 60–71. Available from `http://dx.doi.org/10.1016/j.ast.2010.07.005`

Teng, T., Zhang, T., Liu, S., & Grant, P. (2015, jan). Representative post-stall modeling of t-tail regional jet and turboprop aircraft for flight training simulator. In *AIAA modeling and simulation technologies conference.* Kissimmee (FL), USA: American Institute of Aeronautics and Astronautics (AIAA). Available from `http://dx.doi.org/10.2514/6.2015-2032`

Walcott, B. L., Corless, M. J., & Zak, S. H. (1987, jun). Comparative study of non-linear state-observation techniques. *Int. J. of Control*, *45*(6), 2109–2132. Available from `http://dx.doi.org/10.1080/00207178708933870`

Wan, E., & van der Merwe, R. (2000, October). The unscented kalman filter for nonlinear estimation. In *Proceedings of the IEEE 2000 adaptive systems for signal processing, communications, and control symposium* (pp. 153–158). Beaverton (OR), USA: Institute of Electrical & Electronics Engineers (IEEE). Available from `http://dx.doi.org/10.1109/asspcc.2000.882463`

Weiss, S., Friehmelt, H., Plaetschke, E., & Rohlf, D. (1996, may). X-31a system identification using single-surface excitation at high angles of attack. *Journal of Aircraft*, *33*(3), 485–490. Available from `http://dx.doi.org/10.2514/3.46970`

Part III

Appendices

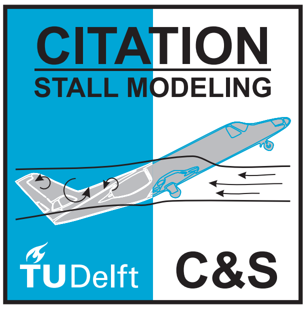

Measurement noise levels

Table 1: Standard Deviations of real life measurements (1)

Measurement	bias	std	unit	Source
x	-	0.20801	m	FTIScal-20151007_074445.hdf5
y	-	0.27464	m	FTIScal-20151007_074445.hdf5
h	-	0.22853	m	FTISxprt-20150318_083858.hdf5
hdot	-	0.10836	m/s	FTISxprt-20150318_083858.hdf5
phi	-	0.00162	rad	FTIScal-20150318_083858.hdf5
theta	-	0.00034	rad	FTIScal-20150318_083858.hdf5
psi	-	0.00113	rad	FTIScal-20150318_083858.hdf5
Vtas	-	0.08967	m/s	FTIScal-20150318_083858.hdf5
alpha(vane)	-	0.00021	rad	FTIScal-20150318_083858.hdf6
alpha(b)	-	0.00060	rad	FPRCV-20151030_092727.mat
beta(b)	-	0.00054	rad	FPRCV-20151030_092727.mat
p	-0.00004	0.00094	rad/s	FTISxprt-20150318_083858.hdf5
q	-0.00002	0.00031	rad/s	FTISxprt-20150318_083858.hdf5
r	-0.00003	0.00059	rad/s	FTISxprt-20150318_083858.hdf5
Ax	0.12550	0.01585	m/s^2	FTIScal-20151007_074445.hdf5/ FTISxprt-20150318_083858.hdf5
Ay	0.16430	0.04742	m/s^2	FTIScal-20151007_074445.hdf5
Az	0.03553	0.08483	m/s^2	FTISxprt-20150318_083858.hdf5
de	-	0.00139	rad	FTIScal-20151007_074445.hdf5
da	-	0.00055	rad	FTIScal-20151007_074445.hdf5
dr	-	0.00039	rad	FTISxprt-20150318_083858.hdf5

Table 2: Standard Deviations of real life measurements (2)

Measurement	**Time Range [s]**	**Engine State**	**Instrument**	**Original Unit**
x	50 to 150	off	arinc/gps	deg
y	50 to 150	off	arinc/gps	deg
h	10 to 35	idle	arinc/Dadc1/alt	ft
hdot	10 to 35	idle	arinc/Dadc1/altRate	ft/min
phi	1180 to 1270	on	arinc/Ahrs1/Roll	deg
theta	1315 to 1355	on	arinc/Ahrs1/Pitch	deg
psi	2440 to 2540	on	arinc/Fms1/trueHdg	deg
Vtas	910 to 990	on	arinc/Dadc1/tas	kts
alpha(vane)	910 to 950	on	analog/Vane_AOA	deg
alpha(b)	8.5 to 11.5	on	?	?
beta(b)	8.5 to 11.5	on	?	?
p	10 to 35 / 910 to 950	idle / on	arinc/Ahrs1/bRollRate	deg/s
q	10 to 35	idle	arinc/Ahrs1/bPitchRate	deg/s
r	10 to 35 / 910 to 950	idle / on	arinc/Ahrs1/bYawRate	deg/s
Ax	50 to 150 / 10 to 35	off/ idle	arinc/Ahrs1/bLongAcc	g
Ay	50 to 150 / 910 to 950	off/ on	arinc/Ahrs1/bLatAcc	g
Az	10 to 35	idle	arinc/Ahrs1/bNormAcc	g
de	50 to 150	off	synchro/delta_e	deg
da	50 to 150	off	synchro/delta_a	deg
dr	10 to 35	idle	synchro/delta_r	deg

Angle of Attack Vane Modeling

The angle of attack and angle of side slip are two very important parameters in flight modeling. All aerodynamic forces and moments are in someway a function of these two variables. The AoA and AoSS are also quiet difficult to obtain during flight testing. These measurements are influenced by things such as body induced velocities and unknown wind components. A large part of this can be compensated by measuring the angle of attack far in front of the aircraft, using a so called "boom". If the nose is not to blunt, an AoA measurement at 1.5 times the fuselage diameter or more will essentially measure the true angle of attack (Gracey, 1958).

For this thesis however the AoA boom was unavailable, as well as an measurement for the AoSS. The Cessna Citation II however contains an AoA vane on the right side of the aircraft, in front of the wings. This vane of course is not far in front of the aircraft and thus is heavily induced by body induced velocities.

Another problem is that this vane is physically damped. This damping acts as an filter on the measurements, which results in a rather smooth signal. A comparison between the boom and vane measurement can be made from Figure 2. Three effects can be found from this figure:

1. Body induced velocities are definitely present, since the AoA measured by the vane is approximately 1.1 degrees lower than AoA measured by the boom. Although it must be noted that the boom in this case is the raw signal, and thus not correct for any body induced velocities as well.
2. The AoA as measured by the vane is well damped, resulting in a rather smooth signal. The boom measurements contains a higher frequency signals.
3. The damping of the vane also causes a time delay in its measurement. When comparing the vane with the boom, the vane has a time delay of approximately 0.2 seconds.

Since the AoA is such a crucial variable it would be nice to obtain an as good as possible estimate of the AoA. To do so the dynamics of the AoA vane were modeled in the Kalman filter, as proposed by (Bennis, 1998). This was done using a low-pass filter with a time delay of 0.2 seconds. This first order filter is given by Eq. 1.

$$\frac{\alpha_v(s)}{\alpha_v^*(s)} = \frac{1}{\tau s + 1} \quad \Rightarrow \quad s\alpha_v(s) = \frac{1}{\tau}\left(\alpha_v^*(s) - \alpha_v(s)\right) \tag{1}$$

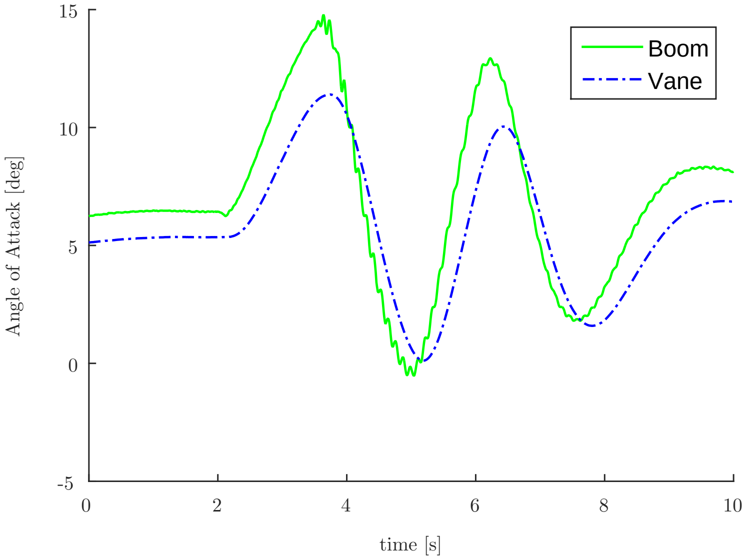

Figure 2: The angle of attack as measured by the boom and by the vane

Where α_v is the measured angle of attack by the vane and α_v^* is the angle of attack in the area of the α-vane which could be expected based on the state:

$$\alpha_v^* = \left(1 + C_{\alpha_{up}}\right) \arctan \frac{w}{u} - \frac{x_{v_\alpha}\left(q - \lambda_q\right)}{\sqrt{u^2 + v^2 + w^2}} + C_{\alpha 0} \tag{2}$$

An extra must then be added to the navigation systems, which is α_v. The kinematic equation for this state is given by Eq. 3

$$\dot{\alpha}_v = \frac{1}{\tau}\left(\alpha_v^* - \alpha_v\right) = \frac{1}{\tau}\left[\left(1 + C_{\alpha_{up}}\right) \arctan \frac{w}{u} - \frac{x_{v_\alpha}\left(q - \lambda_q\right)}{\sqrt{u^2 + v^2 + w^2}} + C_{\alpha 0} - \alpha_v\right] \tag{3}$$

The angle of attack in the observation equations is then just:

$$\alpha_m = \alpha_v \tag{4}$$

When adding the vane dynamics to the Kalman filter, the complexity of the navigation system is increased. One question that comes to mind then is whether or not the system is still observable. This can be done using the method as explained in section 3-5. Lets call n, as in $L_f^{n-1} h\left(x\right)$ the number of recursions that was used. In table 3 the number of recursions that are needed to obtain observability can be found.

Table 3: Number of recursions that are needed to obtain observability.

Parameter used	Number of recursions
$C_{\alpha_{up}} + C_{\alpha 0}$	4
$C_{\alpha_{up}}$	3
$C_{\alpha 0}$	3

As shown when using the full navigation system, i.e. including the vane dynamics, the upwash and unknown wind coefficients, the state is observable after four recursions. This means that in theory the state is fully observable. This however does not necessarily mean that the Kalman filter will converge. In Figure 3 the upwash and unknown wind coefficients for three different initial values are shown. As can be seen both values do not converge to one solution, and is depended on the initial condition.

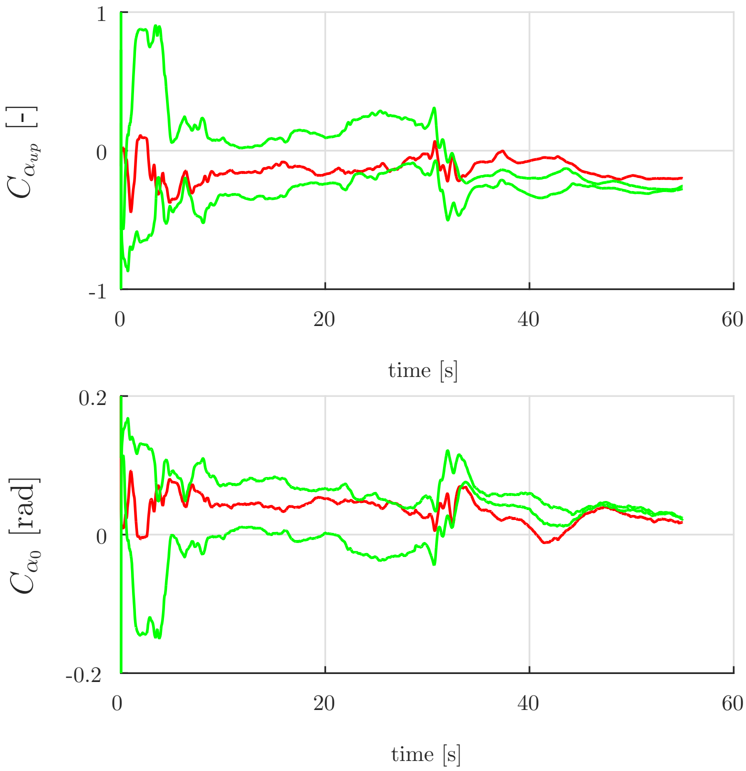

Figure 3: Upwash coefficient $C_{\alpha_{up}}$ and unknown wind component C_{α_0} for three different initial conditions.

To solve this problem either the upwash component or the unknown wind component has to be removed. As shown in table 3 when removing one of these components the number of recursions that are needed is reduced to three. When removing one of the components it was found that the state will converge. An example, for this case $C_{\alpha_{up}}$ is shown in Figure 4. A similar plot can be shown for C_{α_0} as well.

The number of recursions be interpreted more intuitively as follows. When one recursion are needed, i.e. $L_f^0 h(x) = h(x)$ the complete state directly observable from the measurements. When two recursions are needed the state is indirectly observable from the measurements. The Kalman filter will still most likely converge, since only ”one layer” is needed to get to the state. When using three recursions, it is less likely that the Kalman filter will converge, but as shown in Figure 4 it is still possible. When four recursions are needed it is even less likely that the Kalman filter will converge and during this thesis there is no example found of when the Kalman filter converges when needing four recursions. In general the rule is thus that the more recursions are needed, the less likely it is the Kalman filter will converge. This can be compared to humans to each other. If person A, talks directly to person B (i.e. one recursion), the message goes directly from A to B. However when person A talks to B. Then B to C, up until person E (i.e. four recursions). It is less likely that the correct message is transferred from person A to person E.

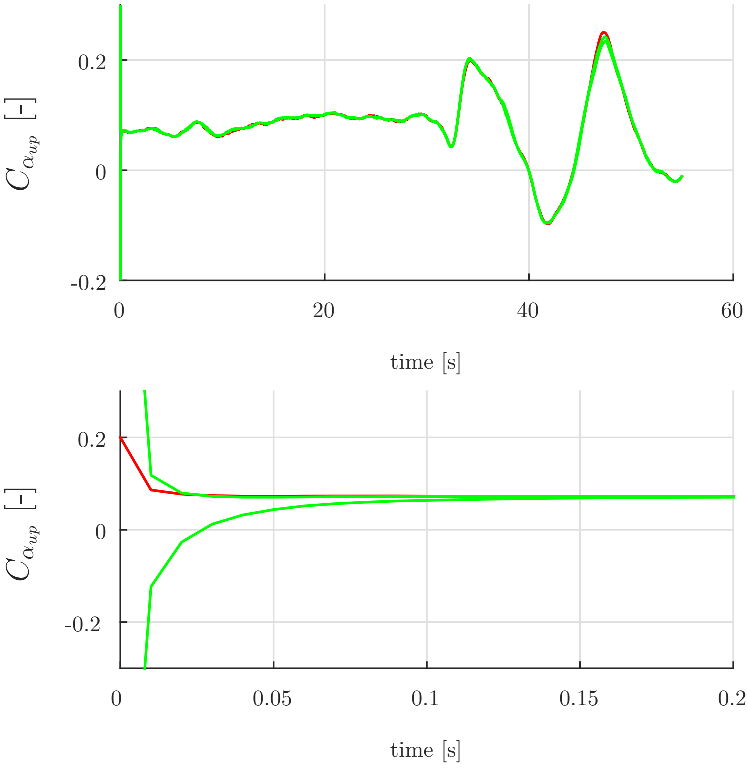

Figure 4: Upwash coefficient $C_{\alpha_{up}}$ for three different initial conditions. Top is full time span, bottom is zoomed view on first 200 ms

Another interesting observation from Figure 4 is that the upwash component during a stall is definitely not constant. The time derivative ($\dot{C}_{\alpha_{up}}$) of this upwash component however is unknown. Setting the time derivative to a value of zero, as in the case of the bias terms is thus not a valid option. To solve this problem the time derivative of the upwash component is modeled as a random walk:

$$\dot{C}_{\alpha_{up}} = 0 + w_{C_\alpha} \tag{5}$$

Where w_{C_α} is a zero mean white noise component. The noise intensity that gave satisfactory results was: $\sigma_{w_{C_\alpha}} = \frac{0.1\pi}{180}$. A too low value does not give the opportunity for the upwash component to change. A too high value results in a very noisy signal.

Final Navigation & Observation models

During the thesis the navigation and observation models that were used have frequently changed. Therefore the models as given in Chapter 3 are not representative anymore. The final navigation and observation equations that were used are given in this Appendix. The time constant τ, that is used in the vane dynamics was set to 0.2 seconds. The value of w_r is a white noise signal with zero mean.

$$\dot{\boldsymbol{x}} = f\left(\boldsymbol{x}\left(t\right), \boldsymbol{u_m}\left(t\right), \boldsymbol{w}\left(t\right)\right)$$

$$\begin{bmatrix} \dot{x} \\ \dot{y} \\ \dot{z} \\ \dot{u} \\ \dot{v} \\ \dot{w} \\ \dot{p} \\ \dot{q} \\ \dot{r} \\ \dot{W}_{x_e} \\ \dot{W}_{y_e} \\ \dot{C}_{\alpha_{up}} \\ \dot{\lambda}_x \\ \dot{\lambda}_y \\ \dot{\lambda}_z \\ \dot{\lambda}_p \\ \dot{\lambda}_q \\ \dot{\lambda}_r \\ \dot{\alpha}_v \end{bmatrix} = \begin{bmatrix} \left[u\cos\theta + \left(v\sin\phi + w\cos\phi\right)\sin\theta\right]\cos\psi - \left(v\cos\phi - w\sin\phi\right)\sin\psi + W_{x_E} \\ \left[u\cos\theta + \left(v\sin\phi + w\cos\phi\right)\sin\theta\right]\sin\psi + \left(v\cos\phi - w\sin\phi\right)\cos\psi + W_{y_E} \\ -u\sin\theta + \left(v\sin\phi + w\cos\phi\right)\cos\theta \\ \left(A_x - \lambda_x\right) - g\sin\theta - \left(q - \lambda_q\right)w + \left(r - \lambda_r\right)v \\ \left(A_y - \lambda_y\right) + g\cos\theta\sin\phi - \left(r - \lambda_r\right)u + \left(p - \lambda_p\right)w \\ \left(A_z - \lambda_z\right) + g\cos\theta\cos\phi - \left(p - \lambda_p\right)v + \left(q - \lambda_q\right)u \\ \left(p - \lambda_p\right) + \left(q - \lambda_q\right)\sin\phi\tan\theta + \left(r - \lambda_r\right)\cos\phi\tan\theta \\ \left(q - \lambda_q\right)\cos\phi - \left(r - \lambda_r\right)\sin\phi \\ \left(q - \lambda_q\right)\frac{\sin\phi}{\cos\theta} + \left(r - \lambda_r\right)\frac{\cos\phi}{\cos\theta} \\ 0.01w_r \\ 0.01w_r \\ \frac{0.1\pi}{180}w_r \\ 0 \\ 0 \\ 0 \\ 0 \\ 0 \\ 0 \\ \frac{1}{\tau}\left(\left(1 + C_{\alpha_{up}}\right)\arctan\frac{w}{u} - \frac{x_{v_\alpha}\left(q - \lambda_q\right)}{\sqrt{u^2+v^2+w^2}} - \alpha_v\right) \end{bmatrix} \tag{6}$$

$$
\begin{aligned}
\boldsymbol{y} &= h\left(\boldsymbol{x}\left(t\right), \boldsymbol{u_m}\left(t\right), \boldsymbol{v}\left(t\right)\right) \\
\begin{bmatrix} x_{gps} \\ y_{gps} \\ h_{DADC} \\ \dot{h}_{DADC} \\ \phi_{AHRS} \\ \theta_{AHRS} \\ \psi_{AHRS} \\ V_{TAS} \\ \alpha_{vane} \\ \beta_{pseudo} \end{bmatrix} &= \begin{bmatrix} x \\ y \\ -z \\ u\sin\theta - \left(v\sin\phi + w\cos\phi\right)\cos\theta \\ \phi \\ \theta \\ \psi \\ \sqrt{u^2+v^2+w^2} \\ \alpha_v \\ \arctan\left(\frac{v}{\sqrt{u^2+w^2}}\right) \end{bmatrix}
\end{aligned} \tag{7}
$$

As can be seen the AoSS is measured by a ”pseudo” signal. This pseudo beta is a zero mean white noise signal with an intensity of 0.1 degrees. It was shown in (Bennis, 1998), that it is better to include a ”pseudo” beta instead of no beta measurement at all. It must be noted however that this assumption is only valid for longitudinal maneuvers!

Important Notes regarding measurements

There are two important notes to be made regarding the measurements of the Cessna Citation II. One about the accelerations and one about the altitude.

-1 Acceleration Measurement

It must be noted that the measured acceleration in y- and z-directions are compensated for the gravity. That means that if the aircraft is at rest, or equilibrium the measured acceleration in y- and z-directions are zero. This does not hold for the acceleration measured in the x-direction, which still measures the specific force. This should be taken into account when filtering and/ or using the data. An example of these acceleration measurements:

-2 Altitude Measurement

When using GPS data for the altitude and altitude rate the filtered results became better than using the DADC data. An example of a stall with pull-up maneuver is given in Figure 6. As it can be seen when using GPS data the overall trends between the raw and reconstructed data seemed to be okay, the difference being an offset, which is to be expected as upwash angle. When using the DADC however the upwash angle is far from constant. This gave problems with estimating the parameters. So it seems as if using GPS data gives better results, than using the DADC which intuitively does not make sense. In Figure 7 I gave the differences between the DADC and GPS measurements of both the altitude and altitude rate.

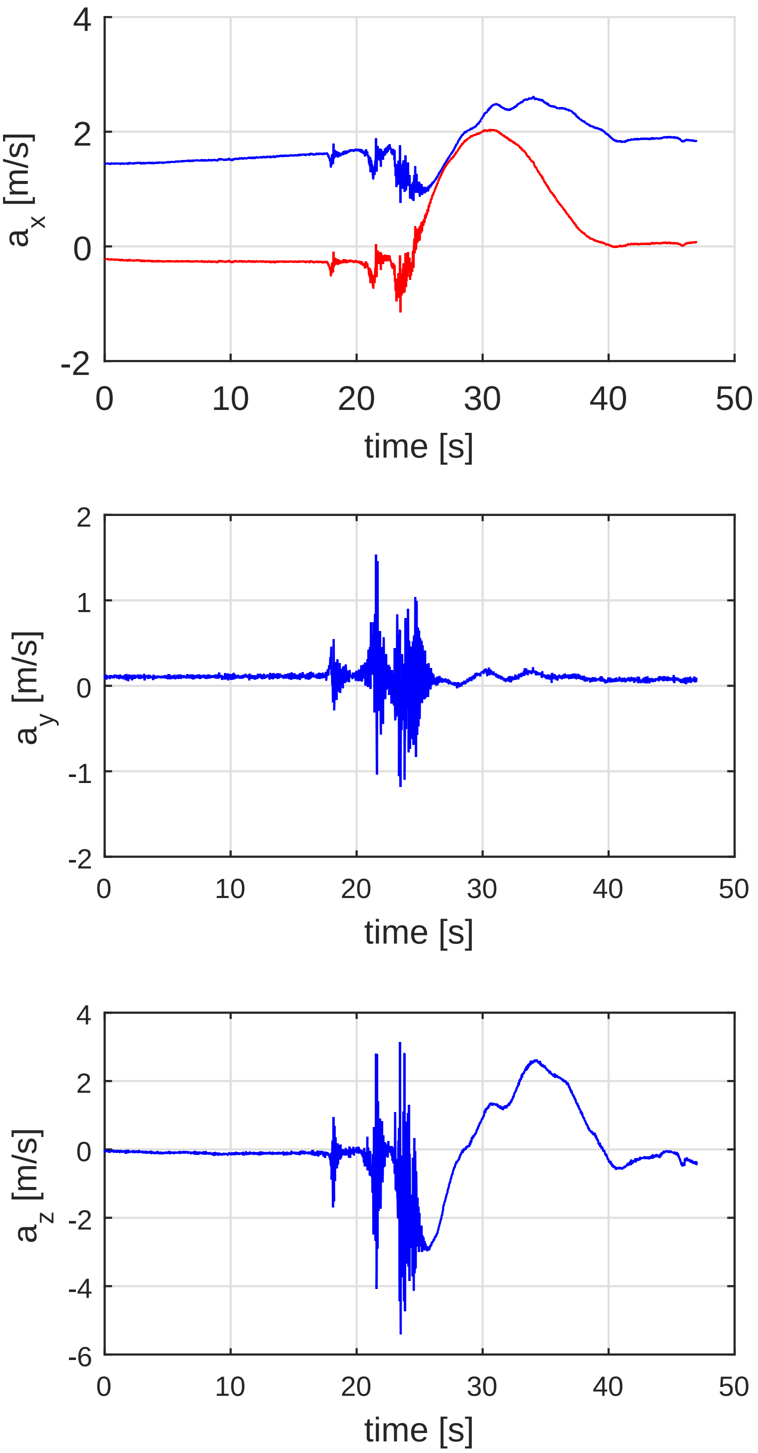

Figure 5: Raw data for the acceleration measurements. Blue line is the measured data, red is (in a_x) is for the gravity corrected value.

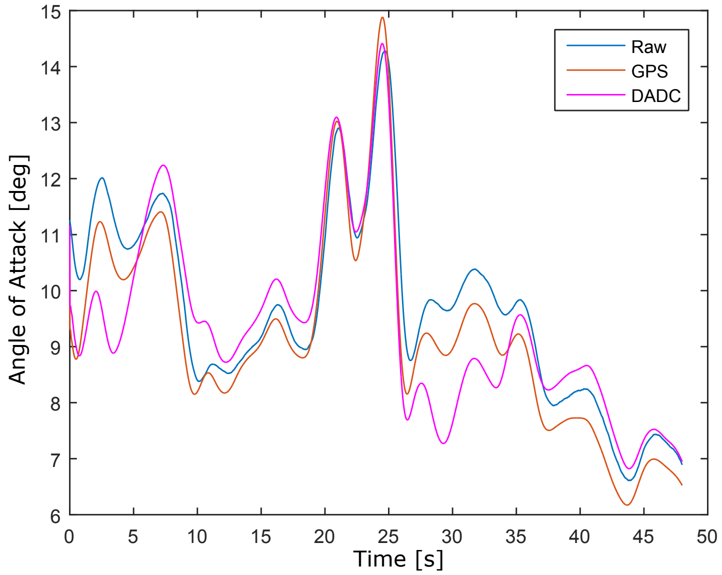

Figure 6: Difference in filtered angle of attack when using DADC and GPS data

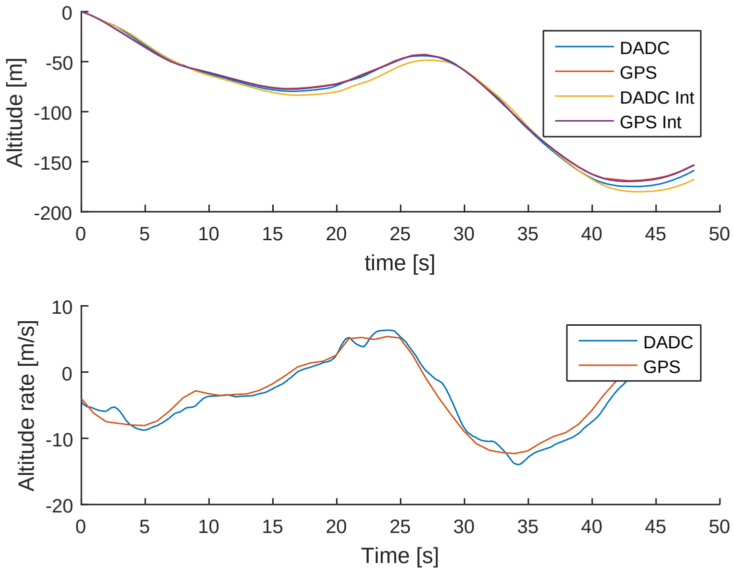

Figure 7: Difference between the GPS and the DADC. Int = integrated velocity